Die approbierte Originalversion dieser Diplom-/Masterarbeit ist in der Hauptbibliothek der Technischen Universität Wien aufgestellt und zugänglich.
http://www.ub.tuwien.ac.at

The approved original version of this diploma or master thesis is available at the main library of the Vienna University of Technology.
http://www.ub.tuwien.ac.at/eng

TECHNISCHE UNIVERSITÄT WIEN

DIPLOMARBEIT

Development of a Modular Cylindrical Magnetron System and Design of a DC Magnetron Sputtering Device for Coating Inner Surfaces of Narrow Tubes

zur Erlangung des akademischen Grades

Diplom-Ingenieurin

im Rahmen des Studiums

Technische Physik

eingereicht von

Miriam Giparakis
Matrikelnummer 01227015

ausgeführt am Institut für Festkörperphysik
der Fakultät für Physik der Technischen Universität Wien

Betreuer: Ao. Univ. Prof. Dipl.-Ing. Dr. Christoph Eisenmenger-Sittner

Wien, 04.12.2018

(Unterschrift Verfasserin)

(Unterschrift Betreuer)

Abstract

Magnetron sputter deposition is a widely used tool for the deposition of high-quality functional thin films on industrially relevant objects. A magnetic configuration modifies the plasma-formation in a favorable way for the desired application. Often this happens by the concentration of the plasma-discharge at specific target-areas. This leads to higher efficiency compared to conventional sputtering using the same parameters. For some applications, magnetrons are the key to enable the applicability of this Physical Vapor Deposition (PVD) process.

The first part of this thesis consisted of the modification of an existing cylindrical magnetron. This happened in two steps: First the magnetron was segmented into modular units. With this modularity in size, a flexibility in target and substrate size arose. In addition, these individual segments were made twistable relative to each other. The effects on the performance of the magnetron with those changes were investigated. In a second step, the same existing cylindrical magnetron was modified again, this time to be suitable for supporting the coating process of inner surfaces of narrow tubes.

This led to the main part of this thesis, namely the construction of a DC-magnetron sputtering device for coating inner surfaces of narrow tubes. In the following, the performance of this setup was tested with different target materials on conducting but also on insulating substrate-tubes. For the latter, a special supporting anode was designed. On both substrate types non-magnetic and even magnetic materials could be deposited in tubes with diameters as low as 8 mm for insulating tubes.

Kurzfassung

Magnetronsputtern ist eine weit verbreitete Beschichtungstechnik um hochqualitative funktionale dünne Schichten auf industriell relevanten Gegenständen zu erzeugen. Eine Magnetkonfiguration verändert die Plasmaausbildung für die gewünschte Anwendung auf günstige Weise. Dies passiert oft indem die Plasmaentladung auf bestimmte Targetflächen konzentriert wird. Bei Verwendung gleicher Parameter führt Magnetronsputtern zu größerer Effizienz im Vergleich zu herkömmlichem Sputtern. Für manche Anwendungen ermöglichen Magnetrons sogar erst die Anwendung dieses physikalischen Gasphasenabscheidungsprozesses (PVD).

Der erste Teil dieser Arbeit beschäftigte sich damit, ein schon existierendes zylindrisches Magnetron zu modifizieren. Dies geschah in zwei Schritten: Als erstes wurde das Magnetron in modulare Elemente segmentiert. Folge dieser Modularität in der Länge ist eine Flexibilität in der Größe des Targets und des Substrates. Zusätzlich wurden die individuellen Segmente gegeneinander verdrehbar konstruiert. Anschließend wurden die Effekte dieser Änderungen auf die Performance des Magnetrons untersucht. In einem zweiten Schritt wurde das gleiche schon existierende zylindrische Magnetron nochmals modifiziert, diesmal um für Innenbeschichtungen von Rohren mit geringem Durchmesser geeignet zu sein.

Dies führte zum Hauptteil dieser Arbeit, nämlich der Konstruktion einer DC-Magnetronsputter-Anlage für die Innenbeschichtung von Rohren mit geringem Durchmesser. Im Folgenden wurde die Performance dieses Aufbaues mit unterschiedlichen Target Materialien für leitende und isolierende Substratrohre getestet. Für letztere wurde eine spezielle Anode konstruiert. Beide Substratrohr-Typen mit einem minimalen Durchmesser von 8 mm für isolierende Rohre, konnten mit nicht-magnetischen und sogar mit magnetischen Materialien beschichtet werden.

Contents

1. Introduction and Motivation

A common desire in material technology are materials equipped with special properties. Often it is sufficient or even crucial that a functionality is present at the surface of a material, for example when the material needs to withstand harsh conditions due to its environment (high temperatures, corrosive environments, chemically reactive substances etc.) or has to have certain other surface-specific properties. Consequently, coatings protecting the bulk material or providing specific functionalities are needed. High-quality thin films can be achieved by PVD (Physical Vapor Deposition) methods, such as magnetron sputtering, which allows deposition processes at relatively low pressures compared to conventional diode sputtering. This is because of the more efficient ionization of the working gas (usually argon (Ar)) and a concentrated plasma discharge at areas prescribed by the magnetic and electric field configuration. Magnetron sputtering is furthermore very adaptable to a variety of different geometries.

In this work, an already existing cylindric magnetron with a specific magnetic configuration was used as a starting point to construct two magnetron-assemblies for different purposes. The performance of both magnetrons was studied, see chapter 4 and chapter 5. In particular, the developed magnetic field was measured using a Hall-probe and simulated using the finite element method, see section 3.3. In addition, Current-Voltage (I-V) characteristics were recorded. One ambition for the existing magnetron was to be modular in height, yielding a flexibility in the size of the whole system. Therefore, the magnetron was segmented, additionally, the single elements were made to be twistable relative to each other. This transformation altered the formed plasma and its effects were studied. In a second step, the magnetic configuration was used to construct a magnetron for deposition of metals on the inside of narrow tubes.

This led to the main part of this work, the construction of a device for inner surfaces of narrow tubes by direct current-(DC)-magnetron sputtering. The deposition of material inside narrow tubes by the sputter-process alone is difficult due to the close proximity of cathode (target) and anode and therefore high necessary working gas pressures. Furthermore, it is not easy to achieve homogeneous films within narrow long tubes. By using a suitable magnetron, the plasma formation can be controlled to take place only in desired areas located within the magnet-assembly. This way a uniform and homogeneous film can be achieved by tuning the motion-pattern of the magnetron.

The designed device was tested for the deposition of copper (Cu), iron (Fe) and aluminum (Al) on the inside of conducting stainless steel tubes and also in insulating acrylic glass tubes, for which a special anode was designed. The deposited thin films were analyzed regarding their film thickness distribution using optical transmission. Also, I-V characteristics were recorded for each target-material/substrate-tube configuration to test its performance, see chapter 6.

2. Physical Basics

In this chapter the physical basics of this work are presented. These include the definition of vacuum as well as a brief overview of the pumping systems and the vacuum gauges for pressure measurement. Subsequently, deposition methods for thin films are discussed with particular attention to sputtering and its extension, magnetron sputtering. The essential physical basics of plasma discharges with special emphasis on magnetron plasmas are discussed.

2.1. Vacuum

In this section vacuum is explained and defined. The pumps, which produce and maintain vacuum, as well as the gauges, which measure the pressure, are introduced.

2.1.1. Characterization of Vacuum

Vacuum is understood as a volume, which is almost free from particles. As a volume can never be completely empty, different vacuum regimes are distinguished [1, 2]:

rough vacuum (10^5 Pa ... 10^2 Pa)

fine vacuum (10^2 Pa ... 10^{-1} Pa)

high vacuum (10^{-1} Pa ... 10^{-5} Pa)

ultrahigh vacuum ($< 10^{-5}$ Pa)

For PVD methods such as sputtering (see section 2.3), which was applied in this thesis, at least high vacuum is demanded as a base pressure. This is due to the following reasons:

- Contaminations from the residual gas on the deposited film are highly undesirable as they can cause defects in the produced layer. A quantity describing how fast these contaminations on surfaces occur depending on the present pressure is the areal impingement rate, see below.

- The mean free path (see below) has to be long enough, so that most of the particles reach the desired area without being deflected. These particles can be ions knocking out deposition material from the cathode or the emitted particles reaching the substrate.

Areal Impingement Rate: The number of impinging particles N per unit time dt on the unit area dA is given by [1]:

$$\frac{dN}{dt} = \frac{n\bar{v}}{4} dA \tag{2.1}$$

where $\bar{v}$ is the mean thermal velocity of the particles and n the particle density.

With a pressure in the range of 10^{-4} Pa, $\bar{v} = 500\,m/s$ and a particle sticking probability of 1 on the chamber walls, they would be covered by a monolayer of residual gas atoms within 3 s [1].

Mean Free Path in Vacuum: The mean free path λ for particles in vacuum can be formulated as [1]:

$$\lambda = \frac{1}{n\sigma} \tag{2.2}$$

where σ is the cross section.

2.1.2. Pumps

Special pumps are needed to generate and maintain vacuum.

In the following, only the pumps used in this thesis are briefly described [1]:

Rotary Vane Pump: A cylindrical valve rotates off axis inside a cylindrical cavity and evacuates the chamber by sucking out gas particles. An oil film between the valve and the pump unit as well as flexible sliders are necessary for the sealing, however the vapor pressure of the oil is a restriction for the achievable vacuum.

Rotary vane pumps reach a pressure in the order from 10 Pa to 10^{-1} Pa and are therefore used to produce prevacuum.

Turbomolecular Pump: This pump requires a prevacuum to function. The main component is a rotor which has a circulation speed in the order of the thermal velocity of the gas particles. When colliding with the rotor most residual gas particles receive a momentum in the direction of the prevacuum pump.

Turbomolecular pumps reach pressures in the upper ultrahigh vacuum regime (around 10^{-5} Pa).

2.1.3. Vacuum Gauges

To measure the total pressure, different gauges, suitable for different pressure regimes exist [2]:

Pirani Gauge: A Pirani gauge consists of a wire, mounted concentrically inside a hollow cylinder.

A wire is heated and kept at a constant temperature by passing a variable current, while heat of the wire is transported by residual gas particles to the cylinder walls, which are at room temperature. This variable current is used as quantity of pressure measurement.

Pirani gauges can be used in a pressure range of 10^5 Pa to 10^{-1} Pa.

Penning Gauge: A Penning gauge belongs to the cold cathode gauges, with a pressure range of 10^{-1} Pa to 10^{-6} Pa.

In between an anode and a cathode, a gas discharge is ignited by applying a high voltage. Through magnets, electrons are forced on certain curves. This increases their lifespan and a single electron can ionize more residual atoms. This way, the discharge can burn on even at very low pressures.

The ions, which impinge on the cathode are measured as an electrical current and from this the pressure can be determined.

Baratron Gauge: As explained in [3], a Baratron gauge measures capacity changes between a diaphragm and a fixed electrode. The diaphragm separates the vacuum, that is to be measured from a very low reference pressure, which can be considered as zero. This reference vacuum is maintained by a getter pump. Depending on the pressure in the chamber, changes in the measured capacity occur due to a change in the shape of the diaphragm. From this, the residual gas pressure can be determined.

Baratrons are available for different pressure ranges from 10^{-1} Pa to ambient and have a very high accuracy.

2.2. A Brief Review of Deposition Methods

Various methods for the deposition of films on surfaces exist [4]:

These differ in their application area, strongly in their deposition rates and in the properties of the deposited films.

For the realization of high-quality thin films with good film adhesion, as needed in many industries, Chemical Vapor Deposition (CVD) and Physical Vapor Deposition (PVD) are commonly used. For these methods the deposition material is brought on the substrate from the vapor phase in form of atoms, molecules or clusters.

In CVD a chemical reaction in the vapor phase takes place with pressures ranging from 10^3 Pa to 10^5 Pa. This leads to a film deposition on a substrate. CVD processes allow a very uniform deposition of films on even complexly shaped substrates. A disadvantage are the arising high reaction temperatures of about 200 – 2000 °C, which limit the choice of suitable substrate materials. In addition, a chemical reaction for deposition of the desired material needs to exist, to which the substrate material also needs to be inert.

In contrast, PVD is characterized by imposing a low thermal load on the substrate, therefore there exists a high variety of usable substrates. Because PVD is a pure physical process, the usable deposition materials are also almost unlimited.

A disadvantage of PVD is that the deposition is strongly direction dependent and therefore the uniform deposition of complexly shaped substrates is difficult, also, the deposition process needs to take place in a vacuum chamber.

In this work, the PVD technique of sputtering was utilized.

2.3. Sputtering

Sputtering is caused by the bombardment of a sample-surface (called target) with energetic particles, mostly ions. Thus, among other processes (see section 2.3.2), surface- material is ejected. This can be utilized in different ways. On the one hand, to 'clean' the sample-surface from contaminations. On the other hand, sputtering can also be used as deposition method, this is then called 'sputter deposition'.

In this thesis, sputtering was only used as a deposition method. Describing the sputter process in detail would exceed the framework of this thesis, therefore only an overview is given here. For more information, see [4–6].

2.3.1. Generation of Ions

The required ions for the sputter process can be generated in different ways, either by using an ion source or by using a gas discharge.

In the present thesis, the source of ions was an Ar plasma discharge, therefore only this method will be discussed in section 2.4.

2.3.2. Atomic Processes during Sputtering

When an ion with sufficient energy collides with the target, amongst other processes, a target-atom can be emitted [4]:

For releasing an atom from the target-surface an energy of at least the threshold energy must be provided. The atoms leave the surface with energies in the range from 10 eV to 40 eV.

The emission process of atoms from the target works as follows: The impinging ion triggers a collision cascade. For emitting atoms or atom-clusters from the target a reversal of the transferred momentum needs to take place, this happens through a collision cascade. The triggered collision cascade penetrates relatively deep into the target and the momentum is transferred to many atoms.

The emitted target atoms are most likely neutral and are ejected from a depth of about 1 nm.

Additionally, further processes, like implantation of the impinging ions, electron emission through argon ions and charge reversal processes can take place.

Furthermore, it is possible for ions to ionize neutral working gas particles on their way to the target. This is an additional source of ionized particles.

2.3.3. Sputter Yield

The sputter yield Y is defined as [4]:

$$Y = \frac{\langle \text{number of ejected particles} \rangle}{\text{number of incoming ions}} \tag{2.3}$$

Y depends on various parameters, like: target-material, impinging ions, ion energy and their angle of impingement. In addition, Y also depends on the combination of chosen target-material and ion-species. For most metals Y is in the range of 1-10.

A sputter yield for Ar ions on a Cu target for an Ar ion energy of 800 eV of $Y = 2,509$ and an energy threshold of 15,8 eV can be calculated online [7] with the equation of Yamamura et al. [8]. This is a half empirical equation, which is valid for mono-atomic targets at normal incidence of the ions [5].

2.4. Plasma

A physical plasma is defined as a quasi-neutral gaseous many-particle system. Electrons, ions and neutral gas particles can move freely. Therefore, a plasma is electroconductive, which makes it influenceable by electric and magnetic fields [9].

Quasi neutrality means that on average the number of positive and negative charge carriers per unit volume is equal. This property makes a plasma electrically neutral on large-scale appearances. No space charges occur in the plasma regions [9].

In this thesis, a glow discharge plasma produced by a DC-source was utilized as an ion-source for the sputter deposition process.

Characteristic Plasma Parameters [10]: The characteristic length in which the plasma differs from quasi neutrality is called the Debye length. It is defined as:

$$\lambda_D = \sqrt{\frac{k_B T_e \varepsilon_0}{n_e e^2}} \tag{2.4}$$

where k_B is the Boltzmann-constant, T_e the electron temperature, ε_0 the dielectric constant of the vacuum, n_e the electron density and e the elementary charge.

For quasi neutrality to be given, the plasma dimensions have to be considerably larger than the Debye length.

Another characteristic parameter is the eigenfrequency of the plasma. It is defined as:

$$\omega_p = \sqrt{\frac{n_e e^2}{m_e \varepsilon_0}} \tag{2.5}$$

with m_e being the electron mass.

The oscillation equation can be written as:

$$m_e \frac{d^2x}{dt^2} + \omega_p x = 0 \tag{2.6}$$

This eigen-oscillation has its origin from the desire of the plasma to preserve quasi neutrality. Electrical fields arise when quasi neutrality is broken. This leads to oscillations of the much lighter electrons around the ions.

2.4.1. Current-Voltage-Characteristics

When free electrons in a diluted gas experience enough acceleration by an applied voltage between cathode and anode to perform ionizations through impact on the working gas atoms, charge carriers are produced and a current flows [11]:

Fig. 2.1 shows that the applied voltage V and the flowing current I of the discharge are codependent.

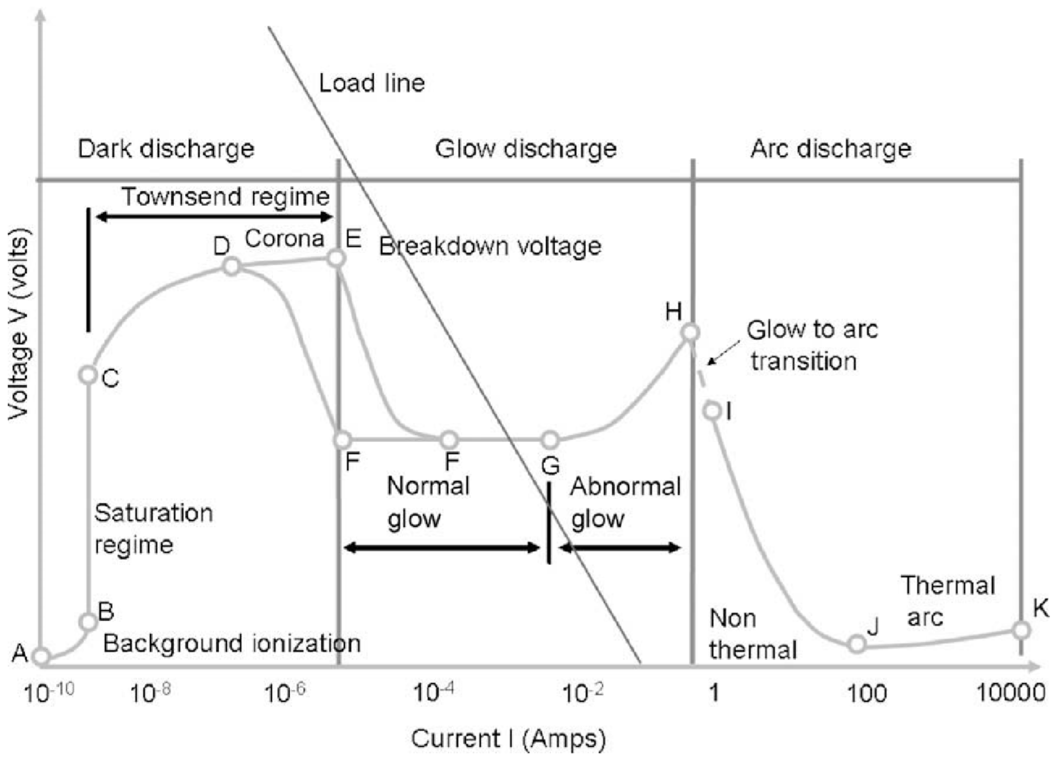

Figure 2.1.: Current-Voltage-Characteristics of a gas discharge. Taken from [5].

Initially electron recombination dominates, then in the saturation regime (between B and C) all electrons reach the anode. Then a charge carrier can provide for its substitute in the region of the self-sustaining discharge in the Townsend regime (between C and E), further on the discharge burns steady. In the glow discharge region (between E and H) the electrons have in some spatial regions enough energy to excite working gas atoms.

In this work, the produced plasma was in the region of the abnormal glow discharge [9]:

The abnormal glow region occurs after a distinct current increase in the characteristics as the plasma covers more and more of the cathode until the entire dimension of the cathode is covered. For this region to be stable, the load line, which is defined as

$$\epsilon = V + I\Omega \tag{2.7}$$

where ϵ is the open-circuit voltage of the DC-source and Ω the ohmic load, must cut the I-V characteristics in this region. When the load line cuts the characteristics at two points, the point at lower voltage is stable.

2.4.2. DC-glow discharge

A DC-glow discharge is generated with the help of a DC-source and is self-sustained. In the simplest version, two electrodes are located opposite of each other in a vacuum chamber. The chamber gets flooded with a diluted working gas. When a voltage between the two electrodes is applied, the working gas gets ionized and a glow discharge develops between the two electrodes [4].

As seen in Fig. 2.2, the glow discharge has a spatial distribution [9]:

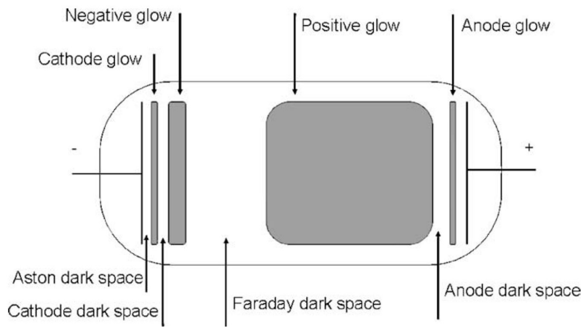

Figure 2.2.: Spatial distribution of a glow discharge. Taken from [5].

In the glowing (grey) regions the energy of the electrons is in a range, in which they can perform excitations. In the cathode dark space, also called the cathode fall, the electrons gain sufficient energy for ionization, this is the region where most atoms get ionized.

The spatial distribution of the light phenomena is dependent on the pressure and the distance between the anode and cathode. The positive column is only visible for high pressures (above 1 Pa).

By reducing the distance between anode and cathode, sequentially, the positive column, the Faraday dark space and finally the negative glow, get shorter. When the distance between the anode and cathode is too small for the negative glow to form, the discharge can no longer be ignited.

2.4.3. Sheaths

If a plasma is in contact with an interface, a form of interaction will arise [9,12], thus a particle current towards the interface is established. This way a sheath will form, in which the plasma is not quasi-neutral. The formed sheath depends on the potential difference between plasma and interface.

The sheath is formed as follows, whereby various cases must be distinguished [9,12]:

When a plasma is in contact with an insulated interface, which has the same potential as the plasma, a high electron transport to the interface will take place. This is because of the much higher mobility of the electrons compared to the ions. Due to this, the interface will charge negatively to the so-called floating potential. A potential hill for electrons and a potential fall for ions will form resulting in a positive space charge in front of the interface, see Fig. 2.3a.

This suggests, that when a plasma is in contact with a grounded interface, the plasma will charge positively compared to this interface, because this time, the interface wont charge negatively with electron impingement. So, the electron transport to the interface does not stop.

Finally sheaths also form in front of cathodes and anodes, see Fig. 2.3b. In front of the cathode a positive space charge forms because of its potential drop compared to the plasma potential. In front of the anode a negative space charge forms.

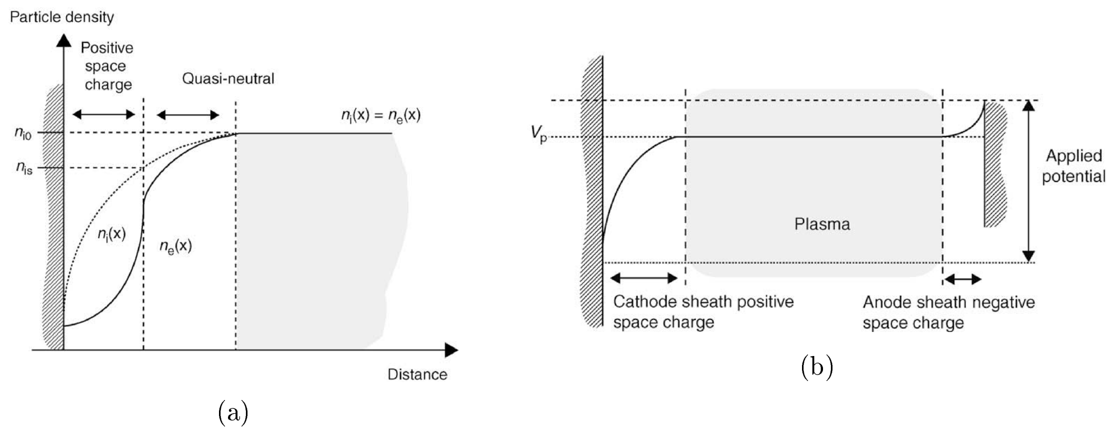

Figure 2.3.: (*a*) Plasma in contact with an insulated interface. A positive space charge in front of the interface forms. Taken from [5]. (*b*) Plasma in contact with the cathode (left) and the anode (right). Taken from [5].

2.4.4. Paschen Curve

Paschen's law provides an equation for the breakdown voltage V_b as a function of the pressure p and the distance d between the two electrodes [12]:

It can be written as follows

$$V_b = \frac{Bpd}{ln(Apd) - ln(ln(1 + \frac{1}{\gamma_{se}}))} \tag{2.8}$$

with A and B being constants and γ_{se} being the second Townsend-coefficient.

The Paschen curve has the following form:

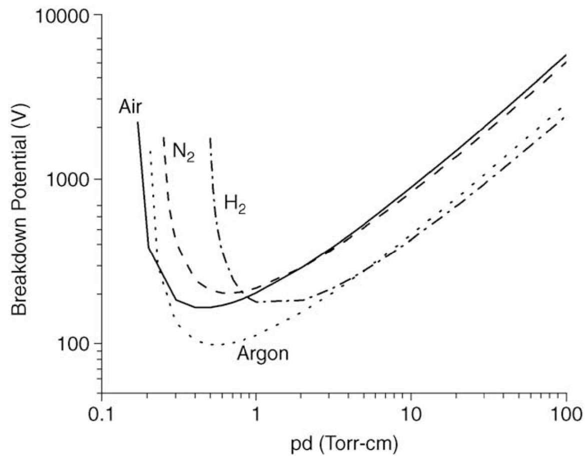

Figure 2.4.: Paschen curves for different working gases. Taken from [5].

It can be understood as follows [5]:

- The lefthanded rise of V_b with low $p \times d$ values is a consequence of two reasons. On the one hand, when d decreases, at one point the electrons get lost to the walls before they can perform ionization. On the other hand, the amount of ionizable gas atoms decreases with decreasing p values, so that at one point a glow discharge cannot be maintained.
- The righthanded rise of V_b with high $p \times d$ is also resulting from two reasons. On the one hand, high d values decrease the energy electrons can take up from the electric field. On the other hand, with higher p values, the mean free path decreases, so electrons can take up less and less energy between collisions.

For magnetron sputtering the Paschen curve can be regarded as guideline only because Paschen's law does not consider an applied magnetic field, which enables the ignition of the plasma at lower pressure values, as will be shown in the following section.

2.5. Magnetron Sputtering

By combining a magnetic and an electric field the path length of the electrons and therefore their lifetime extends before reaching the anode, see section 2.5.1. Thereby, the probability for ionization of the working gas atoms increases. The plasma now only forms in certain regions, depending on the magnetic and electric field configuration. Like this, the effective area of the target, which is sputtered off, can also be controlled.

Caused by the higher electron density and consequently higher ionization rate, the required pressure for the plasma discharge decreases. Lower pressure also means less collisions for the ions on the way to the target resulting in a higher ion impact energy. By using magnetron sputtering, it is possible to achieve higher deposition rates and to deposit larger areas [5].

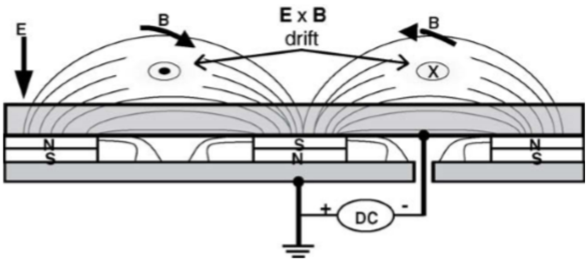

Figure 2.5.: Planar magnetron; permanent magnets are located underneath the planar target. Taken from [5].

These magnetic configurations are called magnetrons. A planar magnetron is shown in Fig. 2.5. A disadvantage of magnetrons is the inhomogeneous erosion only in the area of the plasma tubes, which form at positions where $\vec{E} \perp \vec{B}$ [5], see Fig. 2.5.

In the following the physical basics of their operation mode will be explained.

2.5.1. Physical Background

The following equations and considerations of this subsection are taken from [13]:

The force, which acts on an electron in arbitrary electric $\vec{E}$ and magnetic $\vec{B}$ - fields can be formally described as

$$\vec{F} = q(\vec{E} + \vec{v} \times \vec{B}) = m\frac{d\vec{v}}{dt} \tag{2.9}$$

where $\vec{F}$ is the Lorentz Force, m the particle mass, q the particle charge and $\vec{v}$ the velocity.

When looking at the electric and magnetic contribution separately, one finds that an electron experiences a force anti-parallel to $\vec{E}$ as a contribution of the electric field.

With

$$\vec{v} = \vec{v_\perp} + \vec{v_\perp} \tag{2.10}$$

where $\vec{v_\perp}$ and $\vec{v_\perp}$ are the components of $\vec{v}$ parallel and normal to $\vec{B}$, the magnetic contribution to the Lorentz Force can be written as

$$m\frac{d\vec{v_\perp}}{dt} = q(\vec{v_\perp} \times \vec{B}) \tag{2.11}$$

This equation shows that the acting force on an electron due to the magnetic field is normal to both $\vec{B}$ and $\vec{v_\perp}$. The electron performs gyrational movements in a plane normal to $\vec{B}$ with the Larmor radius r_L of

$$r_L = \frac{mv_\perp}{qB} \tag{2.12}$$

Because of the superposition of the electric and magnetic field, a particle drift, normal to both fields, arises. It can be written as

$$v_{\vec{E \times B}} = \frac{\vec{E} \times \vec{B}}{B^2} \tag{2.13}$$

This drift adds to the magnetic contribution of the particle movement. Thus, in homogeneous crossed electric and magnetic fields, an electron performs cycloidal movements along a plane, see Fig. 2.6. This motion is called the $\vec{\mathrm{E}} \times \vec{\mathrm{B}}$ - drift.

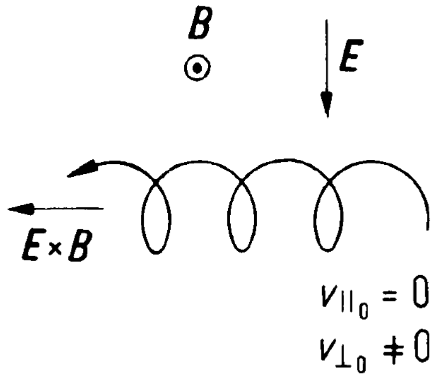

Figure 2.6.: Electron movement in an electric and magnetic field: $\vec{\mathrm{E}} \times \vec{\mathrm{B}}$ - drift. Taken from [4].

Movement in non-homogeneous magnetic fields: A non-uniform magnetic field can be shaped as shown in Fig. 2.5, which is a typical magnetic field distribution for a planar magnetron. The $\vec{B}$ - lines are now curved and therefore also exhibit a $\vec{B}$ - field gradient $\vec{\nabla}\vec{B}$, see Fig. 2.7a. This leads to the curvature and the gradient drifts which always appear together:

The gradient drift can be written as

$$\vec{v_G} = \frac{-|\vec{m}|}{q} \frac{(\vec{\nabla}\vec{B}) \times \vec{B}}{B^2} \tag{2.14}$$

where $|\vec{m}|$ is the magnitude of the magnetic moment which arises because the circular motion of an electron in the $\vec{B}$ - field produces a current which induces a magnetic field similar to a dipole at much larger distances than r_L. Charged particles now perform movements as indicated in Fig. 2.7a.

The curvature drift can be written as

$$\vec{v_c} = \frac{\vec{F_c} \times \vec{B}}{qB^2} \tag{2.15}$$

where $\vec{F_c}$ is the centrifugal force (see Fig. 2.7b) which is now present because of the curved magnetic field lines. The direction of movement of a charged particle is again charge dependent, see Fig. 2.7b.

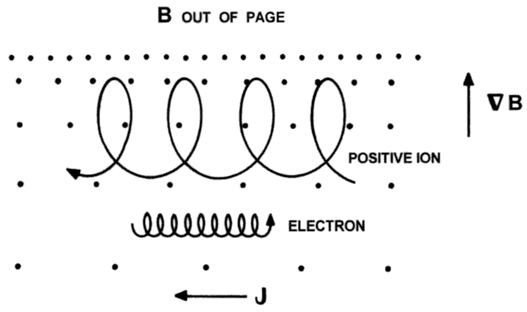

(a)

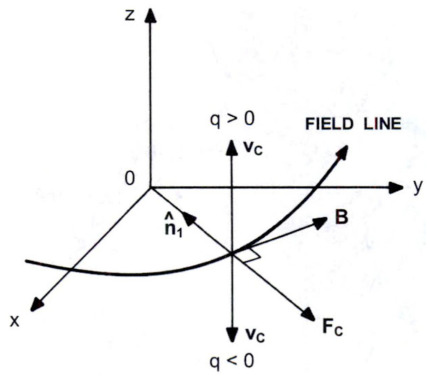

(b)

Figure 2.7.: (a) Gradient drift of electrons and positive ions due to a gradient $\nabla\vec{B}$ in the magnetic field. Taken from [13]. (b) Sketch of the particle curvature drift $\vec{v_c}$. Taken from [13].

Both, the gradient and the curvature drift, point in the same direction and are labelled as v_D in Fig. 2.8. In this Figure it is also indicated, that an electron can be reflected when it moves in the direction of converging magnetic field lines (in this case closer to the target), due to the magnetic mirror effect. Also, the Larmor radius increases when electrons move away from the target, because $\vec{B}$ decreases due to the gradient.

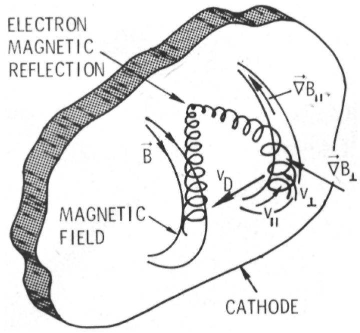

Figure 2.8.: Electron movement due to curved magnetic field lines. Taken from [14].

2.5.2. Unbalanced Magnetrons:

For this kind of magnetron, the magnets are arranged in such a way, that the magnetic field lines are not concentrated only in close vicinity to the target, but they reach into the space of the area in front of the substrate, see Fig. 2.9. The Plasma is therefore not focused directly in front of the target anymore but 'leaks' out into the immediate proximity of the substrate [15].

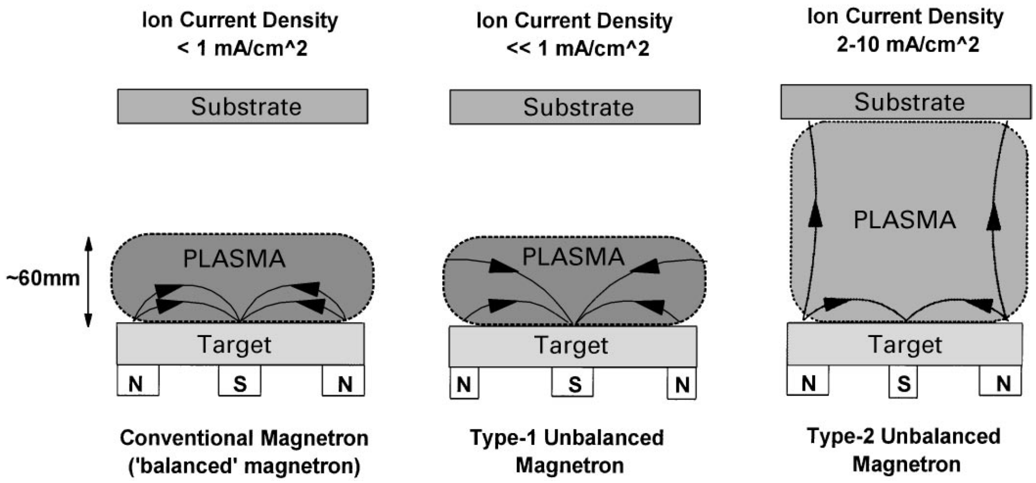

Figure 2.9.: Comparison of balanced and unbalanced magnetrons. Taken from [15].

By applying unbalanced magnetrons, a high ion current reaches the substrate and can be extracted. Additionally, a high current of deposition particles can be provided [15].

Because of the immediate proximity of the plasma to the substrate, an ion platting effect can occur. This has huge effects on the properties of the deposited films [4]:

Weakly bound adsorbates are removed by the constant ion bombardment, which has a 'cleaning' effect. During the film deposition, a constant demolition of the crystal structure occurs and consequently a high concentration of defects is present. Finally, a finely grained, closely packed film develops. Because of the increased ion flux to the substrate, an implantation of working gas atoms is also more likely.

3. Experimental Methods

In this chapter the measurement- and evaluation methods for the current-voltage (I-V) characteristics of different systems as well as the experimental setup for obtaining these are described. The magnetic field of magnetron systems was measured utilizing the Hall - effect and simulated using the finite element method, which are explained. Furthermore, the spatially resolved film thickness measurement technique for thin films deposited on extended substrates is described. Finally, different approaches to measure the temperature on the target are addressed.

3.1. Evaluation Method of the obtained I-V Characteristics

The following expression is commonly used to describe the discharge current of a glow discharge (Fig. 2.1) [14]:

$$I \propto V^n \tag{3.1}$$

where I is the discharge current, V is the voltage and n can be interpreted as an indicator for the electron trapping efficiency, which will be discussed in more detail below.

According to Westwood et al. [16], current values obtained with this equation differ from the real values at low voltages.

As initially done in [16], V_0, the minimal voltage necessary to sustain a discharge, was obtained, from Eq. 3.1: As follows from this equation, straight lines arise when plotting the I-V characteristics in log-log plots. When doing so, n is the slope of the straight line and V_0 can be obtained by extrapolation of the straight-line plot towards zero current.

n varies in a range of 1-10 and depends on parameters like the target, the magnetic configuration and the working gas pressure [16].

A higher n value corresponds to a higher increase of I than for lower n values when increasing the applied power. Therefore, a high n can be interpreted to correspond to a better electron trapping efficiency of the system.

I-V characteristics can also show non-linearity in log-log-plots [14]: By increasing the applied power beyond a certain value the voltage suddenly increases overproportionally. This can have reasons in a too weak magnetic field which causes electrons to escape. Another reason can be a too low pressure at high magnetic field.

3.2. Hall Probe Measurements of the Magnetic Field: Theory and Setup

In this section the operating principle of Hall probes is explained, subsequently the employed Hall probes and magnets are introduced before the measurement setup is described.

The Hall - effect: A Hall probe utilizes the Hall - effect and the Hall voltage is measured [11]:

Simplified, a Hall probe consists of a flat metallic cuboid, which is the active element, see Fig. 3.1.

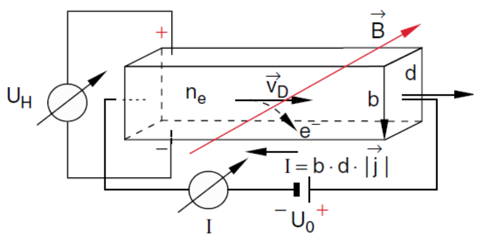

Figure 3.1.: Schematic illustration of the Hall-effect. Taken from [11].

Through the magnetic field $\vec{B}$ to be measured, the Lorentz force $\vec{F}$ acts on the charge carriers n_e of the active element,

$$\vec{F} = n_e e \cdot (\vec{v_D} \times \vec{B}) \tag{3.2}$$

where e is the charge of the charge carriers, $\vec{v_D}$ is their velocity and $\vec{B}$ the magnetic flux.

Because of the acting force $\vec{F}$ the charge carriers are deflected normal to $\vec{B}$ and normal to their direction of motion. This leads to a charge separation resulting in the build up of an electrical field. This field causes a voltage to arise, the so-called Hall voltage U_H,

$$U_H = -\frac{IB}{n_e e d} \tag{3.3}$$

where I is the electrical current and d the side length of the active area, see Fig. 3.1.

U_H is positive for electrons. When the material is primarily characterized by vacancies, a negative Hall voltage is measured.

Employed Hall probes: In this thesis a transverse Hall probe, which measures the transverse part of the magnetic flux with the identification *HHP-NP*, as well as a radial Hall probe, measuring the radial part of the magnetic flux, with the identification *HHP-NA* manufactured by the company *Arepoc* [17], was utilized.

The specifications of the transverse and axial Hall probes are given in table 3.1 and table 3.2 respectively.

Table 3.1.: Specifications for the transverse Hall probe *HHP-NP* from the company *Arepoc* [17].

Operating temperature range:	1,5 K - 330 K
Sensitivity at 297 K:	157 mV/T
Linearity error up to 1 T:	<0,2 %
Active area dimension:	500 µm × 100 µm
overall dimension (w × l × h):	5 mm × 7 mm × 1 mm

Table 3.2.: Specifications for the radial Hall probe *HHP-NA* from the company *Arepoc* [17].

Operating temperature range:	1,5 K - 330 K
Sensitivity at 297 K:	160 mV/T
Linearity error up to 1 T:	<0,2 %
Active area dimension:	500 µm × 100 µm
overall dimension (OD × L):	⌀ 6 mm × 8 mm

Employed Magnets: NdFeB N38 magnets with a magnetization oriented through their thickness (see Fig. 3.2) were provided by the company *ChenYang Technologies GmbH & Co. KG*.

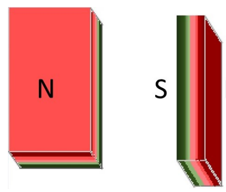

Figure 3.2.: Schematic of the employed NdFeB N38 block magnets. The red (north) and green (south) color indicate how the magnetization is oriented through their thickness.

On their website [18] the following specifications are given:

Table 3.3.: Specifications for the NdFeB N38 magnets from the company *ChenYang Technologies GmbH & Co. KG* [18].

maximum working temperature (°C):	80
Remanence (T):	Nom: 1,26 Min: 1,22
Coercivity (kA/m):	Nom: 925 Min: 900

Setup: The setup for the Hall probe measurements is given in Fig. 3.3

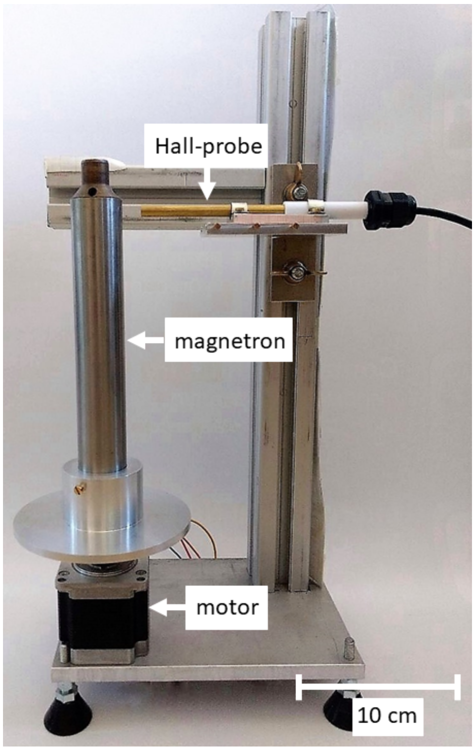

Figure 3.3.: Setup for the Hall probe measurements. The Hall-probe, the magnetron and the motor are shown.

Both investigated magnetron types were mounted on a motor, which was controlled by a *LabVIEW* program. The Hall probe was connected to the computer via the USB module *USB2AD* [17]. After every rotational step of the motor the program recorded the output value of the Hall probe.

Despite all efforts, a very low precession when turning the magnetron around its axis between the Hall probe and the measured magnetron could not be avoided. Because of this, measurement errors occurred.

Measuring the magnetic field of the modular cylindrical magnetron: This magnetron was measured for two of its segments in its original design and also twisted to its maximum, which is 30°, see section 4.3.1. Both, the transverse and radial Hall probe were used. For these systems two dimensional measurements of the magnetic field were performed too. The measuring distance started from 0 mm and went to 15 mm. During a 360 ° turn, a measurement was taken every 4 °.

Measuring the magnetic field of the magnetron for inner coatings: The investigation of the magnetic field of the magnetron for coatings on the inner surfaces of narrow tubes (from now on called "internal" coatings) was done solely by using the transverse Hall probe.

Depending on the normal or parallel orientation of the active area in respect to the magnets, the transverse or radial component of the magnetic field could be measured.

To achieve a two dimensional measurement of the magnetic field in exactly the mid-plane of the magnetron, the following approach was applied: The closest distance between the probe and the magnets was 3 mm. A 360 ° turn of the magnetron was measured in 4 ° steps. After this, the Hall probe was moved 1 mm closer to the center until the center (half of the linear extension of the magnetron) was reached.

3.3. Simulation of the Magnetic and Electric Field

For the simulation of the magnetic field of a magnetron assembly, *FEMM (Finite Element Method Magnetics)* [19] was used. This is a freely available software for solving two-dimensional magnetics, electrostatics and heat conduction problems using a finite element approach.

Magnetostatic Problems: As described in the *FEMM* Reference Manual, which can be found under *Documentation* in [19], magnetostatics problems like in the case of a magnetic field of a magnetron, are solved by finding a solution for the following equations:

$$\vec{\nabla} \times \vec{H} = \vec{J} \tag{3.4}$$

$$\vec{\nabla} \cdot \vec{B} = 0 \tag{3.5}$$

$$\vec{B} = \vec{\nabla} \times \vec{A} \tag{3.6}$$

where $\vec{H}$ is the field intensity, $\vec{J}$ is the current, $\vec{B}$ is the flux density and $\vec{A}$ the magnetic vector potential.

The following equation is then solved:

$$\vec{\nabla} \times (\frac{1}{\mu(B)} \vec{\nabla} \times \vec{A}) = \vec{J} \tag{3.7}$$

where $\mu(B)$ is the permeability as a function of $|\vec{B}|$.

Electrostatic Problems: In the *FEMM* Reference Manual in [19] it is also discussed, how electrostatic problems are solved by considering the following equations:

$$\vec{\nabla} \cdot \vec{D} = \rho \tag{3.8}$$

$$\vec{\nabla} \times \vec{E} = 0 \tag{3.9}$$

$$\vec{E} = -\vec{\nabla} V \tag{3.10}$$

where $\vec{D}$ is the electric flux density, $\vec{E}$ the electric field intensity and V a scalar potential. $\vec{D}$ and $\vec{E}$ are related in vacuum through the electrical permittivity ϵ_0 by $\vec{D} = \epsilon_0 \vec{E}$. Thus, substituting in Eq. 3.8 yields

$$-\epsilon_0 \nabla^2 V = \rho \tag{3.11}$$

The finite element approach is designed to convert a single element problem with complex geometry into a problem with a high number of elements but with simple geometry, and therefore easier solvability. These elements with simple geometry can be squares or triangles. Further information can be found in [19, 20].

3.4. Film Thickness Measurements: Optical Transmission

Using a transmitted light scanner (*Epson: Epson perfection V750 PRO*), the film thickness of a sample can be determined by evaluating the intensity of the light at given wavelengths transmitted through a transparent scanned sample. For the evaluation, the custom developed program *Thin Film Inspector*, was used.

With this program, as explained in the masters thesis of Mahr [21], the transmissivity of thin transparent metallic films for three defined wavelengths, namely 650 nm, 550 nm and 450 nm, which correspond to the three colors red, green and blue, can be determined spatially resolved. Like this, one obtains a film thickness distribution of the sample by employing the Beer Lambert law.

To disentangle the transmittance spectrum of the film from that of the substrate, an uncoated substrate is needed as a reference. This reference then corresponds to a transmittance of one. Also, a dark reference with a transmittance of zero must be provided.

3.5. EDX - Energy Dispersive X-ray Spectroscopy

As explained in [22], with EDX, X-rays are detected which arise from the following process: When bombarding a material-surface with electrons they can eject electrons from inner shells. When the created electron hole is filled with an electron from an outer higher energy shell the energy difference can be released in the form of X-rays. These have a characteristic energy, dependent on the specimen, and therefore the elemental composition of a material can be determined. X-rays emerge from a depth of around 500 nm, depending on the material and the primary electron energy.

3.6. Temperature Measurements

The temperature was measured on the substrate as well as on the target in the case of coating internal surfaces of narrow tubes. In this section the employed measurement-techniques are introduced.

3.6.1. Temperature Indicating Labels

The company *TMC Hallcrest* provides self-adhesive temperature indicator stripes with the indication *Thermax*, which were employed only for target-temperature measurements. One of these stripes consists of several indicators, each for a discrete temperature value. With these stripes a temperature range from 77 °C to 204 °C is covered in discrete temperature-steps of up to 11 °C per step.

The maximum temperature the stripe was exposed to can be read off from the change of colors of the indicators from white/yellow to black. These indicators were attached directly to the target, which had the form of a concentric wire in the center of a tube, close to the area, which was exposed to the plasma.

3.6.2. Pt100 resistance temperature detector

In this thesis, a Pt100 from the company *RSpro* was used, which was also utilized for target-temperature measurements only. The sensor is a platinum resistance temperature detector (RTD) with a 100 Ω resistance at 0 °C and uses the temperature dependence of the resistance of platinum. It is applicable in a temperature range of -50 °C to 250 °C. A Pt100 is very sensitive to external voltages. It needs to be isolated very carefully when mounting it directly on the target, which is on high voltage during the sputter process. Fig. 3.4 shows the wire-target as well as the Pt100 element which was attached with a thin wire to a Kapton insulated part of the Cu target-wire and additionally insulated with Teflon.

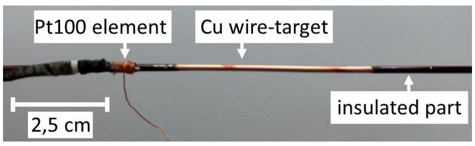

Figure 3.4.: Pt100 element attached to a Cu wire-target.

3.6.3. Thermocouple Type K

With a thermocouple type K the temperature on the substrate was measured. It consists of two wires out of different metals which are connected at the end. The temperature is measured by utilization of the thermoelectric effect [11].

4. Modular Cylindrical Magnetron

The first part of this thesis is devoted to segmenting an already existing cylindrical magnetron assembly into repeatable units, so that basically magnet-assemblies of arbitrary length can be formed. In the following, the design of the non-segmented magnetron is described, before turning to the considerations on the design of the modular magnetron. Finally, the results of the Hall probe measurements, the simulations of the magnetic field, the plasma formation and the I-V characteristics of the modified system are presented.

4.1. Existing Cylindrical Magnetron

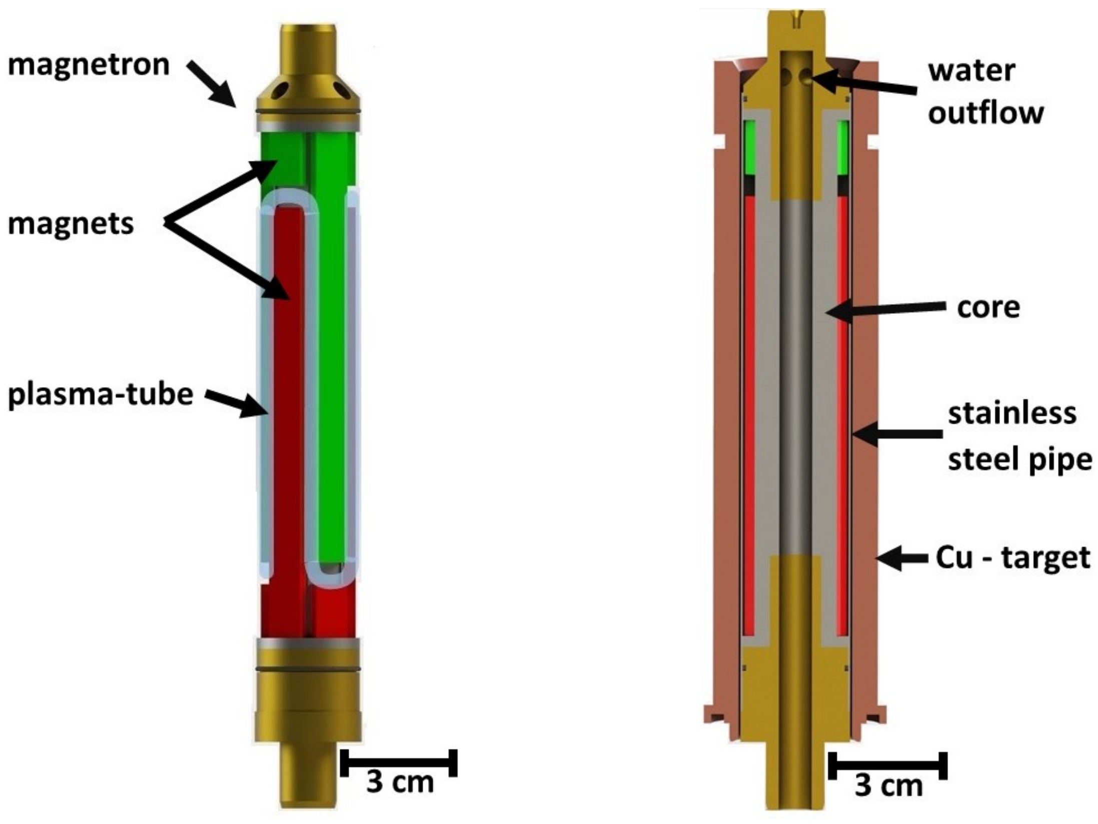

(a) (b)

Figure 4.1.: Renderings of a cylindrical magnetron. The red and green blocks represent differently orientated magnets. in (a) the blue line indicates how the meander-shape plasma-tube develops on the outer target-surface and (b) a cross-section of the cylindrical magnetron concentrically inside a cylindrical target.

Fig. 4.1 shows the existing magnetron. Its core consists of a magnetic material, in this case construction steel (ST37), in a hexagonal cylindric geometry. A magnetic material is chosen because magnets can be attached easily, also, it confines the magnetic field lines at the side where the magnets are attached. The top and the bottom part consist of brass and fulfill functional needs. NdFeB block magnets (see section 3.2) are attached to the core, in a special formation (see Fig. 4.1a), so that a meander-shaped plasma-tube (blue transparent line) develops on the outer surface of a hollow cylindrical target, see Fig. 4.1b. The magnetron rotates inside this target to ensure a uniform erosion of target-material.

Because of high temperatures arising during a high power sputter-process and the limited temperature resistance of the magnets (maximum working temperature: 80 °C), a water-cooling system is included in the magnetron design. The cross-section of the magnetron depicted in Fig. 4.1b shows a concentrical pipe in its center. Through this pipe, water is pumped during the sputter process, which is distributed through openings on the top of the magnetron and flows downward between the magnetron and the inside of the target, before it is drained from the system. Therefore, the magnets need to be protected with a stainless steel pipe, forming the outside of the magnetron, to prevent corrosion.

4.2. Design of Two Modular Magnetron Models

To modularize the existing magnetron its core was segmented, the brass top and bottom parts had to be adapted accordingly. The magnet-configuration stayed the same, the length the plasma-tube runs straight varies with the magnetron-length.

Segmentation of the existing magnetron held two difficulties. The first is the small diameter of the core and the second is the necessary water-tightness of the segmented magnetron to the outside.

Two systems were designed, which both consist of 25 mm long segments made from construction steel (ST37).

The two models differ in the form of realization of the link between the segments and the solution for the water-seal. One model is completely divisible, whereas the other model consists of a non-divisible inner tube on which the segments are strung along.

Both models consist of two end-pieces and up to 3 central-segments. The magnetic configuration of the end-pieces is shown in Fig. 4.2.

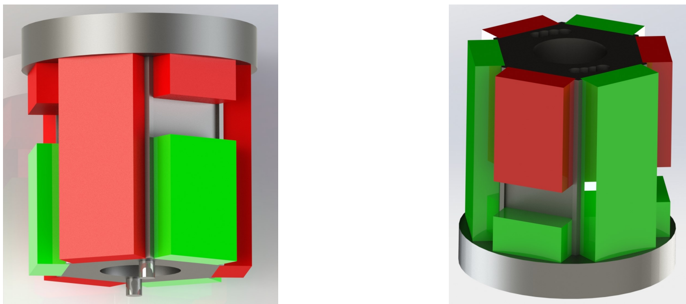

(a) (b)

Figure 4.2.: Renderings of the (*a*) top and (*b*) bottom end-piece. Shown for model 2.

The section closest to the upper or lower end of the end-pieces consists of magnets with different length oriented the same way all around the circumference of the end-segments. With a distance of about 4 mm to the shorter end-magnets, magnets with different orientation are attached to the end-pieces. As will be discussed in section 4.3.3, plasma forms between two differently oriented magnets. Like this, the shorter magnets redirect the plasma and therefore a closed plasma-tube forms, see Fig. 4.5. As mentioned above, between the end-pieces, the two models developed for this thesis consisted of up to 3 central-segments. However, systems containing an arbitrary number of central-pieces can be created. The construction of the central-segments is subsequently described.

Model 1: The design drawing of a segment is shown in Fig. 4.3. The segments are sealed with sealing rings for water-tightness at their link. They are plugged together and connected with three screws (blue arrows in Fig. 4.3). The red arrows indicate the mountings of this segment to the one before, which is not shown. The same screw assembly is also used to fix the top and bottom brass parts. This leads to a strict order of assembly from bottom to top.

The advantage of this model is the complete divisibility. The disadvantage is the more difficult assembly compared to the second model and the lack of water-tightness in case of incorrect assembly at the sealings.

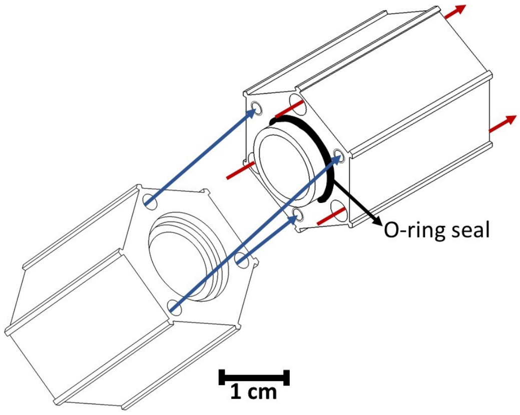

Figure 4.3.: Assembly of model 1. The blue arrows indicate where screws mount the left segment to the right one. The red arrows show where the right segment is mounted to the one before. An O-ring seal ensures water-tightness at the link between the segments.

Model 2: The design drawing of a segment is shown in Fig. 4.4. The individual segments are strung onto an inner pipe (which is not shown in Fig. 4.4). The segments have pins on their bottom and indentations on their top. Depending on which indentation is chosen for a pin when linking two segments, a twist of 0 °, 10 °, 20 ° or 30 ° arises between them, compare Fig. 4.4. This twist yields an extension of the plasma-tubes, see section 4.3.3.

Strong forces arise when bringing two magnets together, which are oriented in the same direction. The pins help keeping an individual segment in its place, as does a screw, which fixes the top segment to the inner pipe.

The advantage of this approach is the easier assembly, the complete water-tightness due to the continuous pipe and the possibility to twist the modules relative to each other. The disadvantage is that the magnetron is not completely modular, because of the non-separable inner pipe.

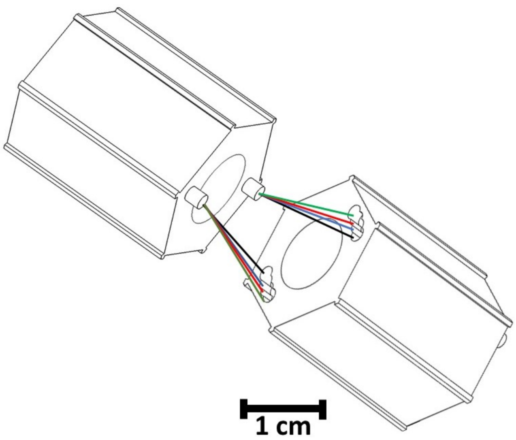

Figure 4.4.: Assembly of model 2. The segments are strung onto an inner pipe, which is not shown. Connecting the two pins to different indentations leads to different twists: black line 0 °, blue line 10 °, red line 20 ° and green line 30 °.

4.3. Magnetic Field Characterization

The magnetic field distribution was measured using a Hall probe, see section 3.2, and simulated with the program *FEMM* [19], see section 3.3. The measurement and the simulation were then compared.

4.3.1. Hall Probe Measurements

The Hall probe measurements were conducted as explained in section 3.2. Due to the identical magnet configuration for both models, Hall probe measurements were only conducted for model 2. The magnetron for the measurements consisted out of two end segments, see Fig. 4.5, and was measured in the mid-plane (see red line) in two configurations, with non-twisted segments (Fig. 4.5a) and segments twisted to 30 ° (Fig. 4.5b) against each other. It is assumed, that the field configuration at this position between the end pieces is also representative for positions in longer multi-segment assemblies, for both straight and twisted segment-joints.

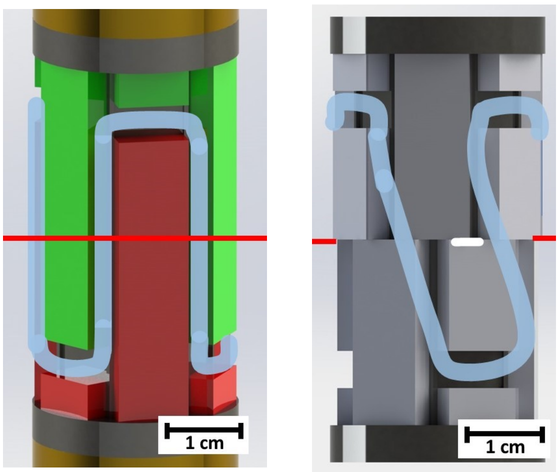

(a) (b)

Figure 4.5.: Magnet configuration of a magnetron with 2 segments, the red line marks the mid-plane, where Hall probe measurements were performed: (*a*) non-twisted. The red and green colors of the magnet indicate the different orientation. The blue line indicates how the meander shaped plasma develops. (*b*) twisted by 30 °. The white line marks the additional length of the plasma-tube (see below).

The results are shown in Fig. 4.6 and Fig. 4.7.

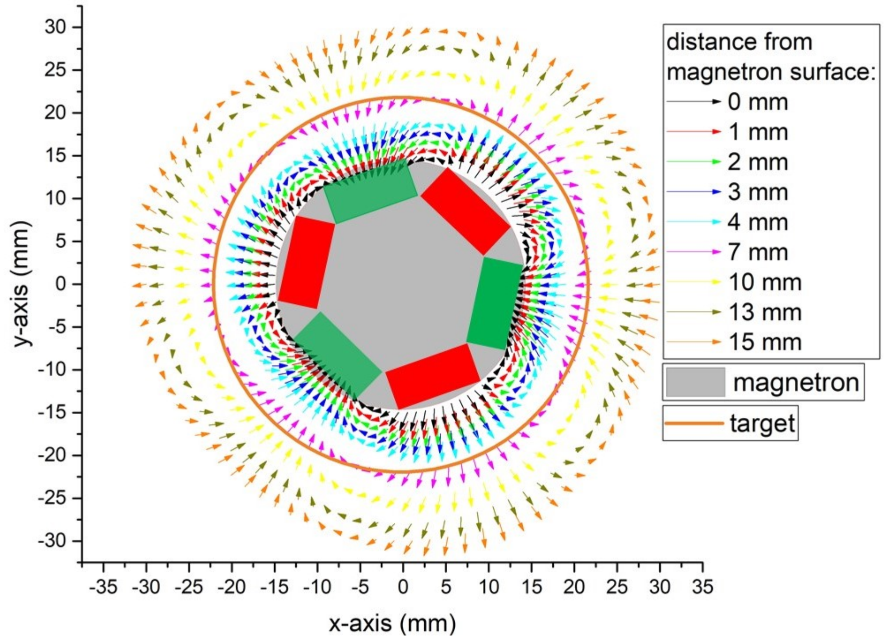

Figure 4.6.: Magnetic field of a non-twisted magnetron consisting of two segments, measured in the mid-plane. The rectangles represent the magnets in north (red) and south (green) orientation.

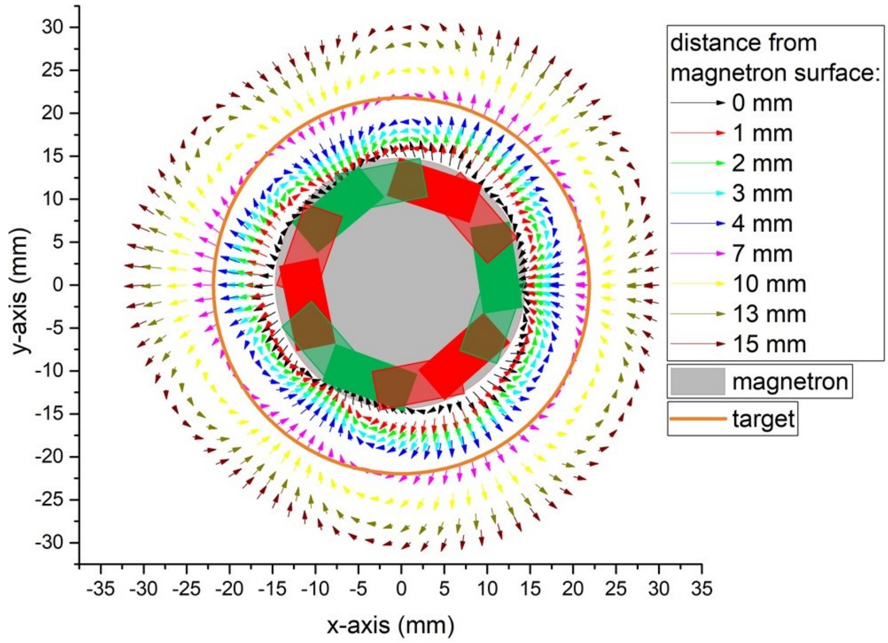

Figure 4.7.: Magnetic field distribution of a magnetron with 2 segments twisted by 30 °, measured in the mid-plane. The rectangles represent the magnets in north (red) and south (green) orientation. The transparent rectangles indicate the magnets of the second segment which was twisted by 30 °.

Because magnets with opposite orientation are always neighboring, magnetic field lines close between them. At the distance corresponding to the target surface, the magnetic fields of both configurations show close resemblance.

Fig. 4.8 shows the decrease of the magnetic field strength starting from the center of the surface of a magnet in the mid-plane of the non-twisted system over a distance of 15 mm. The black line marks the target-surface. At this point the magnetic field strength is about 30 % of its initial value. The red line corresponds to a simulation made by the program *FEMM*, see section 4.3.2.

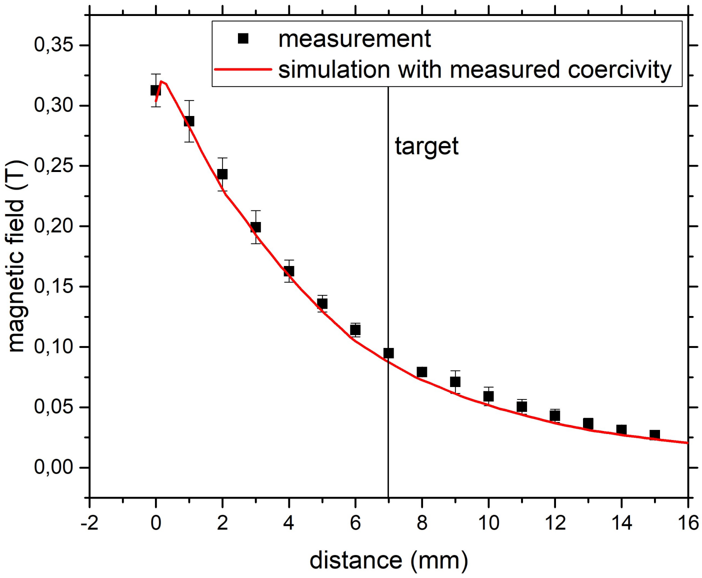

Figure 4.8.: Decrease of the magnetic field strength over a distance of 15 mm, measured from the center of the magnet. The red line is the simulation (using *FEMM* see 4.3.2) with the coercivity value, which was calculated from the measurement. The black line marks the target-surface. Statistic from 3 magnets.

4.3.2. Simulation of the Magnetic Field

Simulations of the magnetic field were performed using the program *FEMM*. Fig.4.9 shows the simulation of the magnetic field line distribution for the non-twisted geometry. It is not possible to simulate the twisted assembly, because *FEMM* is only capable to treat geometries which can be mapped to a 2D situation.

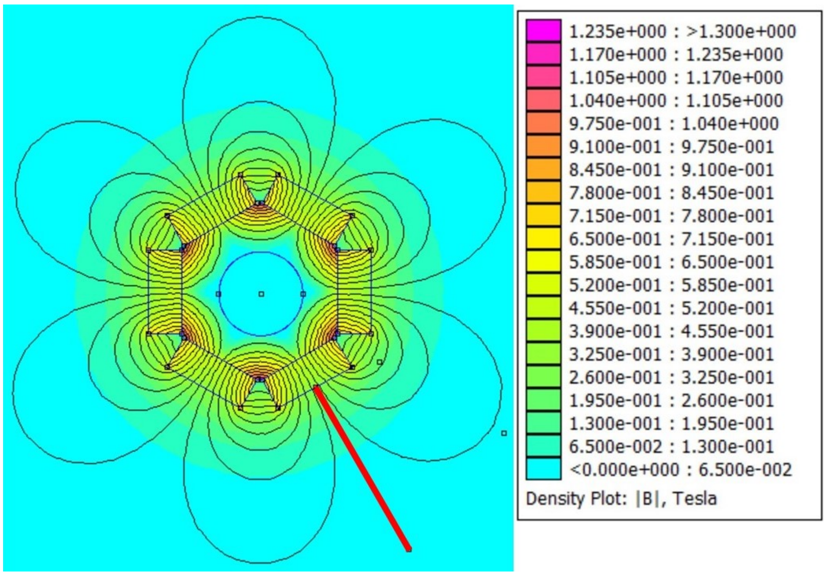

Figure 4.9.: Two dimensional simulation (using *FEMM*) of the magnetic field line distribution of a plane of the magnetron. The core consists of magnetizable construction steel. For the simulation the coercivity value of 676546 A/m, which was calculated from the measurement (explained below), was used. The red line indicates the position of the measurement-line used in Fig. 4.10.

Along the red line in Fig.4.9 the magnetic field strength is plotted in Fig. 4.10.

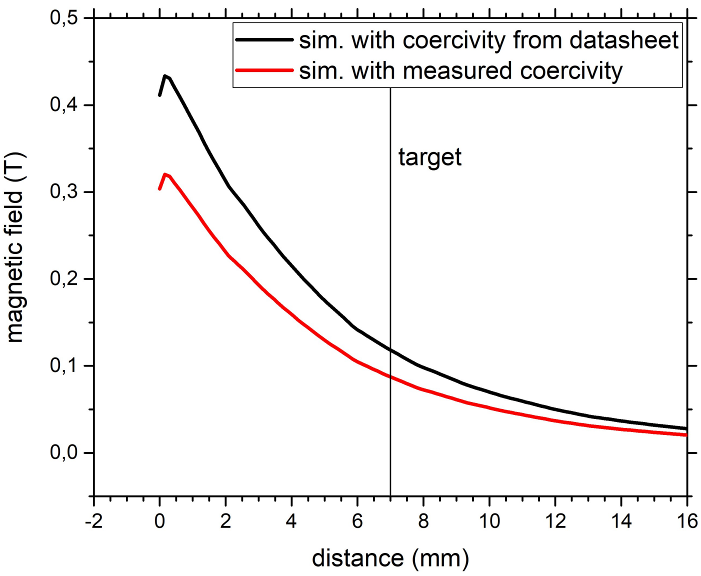

Figure 4.10.: The black line represents the simulation with the coercivity value of 900000 A/m from the datasheet of the magnets, see section 3.2. The red line represents the simulation with the calculated value for the coercivity of 676546 A/m from the measured magnetic field at the surface of a magnet in the magnetron configuration. The vertical black line marks the surface of the target.

The black line represents the magnetic field strength decrease over the distance for the stated value in the datasheet of the block magnets for the minimal coercivity (900000 A/m) with a minimal remanence of 1,22 T, see section 3.2. The red line represents the simulation with a coercivity value calculated from a Hall-probe measurement. For this line, the magnetic field strength was measured directly on the surface of a magnet in the magnetron configuration. The value for the magnetic field strength of a magnet at this position was also taken from the simulation with the coercivity-value of 900000 A/m from the datasheet. From the difference in value, the coercivity, which corresponds to the measured magnetic field strength value, was assessed. This yielded a coercivity of 676546 A/m and from this a remanence of 0,89 T was calculated.

Also, the magnetic field with a non-magnetic stainless steel core was simulated. It is depicted in Fig. 4.11.

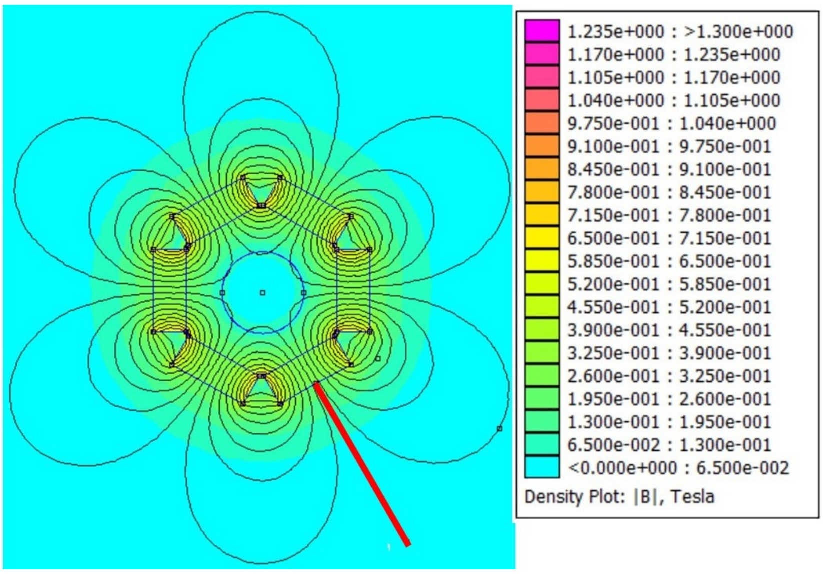

Figure 4.11.: Two - dimensional simulation (using *FEMM*) of the magnetic field line distribution of a plane of the magnetron. The core consists of non-magnetic stainless steel. For the simulation the coercivity value, which was calculated from the measurement, was used. The red line indicates where the decrease of the magnetic field was plotted in Fig. 4.12.

Fig. 4.12 shows the difference in the decrease of the magnetic field strength over the distance from the magnet, for the different core materials. The black line represents a magnetron configuration with a non-magnetizable stainless steel core whereas the red one represents a configuration with a magnetizable construction steel core. It is clearly visible that the trapping of the field lines by the magnetic core enhances the field strength outside the magnetron.

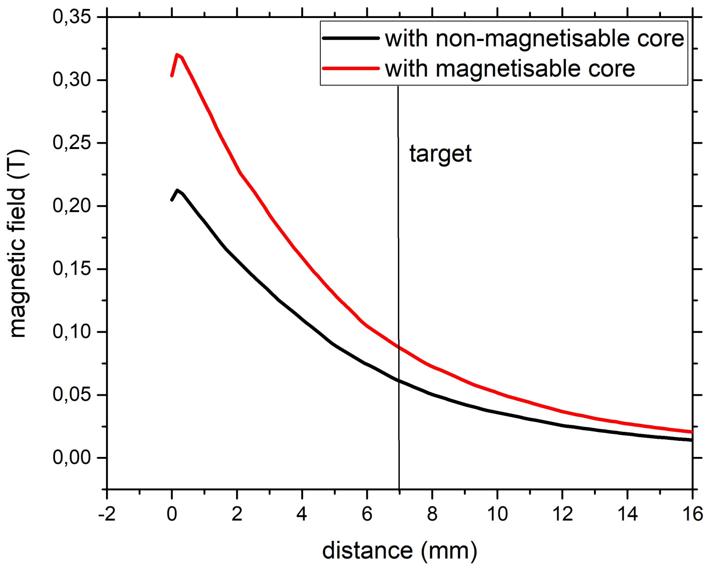

Figure 4.12.: Simulation of the magnetic field decrease along the red line in Fig. 4.9 and Fig. 4.11 with the measured coercivity of 676546 A/m. The red line corresponds to a magnetron configuration with a magnetizable core. The black line corresponds to a magnetron configuration with a non-magnetizable core. The vertical black line marks the surface of the target.

4.3.3. Plasma Development

High ionization probability occurs in areas with a high concentration of electrons. A situation like this can be realized when electrons are trapped in certain areas for a period of time. For magnetrons this is usually achieved by deliberately implementing the $\vec{E} \times \vec{B}$ - drift, see section 2.5.1. A very efficient confinement of electrons occurs when the electron drift can form a closed curve [14]. A ring-current develops, and electrons are solely lost due to collision processes and other arising drifts, occurring for example due to curvatures and gradients of the $\vec{B}$ - field (see section 2.5.1).

In a magnetron configuration like discussed before, the plasma forms between two neighboring magnets on the target surface, compare the blue line in Fig. 4.5. This can be understood as follows:

As described in section 2.5.1, charged particles experience the Lorentz force when moving through an electric and magnetic field. In the investigated system it is assumed that the electric field develops radially from the chamber walls, which serve as anode, to the target.

From the electric field electrons experience a force $q\vec{E}$ and drift along the field lines towards the chamber walls. The $\vec{B}$ - field lines are curved in opposite direction of the $\vec{E}$ - field (convex). Electrons accumulate at areas of the magnetic field lines where the $\vec{B}$ - field is perpendicular to the $\vec{E}$ - field and they now only experience the $\vec{E} \times \vec{B}$ - drift perpendicular to both, the electric and magnetic field. The convex curvature of the magnetic field lines additionally confines the electrons.

For the present magnet assembly the plasma-tube forms in a meander-shaped closed electron-current because of the magnet configuration in the end pieces (see section 4.2). The transformation of the meander-shaped closed current to a ring-current is indicated in Fig. 4.13.

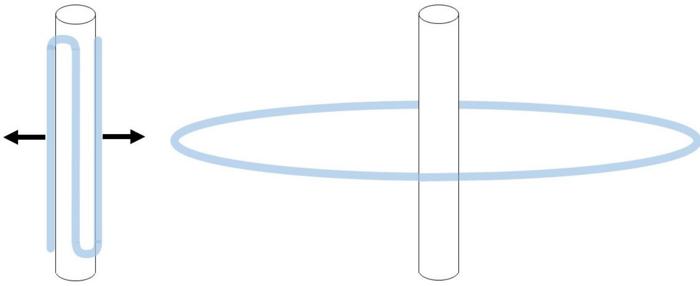

Figure 4.13.: Transformation of the formed meander-shaped closed plasma-tube into a ring - current.

Fig. 4.14 shows how the plasma - tube develops in the non-twisted (compare Fig. 4.5a) and twisted system (compare Fig. 4.5b) with 2 segments.

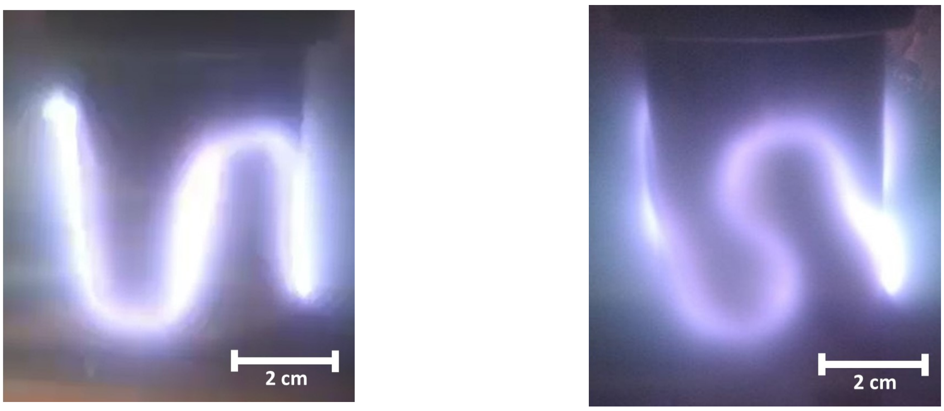

(a) (b)

Figure 4.14.: (*a*) Plasma formed by a magnetron with 2 end-segments. (*b*) Plasma formed by a magnetron with 2 end-segments, which were twisted among each other by 30°.

4.4. I-V Characteristics

All I-V characteristics were recorded with model 2, because its non-twisted state corresponds to the configuration of model 1.

The characteristics were recorded for several configurations of model 2: The number of segments was varied between 2 and 5. For each of these the degree of twist of the segments relative to each other was varied from 0° to 30° in 10° steps.

To be able to compare magnetrons with a different number of segments and degree of twist, the electric current had to be replaced by the electric current-density in the I-V plots.

For the calculation of the current-density, the area of the target, which was covered by the plasma-tube had to be determined. This area was roughly estimated in the following way:

From observations during several sputter processes it was apparent how the meander-shaped plasma-tubes formed, see Fig. 4.14. A mean plasma-tube diameter of 10 mm was assumed. For the curvature of the plasma-tube at its ends, a semicircle with a radius of 10 mm was estimated. Depending on the degree of twist of the segments against each other, the length of the plasma-tubes varied, see Fig. 4.14b. The (additional) length was roughly estimated by measuring the length of the white line in Fig. 4.5b for each degree of twist. The resulting plasma-tube-areas for all magnetron configurations are given in Table 4.1.

Table 4.1.: Different resulting plasma-tube-areas for all examined magnetron configurations. With decreasing number of segments, the sputtered-off target area decreases given by the decreasing height of the plasma-tube.

segments	target area (mm^2)	twist (°)	plasma-tube area (mm^2)
2	4382,52	0	1884,6
		10	2064,6
		20	2244,6
		30	2424,6
3	7916,81	0	3384,6
		10	3564,6
		20	3744,6
		30	3924,6
4	11451	0	4884,6
		10	5244,5
		20	5604,6
		30	5964,6
5	14985	0	6384,6
		10	6924,6
		20	7464,6
		30	8004,6

Experimental Setup The I-V characteristics were recorded by reading off the current and voltage value, which were applied by the DC-source, after setting a power value. A Cu target was utilized and the magnetron rotated with 13 revolutions per minute.

The cylindrical magnetron was measured in a vacuum chamber with a base pressure of 10^{-5} Pa. An Ar pressure of 0,4 Pa, 0,7 Pa, 1 Pa, 1,5 Pa or 2 Pa was applied and was measured by a Baratron gauge with the specification *627BX01TDC1B* from the company *MKS Instruments*.

The employed DC-source was a *Pinnacle^{TM} 10 kW* from the company *Advanced Energy*.

The source has a maximal power output of 10 kW, a maximal voltage output of 400 V to 800 V and a maximal current output of 25 A to 12,5 A.

The I-V characteristics for rotating magnetrons with a different number of segments were recorded up to different power values (compare Table 4.2) corresponding to approximately the same power-density.

Table 4.2.: Showing the applied power-range and the power-value steps for which the different magnetron configurations were recorded.

	2 segm.	3 segm.	4 segm.	5 segm.
appl. power (W)	100 -1300	200 - 2500	300 - 3600	500 - 5000
in steps of (W)	100	200; 300	200; 300	500

4.4.1. Measurements and Results

The obtained I-V characteristics were fitted with Eq. 3.1 in section 3.1. The values for the slopes n of the characteristics in log-log-plots, which can be interpreted as an indicator for the trapping efficiency of magnetrons [14, 16] and the minimum voltage V_0, which is required to sustain the discharge [16] (see section 3.1) for different configurations, are given in Table A.1 in the Appendix A.1. To receive V_0 by extrapolation of the log-log-plots, a minimum current of 0,1 A was assumed. However, many characteristics showed no sufficient linearity to obtain reasonable results.

In the following, the obtained I-V characteristics for the different magnetron configurations are compared, analyzed and interpreted.

Magnetron Configuration with 2 Segments: In contrast to the other configurations (see below), the I-V characteristics of the configuration with 2 segments show consistent linear behavior. With the degree of twist the characteristics become more pressure-dependent and separate from each other, although this effect decreases with increasing pressure, see Fig. 4.15.

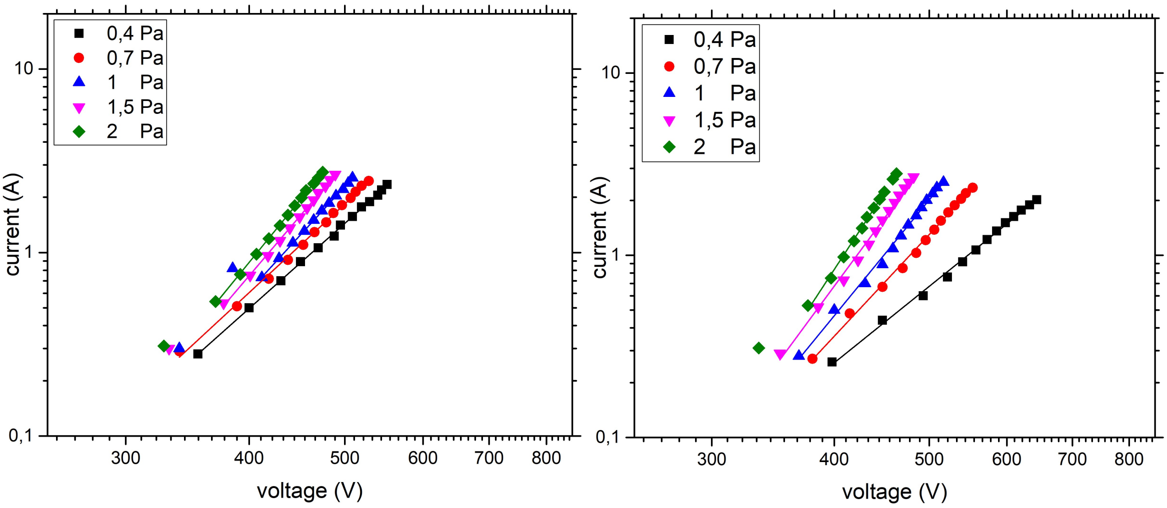

(a) (b)

Figure 4.15.: I-V characteristics of the configuration with 2 segments twisted by (*a*) 0 ° and (*b*) 30 ° recorded at different pressures.

n increases with increasing pressure from 0,4 Pa to 2 Pa. Also, n has the highest values for the systems twisted by 30 °, see Fig. 4.16b, for pressures down to 0,7 Pa (mean $\bar{n} \approx 6,21$). This is in contrast to the behavior of the other configurations.

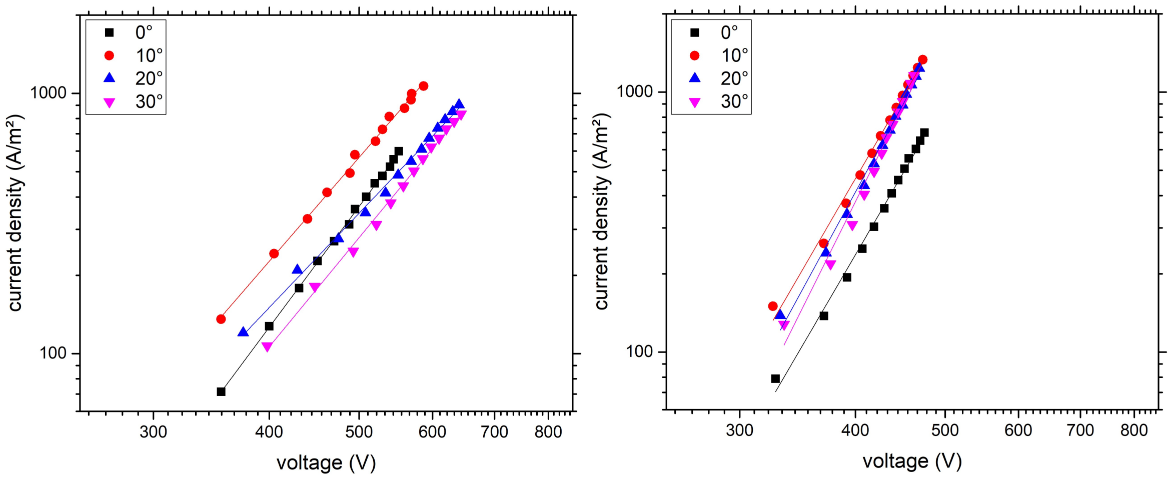

(a) (b)

Figure 4.16.: I-V characteristics recorded at (*a*) 0,4 Pa and (*b*) 2 Pa showing the pressure dependence of the twist of a magnetron with 2 segments.

The current-density as a function of the current and the pressure shows higher dependence on the degree of twist among the segments than for the other configurations (see below). With a twist of 0 ° the current-density exhibits the highest value, see Fig. 4.17.

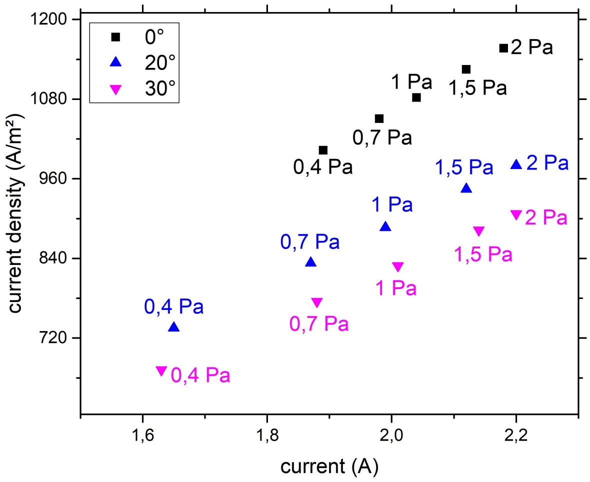

Figure 4.17.: Increasing current-density with pressure. Recorded at a power of 1000 W for a 2 segmented magnetron with a twist of the segments relative to each other of 0 °, 20 ° and 30 °.

Configurations with 3, 4, and 5 Segments: The I-V characteristics of the configurations with 3, 4, or 5 segments show strong dependence on parameters like pressure and degree of twist. In general, with increasing pressure, n increases, the linearity and the stability of the characteristics increase and therefore higher applied powers are reachable, see Fig. 4.18 and Fig. 4.19.

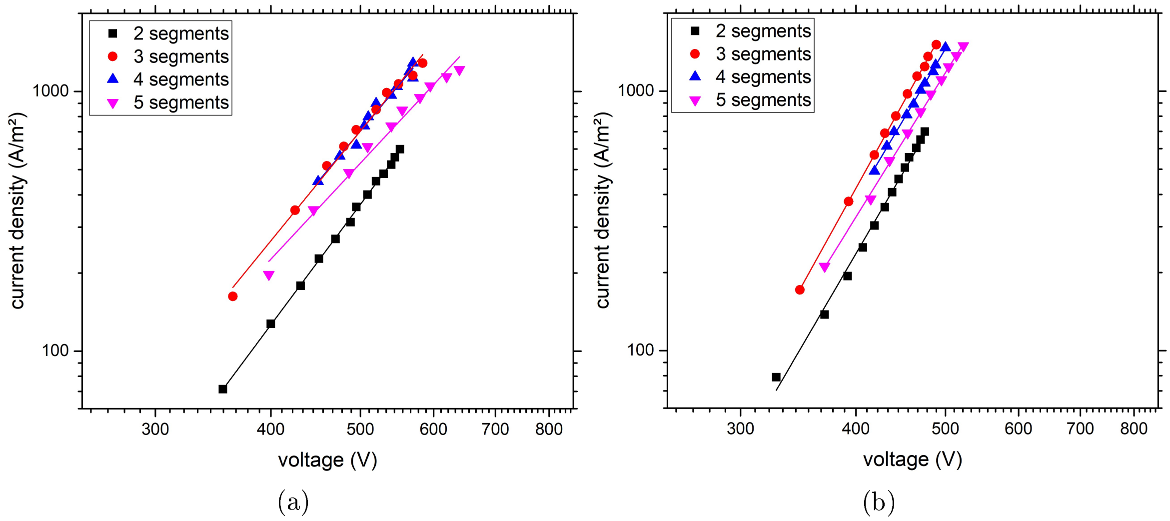

Figure 4.18.: I-V characteristics of configurations with different number of segments twisted by 0 ° among each other at a pressure of (a) 0,4 Pa and (b) 2 Pa.

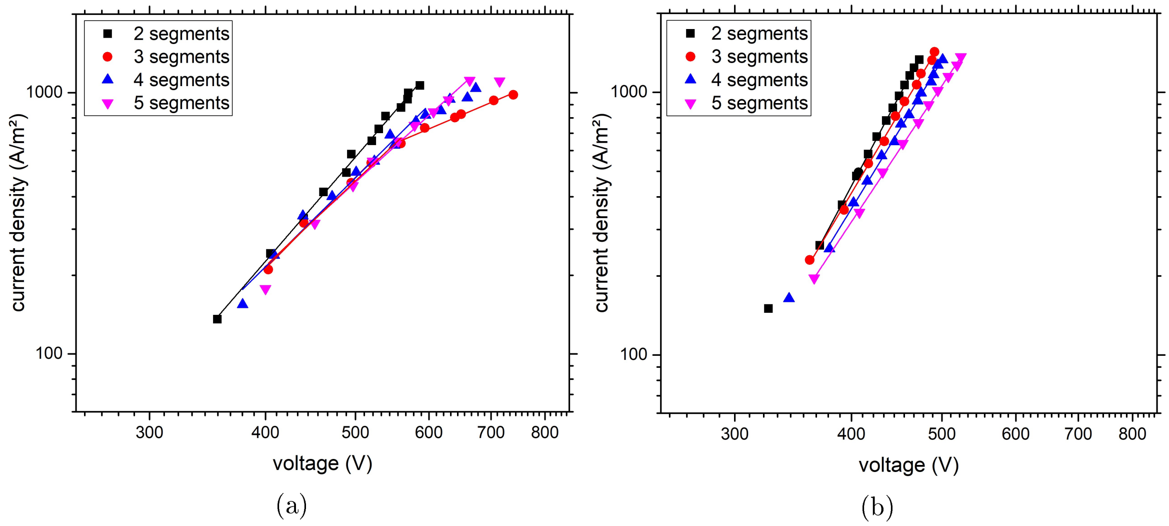

Figure 4.19.: I-V characteristics of configurations with different number of segments twisted by 10 ° among each other at a pressure of (*a*) 0,4 Pa and (*b*) 2 Pa.

In Fig. 4.20 and Fig. 4.21 the I-V characteristics are shown for the configurations with 3 and 5 segments for a twist of 0 ° and 30 °.

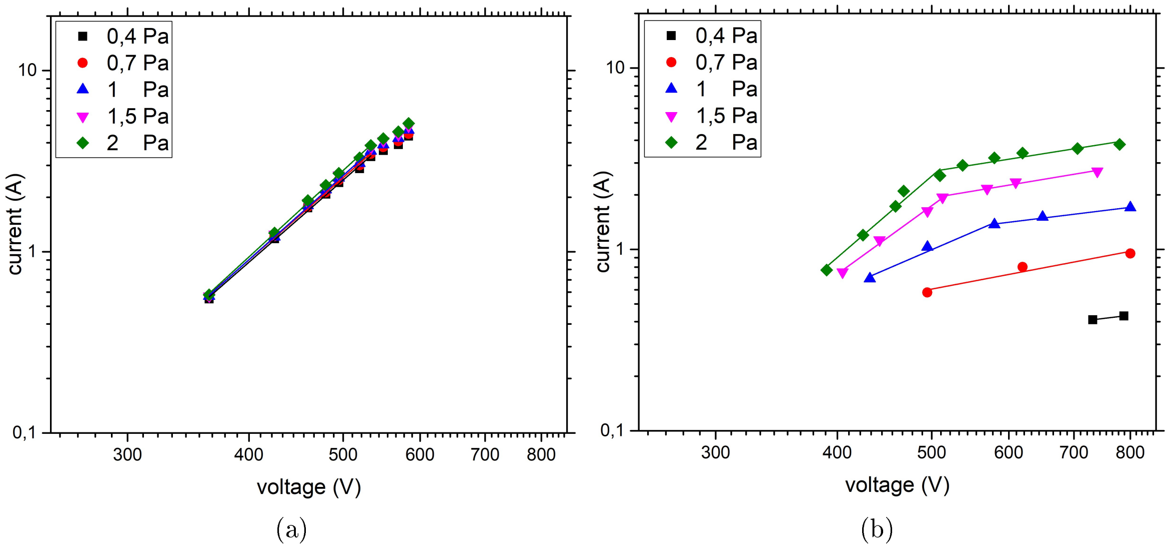

Figure 4.20.: I-V characteristics of the configuration with 3 segments twisted by (*a*) 0 ° and (*b*) 30 °, recorded at different pressures.

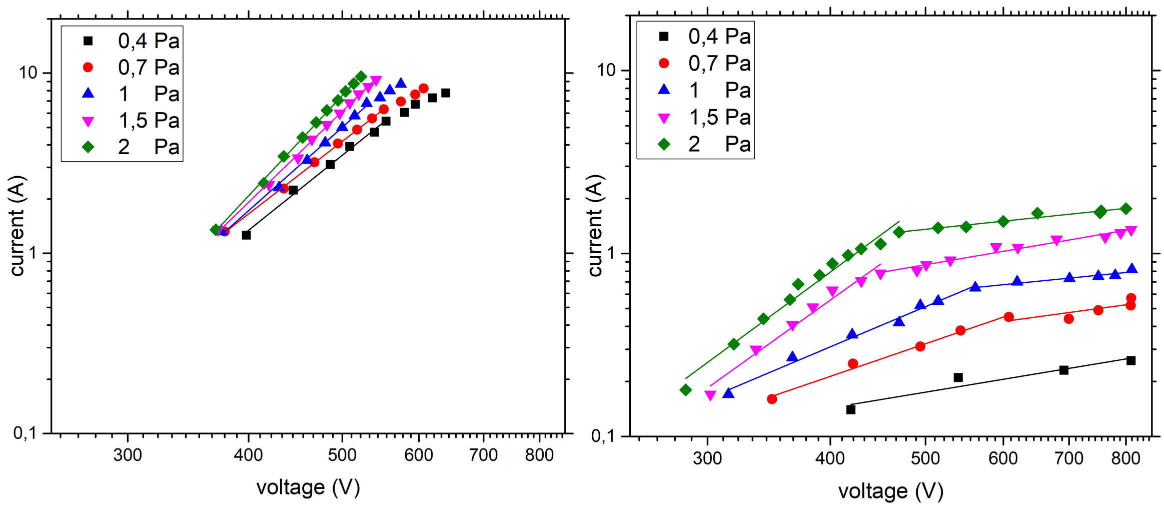

(a) (b)

Figure 4.21.: I-V characteristics of the configuration with 5 segments twisted by (*a*) 0 ° and (*b*) 30 °, recorded at different pressures.

It is clearly visible that the pressure dependence gets more pronounced with a higher degree of twist and a higher number of segments. While twisting the segments by 10 ° leads to a non-linearity of the I-V characteristics only at 0,4 Pa (Fig. 4.19a), starting from a twist of 20 ° all characteristics show a transition of slope. This causes the extinction of the discharge at lower powers compared to the non-twisted configurations. For I-V characteristics, which showed a transition in slope, linear fits were performed two times and two n values (n_1 and n_2) were obtained.

n, the exponent of Eq. 3.1, shows a decreasing tendency with additional segments and increasing degree of twist, compare Fig. 4.22. The decrease of n is especially pronounced at a twist of 30 °.

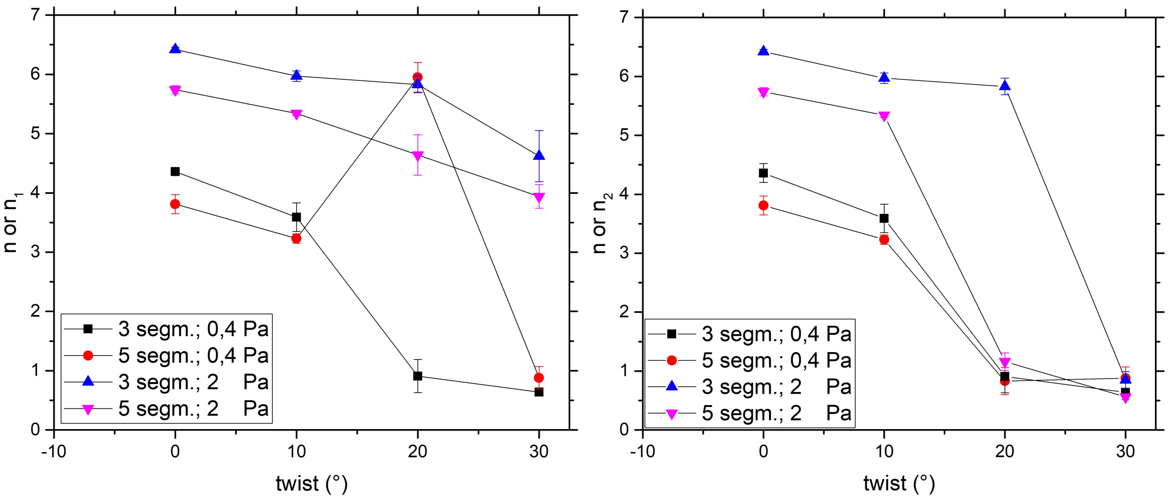

(a) (b)

Figure 4.22.: Exponent n over the twist for the configurations with 3 and 5 segments. Recorded for 0,4 Pa and 2 Pa. If the characteristics showed a transition of slope, in (*a*) n_1 and in (*b*) n_2 is shown.

The current-density of the plasma-tube increases with the pressure, because the current is higher at the same applied power. Fig. 4.23a shows the current-density as a function of the current, recorded at a power of 1000 W, each datapoint represents a different pressure value (0,4 Pa, 0,7 Pa, 1 Pa, 1,5 Pa and 2 Pa). As visible in Fig. 4.23b, the current-density of the plasma-tube does not stay constant with increasing twist of the segments, but decreases.

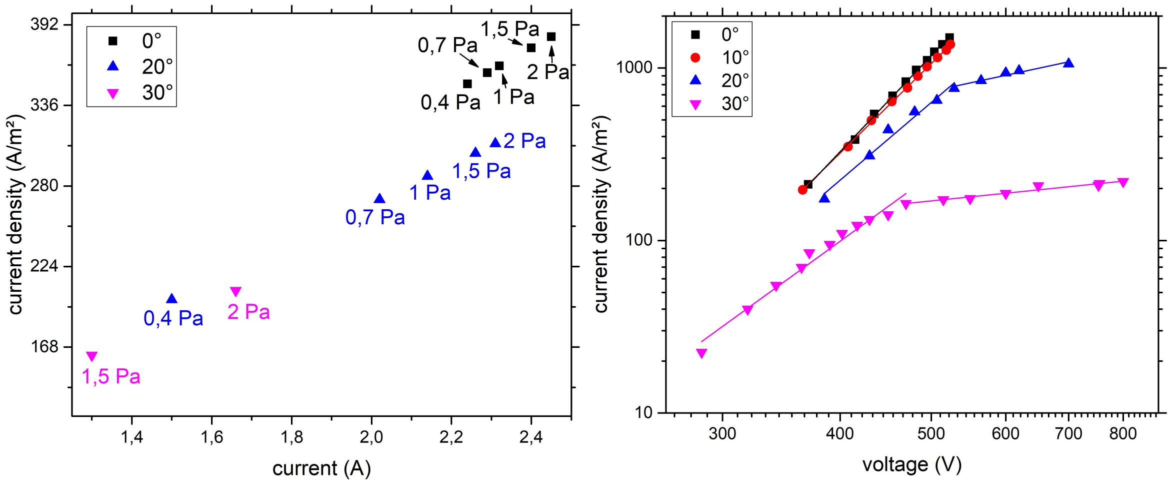

(a) (b)

Figure 4.23.: (*a*) Increasing current-density with pressure. Recorded at a power of 1000 W for a 5 segmented magnetron with at twist of the segments relative to each other of 0 °, 20 ° and 30 °. (*b*) Current-density decrease by the degree of twist of the magnetron with 5 segments recorded at 2 Pa.

4.4.2. Summary and Discussion

The I-V characteristics of all studied configurations, except the magnetron with 2 segments, showed a loss of linearity with decreasing pressure, a transition in slope was also observed with increasing twist. Starting with a twist of 20° the characteristics show two distinct regions, one with a higher and one with a lower slope (see Fig. 4.23b). Additionally, the discharge extinguished at lower power values with increasing twist.

By twisting the segments relative to each other, the magnetic field line distribution and therefore, the geometry and length of the plasma-tubes changes. As can be seen in Fig. 4.24, the plasma-tubes curve at the transition from one segment to another, while they are straight over the length of a segment.

Figure 4.24.: Plasma development for a 4 segment configuration twisted by 30 ° relatively to each other.

Because this is the only difference between the twisted and non-twisted configurations, it is assumed that due to the twisting, the trapping efficiency [14] of charge-carriers worsens. Only for the configuration with 2 segments n increased with the degree of twist for all pressures except 0,4 Pa where it also decreased. It can be seen in Fig. 4.14b that the plasma-tube developed much smoother for this system.

With the degree of twist, the length of the plasma-tube increases, nevertheless the current stays almost the same for the same applied power compared to the non-twisted configuration. Accordingly, twisted systems exhibit a lower current-density.

With a lower number of segments, the power-density increases because of the smaller target area which is sputtered off with the same power, therefore the current-density has to increase.

With increasing pressure, n increases because of the higher probability of collisions which results in a higher ionization-number and therefore higher number of electrons.

To conclude, a twist of the segments relative to each other yielded slightly higher n only for the configuration with 2 segments in comparison to the non-twisted configurations.

I-V characteristics of the configurations with 3, 4, and 5 segments showed approximate linearity for a twist up to 10 ° and a pressure down to 1 Pa. At lower pressures a transition of slope of the I-V characteristics occurred.

5. Magnetron for Coating Internal Surfaces of Tubes

The second part of this work consisted in converting the magnetic configuration described in section 4.1 to be suitable for the deposition of coatings on internal surfaces of narrow substrate-tubes. Before the construction of this magnetron, *FEMM* [19] simulations and Hall-measurements of its magnetic field configuration are presented. To test if internal coatings in narrow tubes with the presented magnetron are possible and to determine parameter-ranges, a proof of concept was implemented in an existing chamber. After successful performance tests (I-V characteristics, deposited film characterization), the final tube coating device was designed, see chapter 6.

5.1. Construction

Fig. 5.1 shows the design of the planned magnetron assembly. NdFeB block magnets (see section 3.2) were confined by two 3D-printed rings made from Polylactide (PLA). Concentrically assembled, these two 3D-printed rings form recesses in which the magnets were glued.

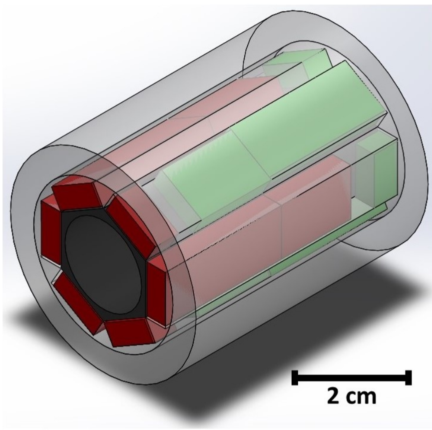

(a)

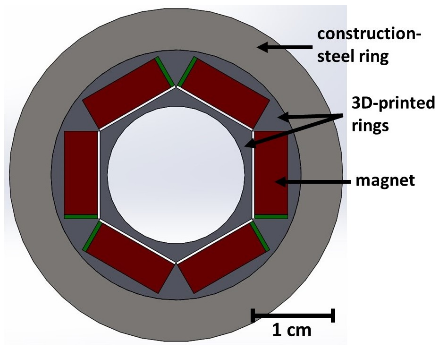

(b)

Figure 5.1.: Magnetron for internal coatings: (a) made transparent, so that the magnetic configuration is perceivable. The red and green blocks represent block-magnets with different orientation. (b) top view.

Additionally, the magnetron was inserted in a magnetizable construction steel ring, to confine the outer stray field (see section 5.2.2). The proposed configuration is basically a minimum version of the segmented magnetron with start- and end-pieces joint with zero twist and a non-magnetic core. Altogether the magnetron has a length of 50 mm and an inner diameter of 16 mm.

5.2. Magnetic Field Characterization

The formed magnetic field of the magnetron was studied by Hall-probe measurements (see section 3.2) and *FEMM* simulations, see section 3.3.

5.2.1. Hall-Probe Measurements

The Hall-probe measurements were conducted as explained in section 3.2. The central cylindrical hollow of the magnetron was measured in the mid-plane. As substrate, a 2 mm thick non-magnetic tube was assumed, the target is thought to be located in the center of the magnetron and is also non-magnetic. The result is shown in Fig. 5.2.

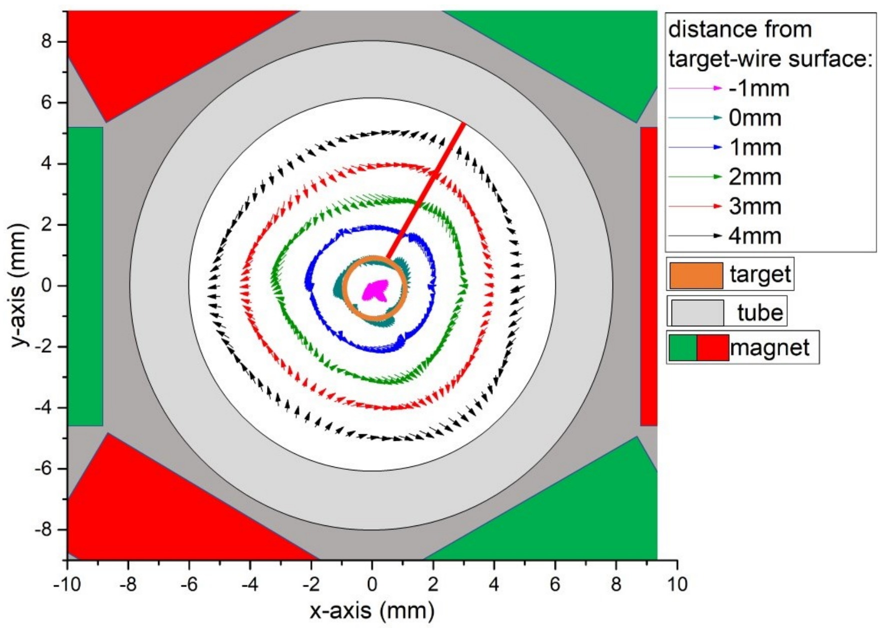

Figure 5.2.: Hall-probe measurement of the magnetic field formed inside a substrate-tube in the magnetron. The orange circle indicates the 2 mm diameter target-wire surface. Along the red line the decrease of the magnetic field strength was measured.

As for the modular cylindrical magnetron, see section 4.3.1, the magnetic field lines close between two neighboring magnets.

Fig. 5.3 shows the decrease of the magnetic field strength over the distance originating from the surface of the substrate-tube in the mid-plane of the magnetron and from the center of a magnet to the center where the target-wire was positioned in the final setup (red line in Fig. 5.2).

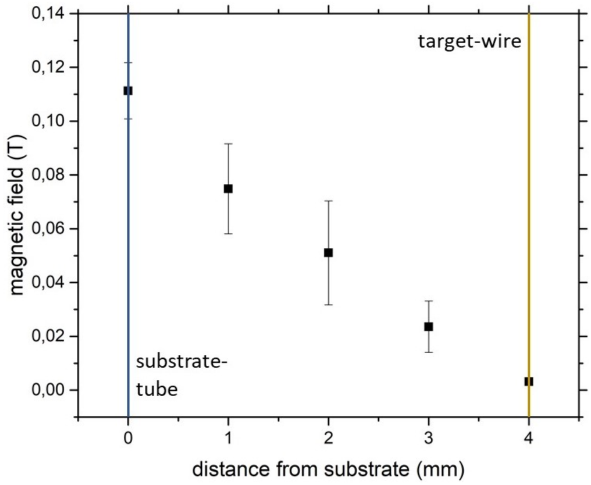

Figure 5.3.: Decrease of the magnetic field strength inside the substrate-tube in the magnetron from the surface of the tube (blue vertical line) to the target (golden vertical line). Statistic from 3 magnets.

At the location of the target-wire in the center of the magnetron the magnetic field strength is around 3,9% of its value at the inner surface of the substrate-tube.

5.2.2. Magnetic Field Simulations

Fig. 5.4 shows the *FEMM* simulation of the magnetron using a Cu target-wire 2 mm in diameter in its center with and without an outer construction steel ring.

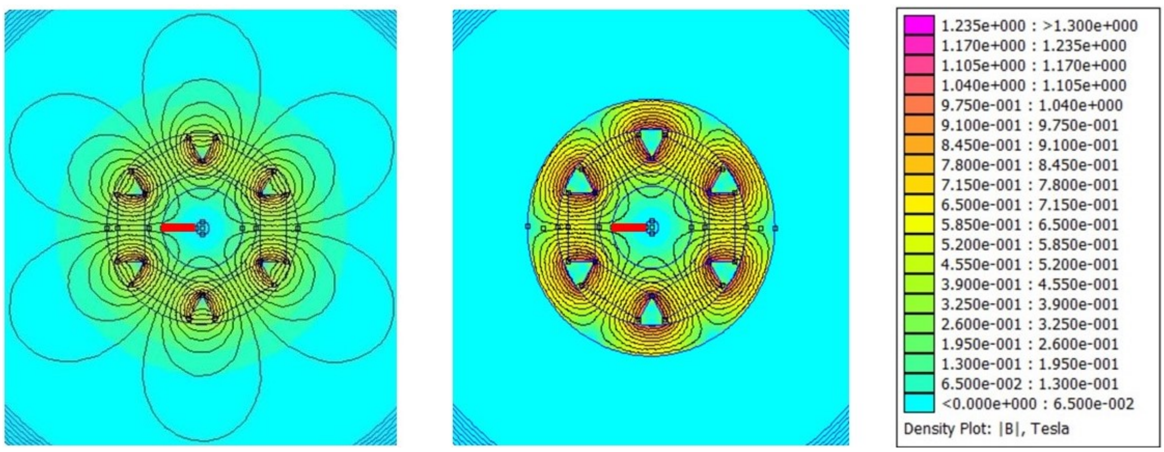

Figure 5.4.: *FEMM* simulation of the magnetron for internal coatings, left, without and, right, with outer confining construction steel ring.

It can be seen that the construction steel ring confines the magnetic field lines and increases the field strength towards the center of the magnetron, an effect which is highly desired to increase electron confinement.

Along the red lines, the decrease of the magnetic field strength is plotted in Fig. 5.5b. The results were compared to the same configuration but using a magnetizable Fe target-wire.

Hardly any impact of the magnetizable target-wire on the magnetic field lines was noticed, see Fig. 5.5b. Fig. 5.5a highlights the difference of the simulation with the coercivity value of 900000 A/m from the datasheet, see section 3.2, and the measurement. The simulation of the magenta line was obtained with a coercivity of 576000 A/m (corresponds to a remanence of 0,76 T), which was calculated from the difference in magnetic field strength of the simulation and the measurement, at the substrate-tube surface at the middle of a magnet, by assuming proportionality.

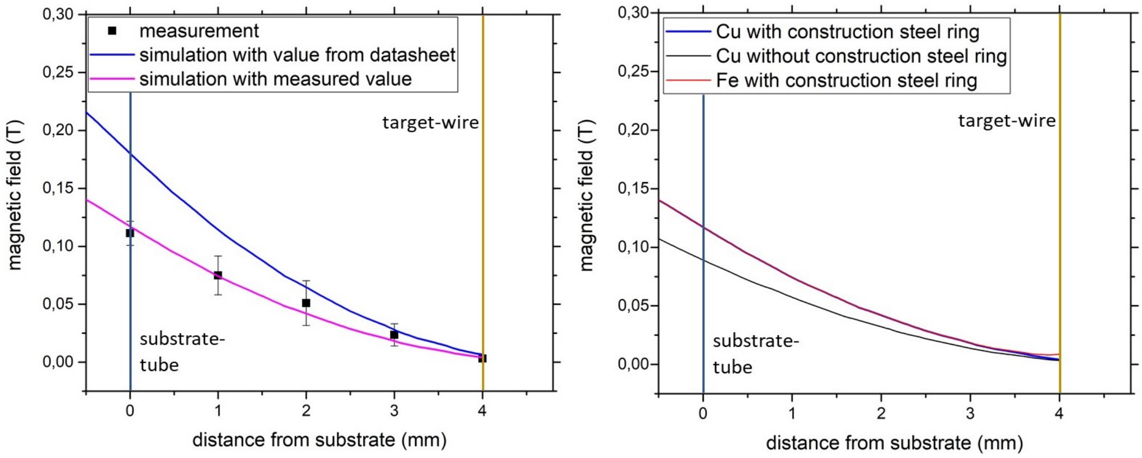

(a) (b)

Figure 5.5.: *FEMM* simulations of the decrease of the magnetic field strength over the distance from the inner surface of the substrate-tube (blue vertical line) to the target (golden vertical line) (a) simulations and measurement with construction steel ring and (b) simulations for a Cu and Fe target with different configuration and the measured coercivity value. The simulations for a Cu and Fe target-wire with construction steel ring are basically indistinguishable.

5.3. Proof of Concept

Fig. 5.6 shows the cross-section of the model of concept to test the deposition-performance of thin films in narrow (insulating) tubes (substrate) with the inverted magnetic configuration.

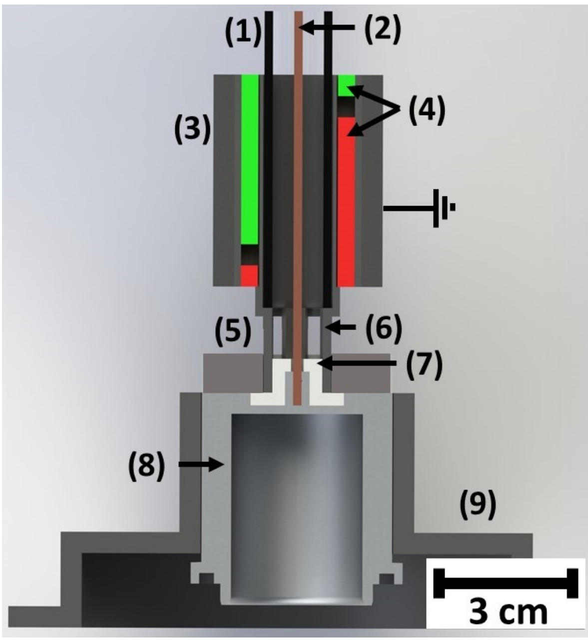

Figure 5.6.: Cross-section of the model of concept: (1) PMMA substrate-tube, (2) Cu target-wire, (3) magnetron with outer construction steel ring, grounded, (4) block magnets, (5) Teflon-element, (6) component to ensure AR-flow through the tube, (7) macor-element, (8) aluminum cylinder, (9) insulating top part.

It consists of an aluminum cylinder (8), whose diameter, bottom design and height fulfill functional needs to mount it in an existing vacuum chamber. The target-wire (2) has a diameter of 2 mm and is attached to this cylinder. A voltage on the target-wire is applied through the aluminum cylinder during the operation of the system. The acrylic glass (Polymethyl Methacrylate abbr. PMMA) substrate-tube (1), with an inner diameter of 12 mm and an outer diameter of 16 mm is arranged concentrically to the target and placed on a 3D printed component (6) which ensures Ar-flow through the tube. It is placed on a macor-element (7), which prevents electric contacts between the substrate and the target due to the deposition process on the tube because of its special geometry. The grounded construction steel ring of the magnetron (3) serves as anode during a plasma discharge. An insulating bottom part (9) prevents a plasma discharge between the aluminum cylinder and the system. This setup was mounted in the same vacuum-system as the modular magnetron, which was discussed in chapter 4. Unlike the modular magnetron, however, the present assembly did not rotate.

5.4. Plasma Development

The development of plasma is dependent on the electrode-distance and the working gas pressure according to Paschen's law. It extinguishes when the distance between the anode and the cathode is too small for the negative glow of the gas discharge to develop, see section 2.4.2. The space the negative glow needs to develop can be shortened by increasing the working gas pressure. Also, electrons can be trapped by $\vec{E}$- and $\vec{B}$- fields arranged in a way that the

$\vec{E} \times \vec{B}$-drift occurs. Furthermore, the electrons necessary for the ionization of the working gas can be directed to drift in a closed curve by the magnetic configuration. A ring current develops, and electrons are solely lost due to collision processes and due to other arising drifts, occurring for example due to curvatures and gradients in the $\vec{B}$-field. All these requirements are fulfilled in the case of the modular magnetron and are assumed to be valid also inside the inverted magnetron, if the field can penetrate the inner tube, which is guaranteed by using a non-magnetic core material. However, there are differences which will be discussed in the following.

Fig. 5.7 shows how the gas discharge develops inside the substrate-tube. What is seen as glowing is attributed to the negative glow, which is confined in the central target-area by the curved magnetic field lines. Furthermore, glowing lines are formed to the substrate making the magnetic field lines perceivable. Due to the difference in the cathode/anode/magnetron configuration from the case of the modular magnetron, namely that the cathode and magnetron have switched positions in their order, the magnetic field line curves are now curved in the direction of the electric field for the electrons (concave). This is in contrast to the case of the modular magnetron where the $\vec{B}$-field lines were curved in opposite direction of the $\vec{E}$-field (convex). With convex $\vec{B}$-field lines electrons are assumed to accumulate in these areas, whereas in the case of concave $\vec{B}$-field lines they can easily escape, due to instabilities, from these areas.

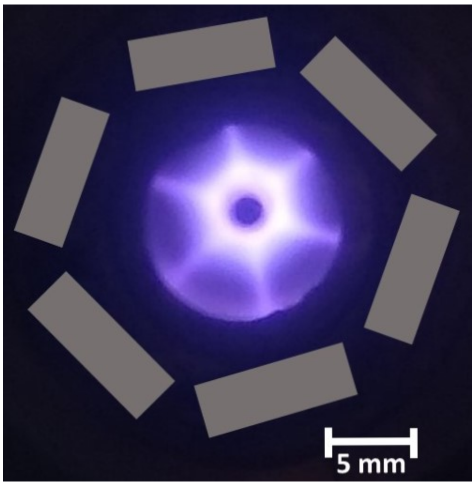

Figure 5.7.: Picture taken of the developed plasma discharge inside a PMMA substrate-tube during the operation of the model of concept. View from above. Gray rectangles symbolize magnets.

The star shaped lines indicate a charged particle flux to the substrate, see section 5.7. An unbalanced magnetron has formed, compare section 2.5.2.

5.4.1. Electric Field Distribution

The electric field line distribution of the model of concept was simulated using the program *FEMM*. This was done for an applied voltage on the target-wire of -800 V, see Fig. 5.8.

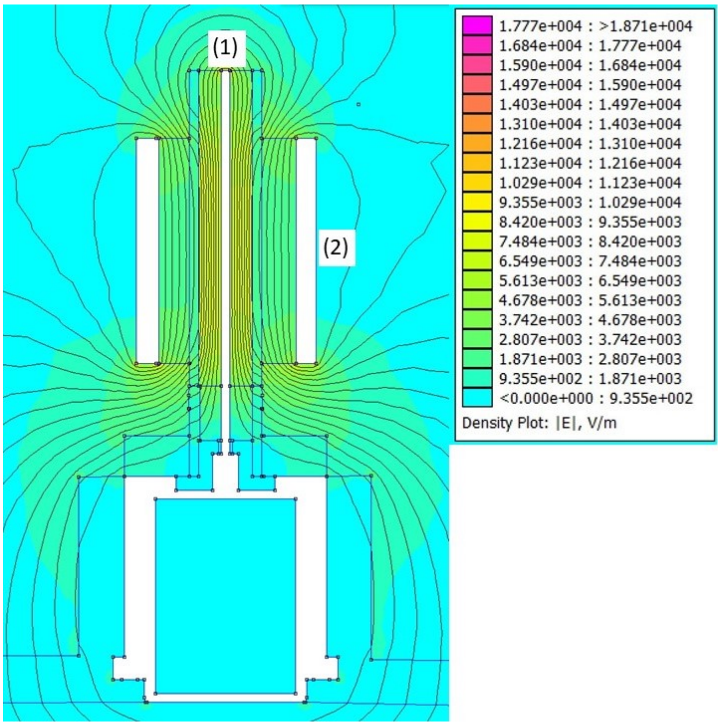

Figure 5.8.: Simulation (using *FEMM*) of the resulting electric field of the model of concept with the grounded construction steel ring of the magnetron (2) and the target (1). Lines correspond to equipotential surfaces, colors to field strength.

The E-field lines ($\perp$ to equipotential surfaces) develop radially to the target-wire (1) and the field strength is constant inside the tube. It is apparent that the grounded construction steel ring of the magnetron (2) primarily serves as anode and not the chamber walls.

5.5. Ignition Pressure

The ignition pressure describes the minimal pressure of the working gas necessary for a gas discharge to ignite at a specific applied power. In addition, the ignition pressure is dependent on system parameters, like the distance, configuration and material of cathode and anode, the electric and magnetic field line distribution, the working gas and applied power.

When determining the ignition pressure, a delay of the system response has to be taken into account. A 2 mm diameter Cu wire served as a target. The substrate was a 12 mm inner diameter PMMA tube, as described in section 5.3.

The charge carrier transport is now impeded due to insulating materials between the space of the anode and cathode. Therefore, the ignition pressure increased compared to the modular magnetron arrangement.

Fig. 5.9 shows the ignition pressure in dependence of the applied power.

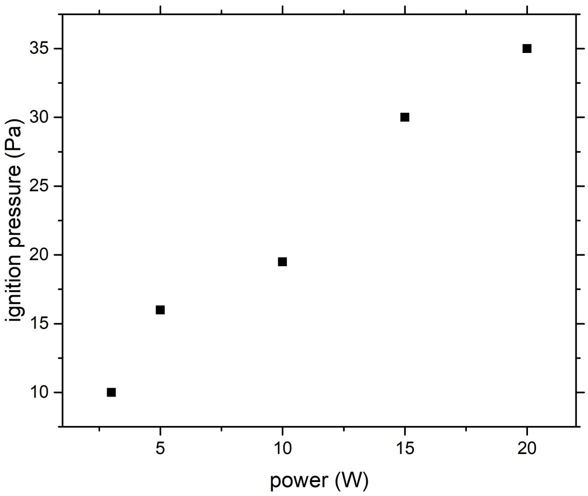

Figure 5.9.: Ignition pressure of the model of concept using a Cu-target, the grounded construction steel ring of the magnetron serves as anode.

After determining the working gas pressure range for the plasma ignition, an Ar-pressure of 30 Pa for the deposition experiments was chosen.

5.6. I-V Characteristics

I-V characteristics were recorded by tracking the current and voltage values, which were applied by the DC-source, after setting a power value. The DC-source with the indication *MDX 500* from the company *Advanced Energy* has a maximal power output of 500 W, a maximal voltage output of 1200 V and a maximal current output of 0,5 A. The Ar-pressure was set to 25 Pa, 30 Pa and 35 Pa and was measured with a Baratron with the specification *627BX01TDC1B* provided by the company *MKS Instruments*.

The obtained characteristics were fitted using Eq. 3.1 in section 3.1 and are shown in Fig. 5.10.

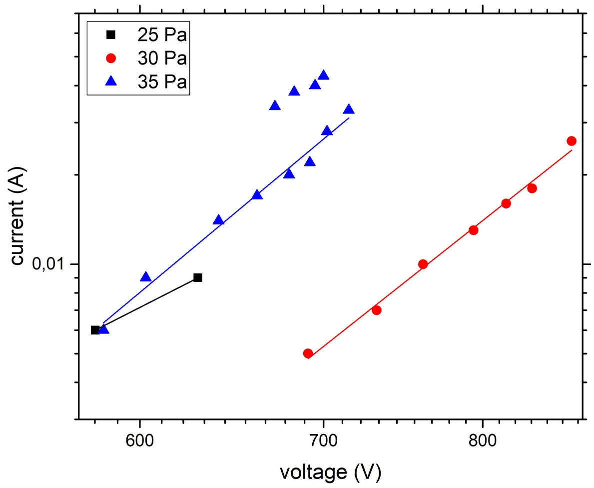

Figure 5.10.: I-V characteristics for a Cu target-wire at different Ar-pressures.

The resulting values for the slope n and V_0, which was obtained by extrapolation and assuming a minimal possible current of 0,001 A, are given in Table 5.1.

Table 5.1.: Values for n and V_0 obtained from the I-V characteristics shown in Fig.5.10.

	25 Pa	30 Pa	35 Pa
n	4,7	7,30 ± 0,26	7,71 ± 0,34
V_0	398 V	561 V	460 V

For 25 Pa the discharge ignited only for powers up to 5 W. For 35 Pa the I-V characteristics showed a jump at 25 W, which occurred in two more measurements. It is assumed, that this is caused by an instability of the plasma, which was, however, not yet optically observed.

5.7. Film Characterization and Evaluation

Thin films were deposited on polymer transparency films, see section 6.3.5, which covered the inner surface of the substrate-tubes. These films were removed again from the tube and were subsequently analyzed regarding their film-thickness distribution and deposition rate by applying the optical transmission method, see section 3.4.

Fig. 5.11 shows the film thickness distribution of a typical coated transparency film. An area with high deposition is found around the center axis of the sample and extends over a length of around 25 mm. This area is located between the deflecting magnets of the magnetron and can be associated with the 25 mm long block magnets.

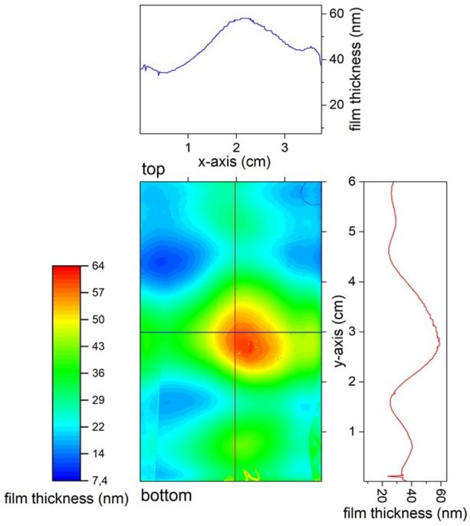

Figure 5.11.: Film thickness distribution of a Cu film deposited at 10 W and 30 Pa for 50 s. Top: upper end of tube; bottom: lower end of tube, towards Al-carrier.

The slightly higher deposition at the bottom and the top of the sample is assumed to originate from system-dependent secondary plasmas. The angle-dependent variations of the film-thickness along the circumference of the tube can be explained by a not entirely concentrically target-wire and/or a not perfectly fitting transparency film to the inner surface of the substrate-tube.

Starting from a power of 25 W a periodic pattern is visible on the deposited films, see Fig. 5.12. As emphasized by red lines in Fig. 5.12b, the pattern confines a meander-shaped surface area on the coated substrate, which is straight in the area of high deposition.

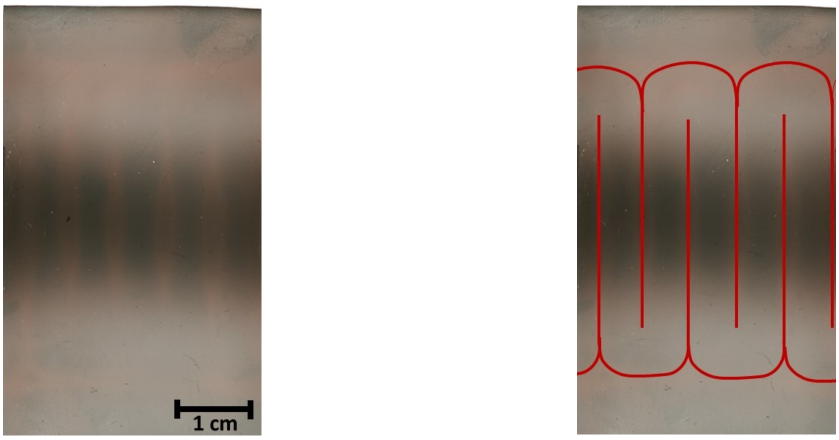

(a) (b)

Figure 5.12.: Cu-film deposited with 30 W, and 30 Pa for 5 s: (*a*) exposing a periodic pattern; (*b*) pattern is emphasized with red lines.

Evaluation of the film thickness yields a slightly higher thickness in the meander-shaped surface area rather than for the lines indicated in red in Fig. 5.12. A thickness line scan through the central part of the substrate is shown in Fig. 5.13.

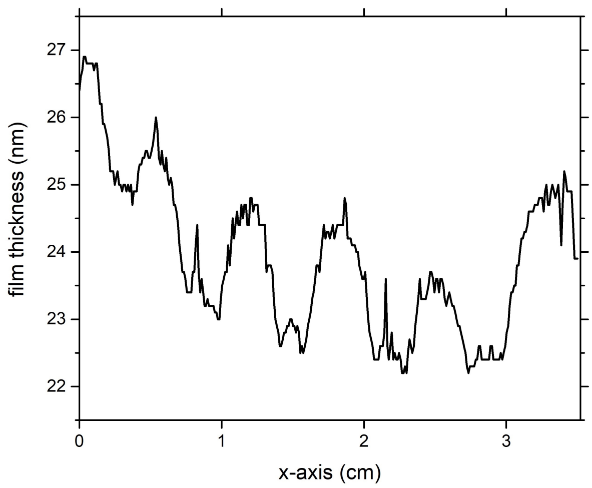

Figure 5.13.: Line profile of the film thickness distribution along the width of the deposited Cu film shown in Fig. 5.12.

These lines are believed to be the areas where the plasma touches the substrate, see Fig. 5.7. The meander-shaped surface between the red lines in Fig. 5.12b corresponds to the meander-pattern of the plasma-tube and is owned to the fact that the magnetron did not rotate. A rotating magnetron would yield a homogenous thickness around the tube.

In Fig. 5.14, the deposition rate of a Cu target-wire is plotted. For the evaluation of these datapoints only the area with maximal deposition (around 25 mm thickness) was considered.

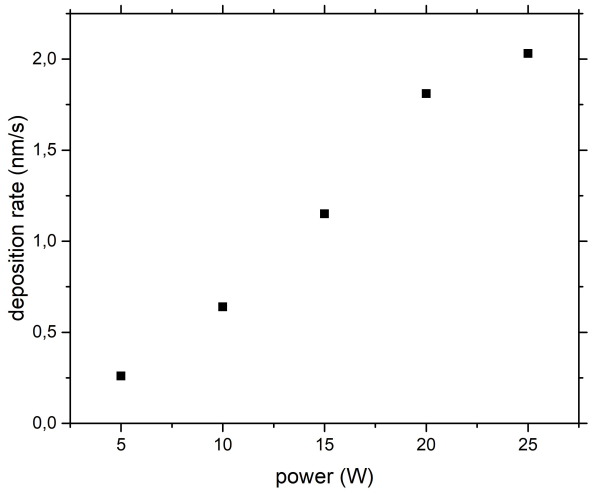

Figure 5.14.: Deposition rates for a Cu target-wire at different applied powers, recorded at an Ar-pressure of 30 Pa.

In Table 5.2 a summary of the results of the conducted deposition experiments is given.

Table 5.2.: Performed deposition experiments for every target/substrate configuration. The deposition rate was determined by taking only the area with maximal deposition (25 mm) into account.

target/substrate	pressure (Pa)	power (W)	time (s)	dep. film thickness (nm)	dep. rates (nm/s)
Cu/PMMA: 12 mm	30	5	80	21,05	0,26
Cu/PMMA: 12 mm	30	10	50	32,2	0,64
Cu/PMMA: 12 mm	30	15	30	34,5	1,15
Cu/PMMA: 12 mm	30	20	15	27,2	1,81
Cu/PMMA: 12 mm	30	25	10	20,3	2,03

5.8. Conclusion

The inverted magnetic configuration was found to be suitable to be used as a magnetron for the internal coating of narrow tubes. Although measurement and simulation showed a weak magnetic field strength at the area of the target and a strong decrease of its strength over the radius of the tube, plasma formed in the area of the target-wire, but was leaking along the magnetic field lines to the substrate-tubes. Thin Cu-films could successfully be deposited on the inside of PMMA tubes with 12 mm in diameter. These films showed an area with high deposition (25 mm) located around the mid-plane of the magnetron. This area is approximately limited by the distance between the two deflecting magnets on both ends in the magnetron. It is also believed that stronger angle-dependent variations in the film-thickness are a result of not perfectly fitting transparency films to the inner surface of the tube and/or a not perfectly concentrically mounted target-wire in relation to the substrate-tube.

Performance tests with the model of concept yielded linear I-V characteristics with a slope n in log-log-plots in the range of 4,7-7,7 at rather high minimal possible voltages of 398 V-561 V, depending on the Ar-pressure. It was found that the ignition pressure for a gas discharge is in the 10 Pa range.

6. DC Magnetron Sputtering Device for the Internal Coating of Narrow Tubes

After showing that it is possible to coat the inside of tubes with an inner diameter of 12 mm with the inverted magnetic configuration, see section 5.3, a device for the internal coatings of narrow tubes was designed. In this chapter, the components, the construction and the achievable base-pressure of this device will be discussed, before turning to the results of performance tests. For these, different target- and substrate-materials were used and I-V characteristics were recorded, also, the deposited thin films were studied. Finally, the results of temperature measurements on the substrate and target are shown.

Devices for coating the internal surface of narrow tubes using the sputter-technique are also found in the literature, see e.g. [23–26]. All of these assemblies were installed inside vacuum chambers. Also, when magnetron sputtering was utilized, static magnetic systems were used. In [26] the plasma discharge could be moved by altering the magnetic field of electromagnets. When insulating tubes were coated, the anode was mounted to the ends of the substrate-tube.

6.1. Design, Assembly and Operating Principle

Design: The design of the device for the internal coating of narrow tubes is shown in Fig. 6.1.

Essentially, it consists of a tube (4) connecting a left part and a right part by tube compression fittings (3) for tubes with an outer diameter of 16 mm. This tube serves as substrate and simultaneously as part of the vacuum chamber. The device has a total length of around 90 cm, with a substrate-tube length of around 30 cm. The choice of the substrate-length was arbitrary. The magnetron (6), which was discussed in chapter 5, is situated on the outside around the tube. The right part of the device is mounted on a rail (8) which allows its forwards and backwards movement in the non-tautly mounted state of the device. It is connected to the pumping system (*Alcatel 5080* turbomolecular pump and *Adixen drytel 1025*) and a Penning gauge (*Alcatel CF2P*) through a flexible corrugated hose (see (15) in Fig. 6.1b).

To the left part a Penning/Pirani vacuum gauge (12) (*Adixen Acc 2009*), an Ar-inlet (14) (needle valve *Alcatel Type 6819*) and an air-inlet (13) are connected, see Fig. 6.1b. Part of this side is also a bellow (1), whose function is explained below.

A wire (5 in Fig. 6.1a), which serves as target is tautly mounted concentrically over the entire length of the device. The wire is fixed using plug-on connectors on both sides, which are connected to coaxial feedthroughs (9), see below. Atmosphere-sided, the right feedthrough is connected to a DC-source with the indication *MDX 500* from the company *Advanced Energy* with a maximal power output of 500 W, a maximal voltage output of 1200 V and maximal current output of 0,5 A. The left-sided coaxial feedthrough remains free atmosphere-sided and is secured with an insulating attachment.

A list of all components is given in the Appendix A.4.

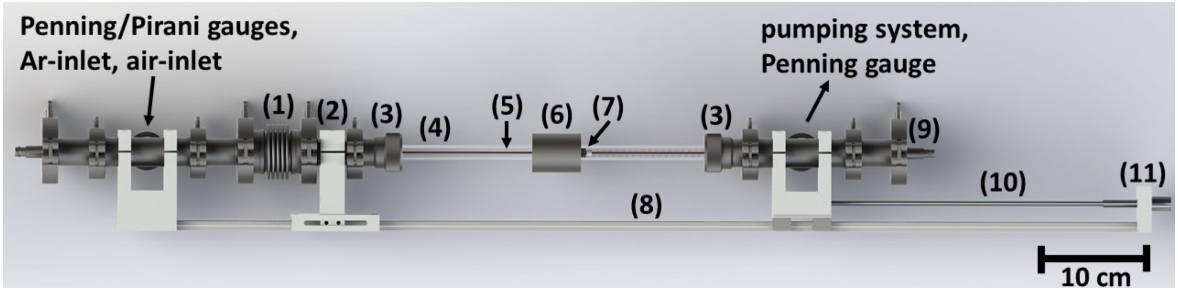

(a)

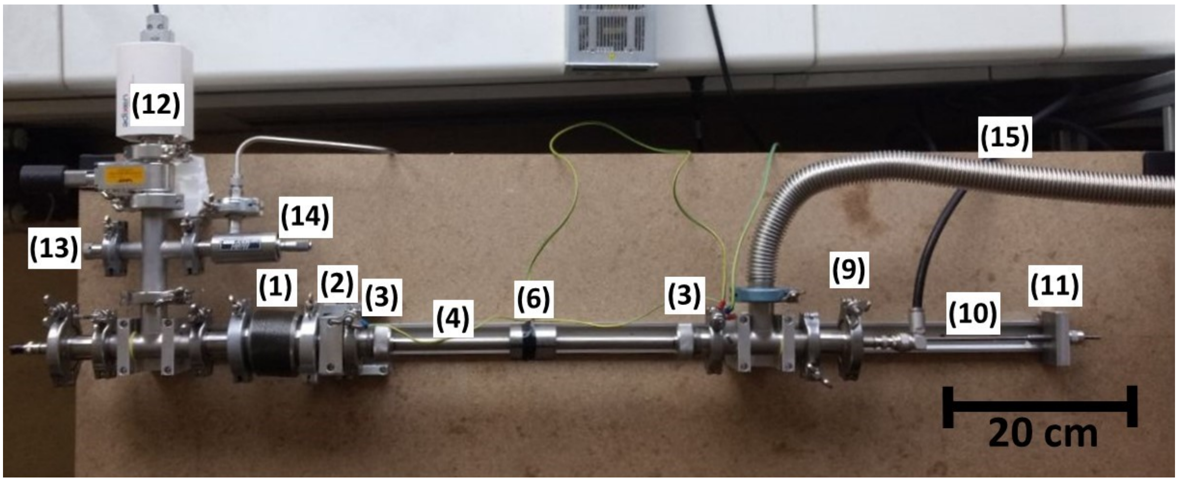

(b)

Figure 6.1.: (a) Rendering and (b) real-life image of the device for the internal coating of tubes: (1) bellow, (2) construction to contract or expand the bellow, (3) tube compression fitting, (4) substrate tube, (5) target-wire, (6) magnetron, (7) anode for insulating substrate-tubes, (8) rail, (9) coaxial feedthrough, (10) rod, (11) mounted thread, (12) Penning/Pirani gauge (*Adixen, Acc 2009*), (13) air-inlet, (14) Ar-inlet, (15) flexible corrugated hose. Equal numbers in (a) and (b) are designated equal parts.

Mounting the target-wire: To tautly mount the target-wire, first, one end is attached to the coaxial feedthrough with a plug-on connector (marked red in Fig. 6.2).

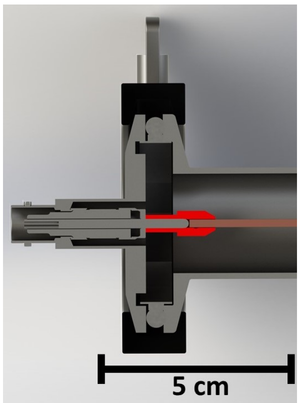

Figure 6.2.: Rendering of the cross section of the coaxial feedthrough, showing how the target-wire is connected by the plug-on connector (marked red).

The wire is fed through the entire length of the device while the bellow is being contracted by a special construction ((2) in Fig. 6.1a). The other end of the wire can then be mounted on the second coaxial feedthrough. By letting the bellow expand again, the coaxial feedthroughs are pushed to the end-faces of the apparatus which close the device. The target-wire is finally fixed and set under tension by pulling the right part of the device using a threaded rod (10), which is connected to the system on the right (11), see Fig. 6.1a. Due to this construction, the right part of the apparatus can be moved in small defined steps. Additionally, insulating centering pieces are positioning the wire concentrically inside the tube, see Fig. 6.3.

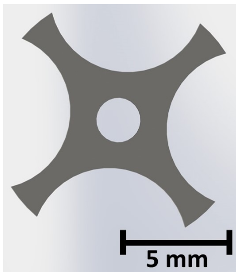

Figure 6.3.: Rendering of a centering piece, which was used to position the target-wire concentrically inside the tube.

Operating Mode: As visible in Fig. 6.1a, the magnetron which was discussed in chapter 5, is situated on the outside around the tube. During the deposition process, it can be rotated and shifted arbitrarily along the length of the tube, because it is easily accessible from the outside. Plasma first develops in the area inside the tube which is located underneath the magnetron, see Fig. 6.4, in dependence of the applied pressure and power.

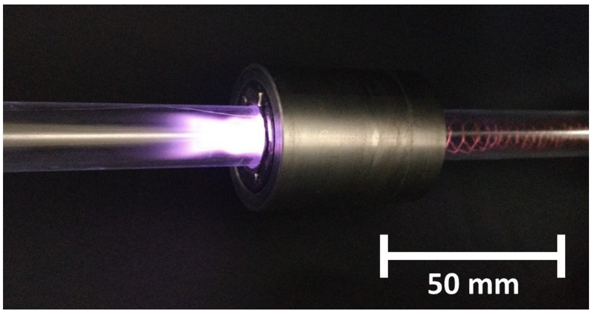

Figure 6.4.: Image of a plasma discharge, which first develops inside the tube underneath the magnetron.

6.2. Base Pressure and Effective Pumping Speed

Due to the design of the device, only tube-shaped areas are pumped, which results in a relatively low conductance and a pressure gradient developing over the length of the device.

For a PMMA substrate-tube, see section 6.3.4, a base-pressure in the mid 10^{-2} Pa range could be reached, whereas for a stainless steel substrate-tube (section 6.3.4) a base-pressure down to the lower 10^{-3} Pa range was accomplished.

In the following, the resulting pressure gradient is discussed. The pressure was measured at two different points: at the very left of the device ((12) in Fig. 6.1b) and in direct proximity of the turbomolecular pump. These two pressure gauges are presumably mounted at areas with the highest and lowest pressure.

Close to the turbomolecular pump pressures down to the 10^{-5} Pa regime were reached. This results in a pressure-gradient ∇p between the two measuring points of $\Delta p = \frac{p_{(1)} - p_{(2)}}{L} \approx 10^{-2}$ Pa.

The following considerations and equations are taken from [2]:

In general, pumps are characterized by their pumping speed S (S is 80 l/s for nitrogen for the *Alcatel 5080*). Their actual pumping speed (effective pumping speed S_{eff}) is dependent on the geometry of the vacuum-device, more precisely on the conductance of the vacuum components. The conductance C depends on S_{eff} as follows:

$$\frac{1}{S_{eff}} = \frac{1}{S} + \frac{1}{C} \tag{6.1}$$

On the basis of molecular flow conditions, the following assumptions can be made about C of a long tube: $C_{longtube,mol}$ can be composed of the conductance through an aperture $C_{aperture,mol}$ and the transmission probability $P_{tube,mol}$:

$$C_{tube,mol} = C_{aperture,mol} + P_{tube,mol} \tag{6.2}$$

$C_{aperture,mol}$ is given by:

$$C_{aperture,mol} = A\frac{\bar{c}}{4} \tag{6.3}$$

where A is the cross section of the pumped vessel and $\bar{c}$ the average particle velocity. For a molecular air flow at 293 K, $C_{aperture,mol}$ is given in [2] for a DN16 flange as 23,3 l/s, for a DN25 flange $C_{aperture,mol} = 52,4$ l/s and for an DN40 flange $C_{aperture,mol} = 153$ l/s.

The exact expression for $P_{tube,mol}$ for a long tube is:

$$P_{tube,mol} = \frac{1}{4lA}\int_s ds \int_{-\pi/2}^{\pi/2} d\theta\, b(\theta)^2 \cos\theta \tag{6.4}$$

where l is the length of the tube, ds describes the integration over the circumference of the tube. $b(\theta)$ is the average path length of a particle between two collisions with the wall and θ is the angle between ds and $b(\theta)$.

Analytically this integral is difficult to solve, but to estimate the order of magnitude of $P_{tube,mol}$, a simplification can be made when setting $b(\theta)$ equal to the diameter of the tube d. This yields the following expression:

$$P_{tube,mol} \approx 2dl \tag{6.5}$$

With these equations, an approximation for $C_{tube,mol} = 1,149$ l/s can be made. Using this result, the effective pumping speed can be calculated to be $S_{eff} = 1,132$ l/s

From this calculation one can conclude, that S_{eff} essentially only depends on $C_{tube,mol}$ and not on the pumping speed S of the turbomolecular pump.

6.3. Targets and Substrates

In this section, the specifications of the used targets and substrates are given. For EDX spectra, samples were prepared in the following way: A cut surface of the material was cleaned with acetone and subsequently rinsed with distilled water.

6.3.1. Cu-Target

Copper was chosen as a target material because of its easy availability and its semi-precious metal properties. Cu has a sputter-yield of 1,89 utilizing Ar-projectiles with 500 eV [7].

A Kapton insulated wire, 2 mm in diameter was utilized as a Cu target. The Kapton insulation was either removed over the entire length of the tube or solely over the length of 50 mm exactly in the middle of the tube. This length corresponds to the length of the magnetron.

Fig. 6.5 shows the measured EDX spectrum of this target, as well as the quantification of the spectrum.

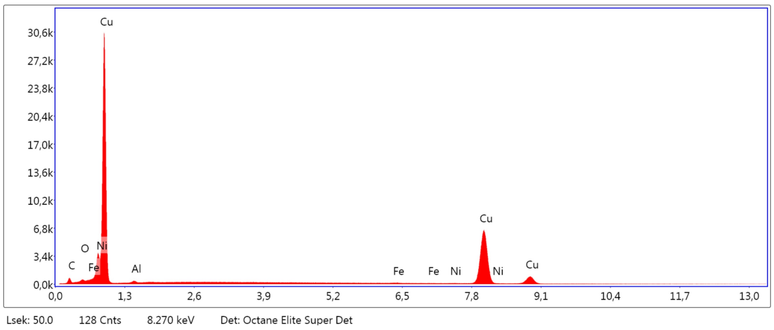

Cu:	75,9 at%
C:	19,4 at%
O:	3,1 at%
Al:	1,3 at%
Fe:	0,2 at%
Ni:	0,1 at%

Figure 6.5.: EDX spectrum of the cut surface of the Cu target-wire.

6.3.2. Fe-Target

Iron was chosen as target material because of its magnetic properties and their possible effect on the performance of the device due to influences on the magnetron. A magnetostatics simulation with this target-magnetron configuration can be seen in section 5.2.2. Fe has a sputter yield of 1,11 utilizing Ar-projectiles with 500 eV [7].

The Fe target had a diameter of 1 mm and was insulated with Teflon tubes over the areas not inside the substrate-tube. The wire has the specification EN 440 G 3 Si 1 and an EDX spectrum is shown in Fig. 6.6.

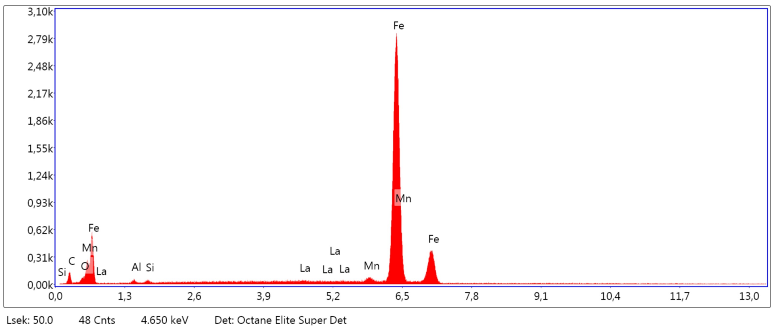

Fe:	79,5 at%
C:	16,5 at%
O:	1,7 at%
Mn:	0,9 at%
Al:	0,8 at%
Si:	0,5 at%
La:	0,1 at%

Figure 6.6.: EDX spectrum of the cut surface of the Fe target-wire.

6.3.3. Al-Target

All measurements/experiments with the Al-target were performed by Sandro Dal Cin in the course of a project work.

Aluminum was chosen as target material, because of its reactiveness on atmosphere. The influences of this effect on the performance during sputtering processes were studied. Al has a sputter yield of 0,98 utilizing Ar-projectiles with 500 eV [7].

A 2 mm diameter Al wire-target, which was insulated with Teflon tubes over the length over the areas not covered by the substrate-tube, was used.

Fig. 6.7 shows the EDX spectrum of Al.

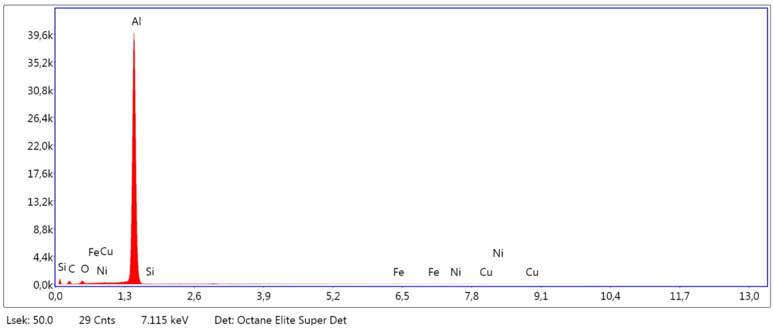

Al:	72,1 at%
C:	21,7 at%
O:	5,5 at%
Si:	0,3 at%
Fe:	0,1 at%
Ni:	0,1 at%
Cu:	0,1 at%

Figure 6.7.: EDX spectrum of the cut surface of the Al target-wire.

The strong presence of C and O in all investigated target materials is believed to result from surface contaminations e.g. due to the cleaning process and due to oxidations effects, whereas the other elements in the 1,2 at% - 0,1 at% range are assumed to be contaminations which occurred during the sample preparation or trace elements in the sample.

6.3.4. Substrate Tubes

The performance of the final setup was tested with insulating and conducting substrate-tubes. Acrylic glass (Polymethyl methacrylate abbr. PMMA, obtained from the company *Transparent Design Handels GesmbH* [27], produced by the extrusion-technique (XT)) was used as insulating substrate-tube. Stainless steel was used as a conducting substrate-tube (with the specification Niro 1.4301 obtained from the company *Fixmetall*). Both tubes had an outer diameter of 16 mm and an inner diameter of 12 mm.

Furthermore, to test even smaller diameters, experiments on PMMA tubes with reduced inner diameter were performed. Therefore, a PMMA tube with an inner diameter of 8 mm and an outer diameter of 12 mm and a length of 60 mm was inserted in a PMMA tube with an inner diameter of 12 mm, see Fig. 6.8.

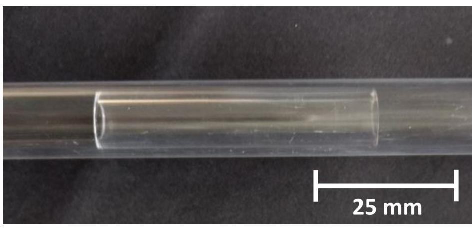

Figure 6.8.: Image of a PMMA tube with an inner diameter of 8 mm and an outer diameter of 12 mm in a PMMA tube with an inner diameter of 12 mm and an outer diameter of 16 mm.

6.3.5. Transparency Film Substrate

To be able to evaluate the deposited films with the optical transmission method (see section 3.4), planar substrates are required. For this reason, transparency films from the company *Q-Connect* with the indication *Black/ White Laser Transparency Film* with the length of the magnetron (50 mm) and the width of the inner diameter of the tube (37,6 mm for a 12 mm inner diameter and 25,1 mm for a 8 mm inner diameter) and a thickness of 0,1 mm were used. These films sheathed the PMMA and stainless steel tubes from the inside.

6.4. Carry-along Anode

Due to the insulating properties of PMMA, this substrate-tube cannot serve as anode simultaneously. For this reason, a special anode was designed, which had to fulfill the following requirements:

- Freely movable along with the magnetron to not lose the possibility of deposition only in distinct areas.
- No mechanical contact with the substrate prevent damage to the already deposited thin film while moving the anode.
- Sufficient gas flow through the anode to pump the device and also to maintain a discharge by sufficient Ar-flow.
- Appropriate electric field line formation relative to the magnetic field lines to ensure plasma ignition.
- Sufficient anode surface to form only a small space-charge region, see section 2.4.3.

Fig. 6.9 shows the designed anode.

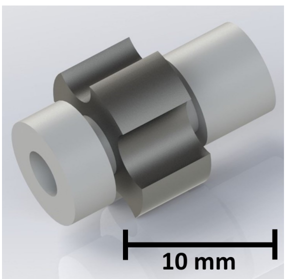

(a)

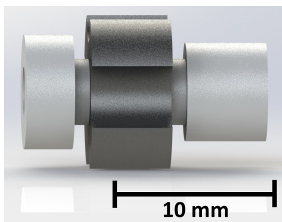

(b)

Figure 6.9.: Rendering of the designed anode for insulating substrate-tubes. The gray part corresponds to construction steel (ST37) and the white parts to Macor.

The anode ((3) in Fig. 6.10) is mounted directly on the target-wire ((1) in Fig. 6.10) which is on high voltage during the deposition process. Therefore, the anode consists of insulating elements, which separate the conductive part from the target. For the choice of the insulating material, high temperatures on the target during the deposition process (see section 6.8) had to be considered. Therefore, Macor, which is a ceramic material and therefore withstands operating temperatures up to 800 °C [28], was used. The conductive part of the anode consists of construction steel (ST37 obtained from *Fixmetall*), which is magnetizable. Therefore, the whole anode (3) gets trapped in the magnetic field lines of the deflecting magnets (6) in the magnetron (2), see Fig. 6.10.

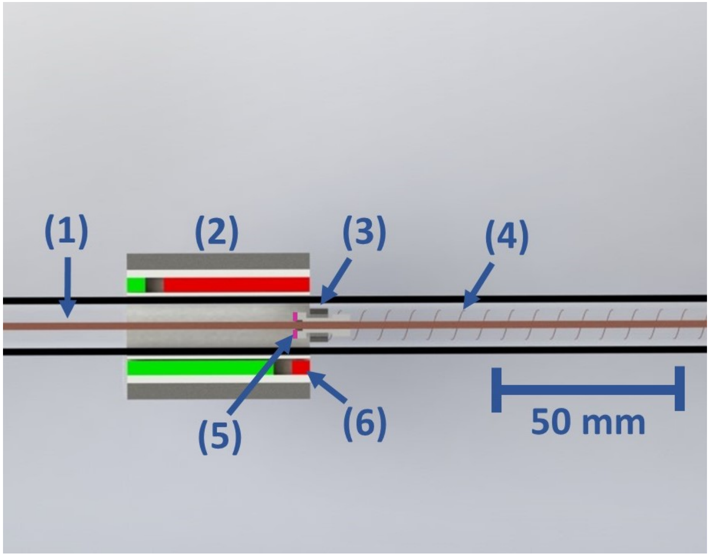

Figure 6.10.: Rendering of the cross section of the tube and the magnetron. (1) target-wire, (2) magnetron, (3) anode, (4) soft Cu spring, (5) violet marked area, (6) deflecting magnet.

This ensures that the anode is always located on the lateral end of the magnetron and can be carried along. The anode freely moves along the target wire and is constructed not to touch the inner surface of the substrate tube, thus preventing damaging of the already deposited thin film.

As the anode is now positioned directly on the target, a short circuit due to the deposition of the insulating macor element is possible, see violet marked area (5) in Fig. 6.10. This can be avoided using the following approach:

A macor-shield is located in front of the conductive construction-steel element, a gap of 1 mm width and 2 mm depth in between them prevents the development of a conductive connection due to geometrical reasons. A macor-shield is located on the backside of the anode as well. It serves the purpose to hinder possible discharges on this side of the anode.

The special shape of the construction-steel element enables a gas-flow through the anode. Also, the surface of the anode gets enlarged. A soft spring (4) made of Kapton insulated Cu, which is connected to the construction-steel element of the anode and the stainless steel elements of the device, puts the anode on the same potential as the rest of the chamber which is grounded.

6.4.1. Plasma Formation

It is assumed that the plasma formation is very similar to the case of the model of concept, see section 5.4, because of the identical magnetic field line distribution. A difference now exists in the formed electric field.

Stainless Steel-Tube: The electric field line distribution of a *FEMM* [19] simulation for an applied voltage of -800 V on the target-wire for the arrangement with a stainless steel substrate-tube is shown in Fig. 6.11.

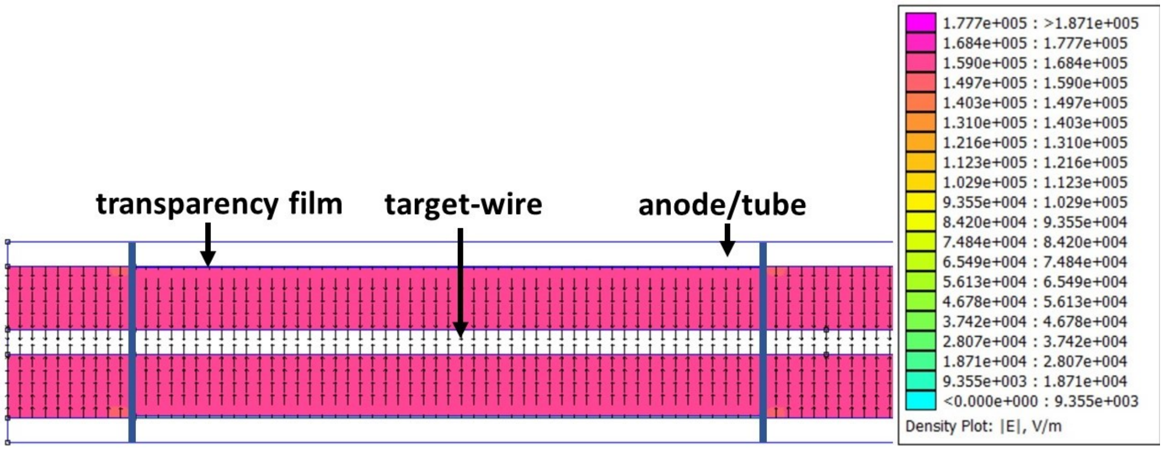

Figure 6.11.: Simulated electric field lines (with *FEMM*) of a configuration with the stainless steel tube, which now serves as anode. Blue lines mark the area covered by the magnetron. Within this region also a thin insulating layer is attached to the inner surface of the tube, to mimic the transparency film for film-thickness determination.

Due to the conducting properties of stainless steel, the tube simultaneously serves as substrate and anode. The field lines develop radially from the anode to the concentrical target-wire (cathode). The field strength is constant over the entire length of the tube.

Insulating 0,1 mm thick transparency films were attached to the inner surface of the tubes in order to analyze the deposited film later on, see section 6.3.5. This transparency film was taken into account in the simulation for the E-field line distribution. As shown in Fig. 6.11 hardly any influence due to this film is perceivable, just a charged particle transport through the transparency film is now not possible anymore.

12 mm PMMA-Tube: Fig. 6.12 shows the simulated (using *FEMM*) electric field lines distribution for the setup including the carry-along anode. The contour lines indicate the equipotential lines. The electric field lines now show a curvature. The E-field strongly varies in strength over the length of the magnetron which is marked by red lines.

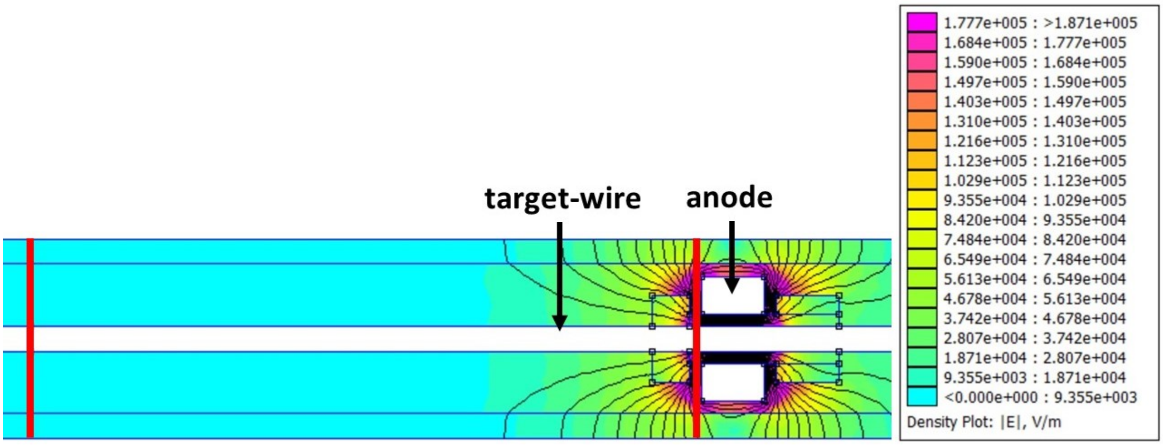

Figure 6.12.: Simulated electric field lines (with *FEMM*) of a configuration with the 12 mm PMMA tube. Red lines mark the area covered by the magnetron.

The superposition of the electric and magnetic field is now complex. A perpendicular electric field component relative to the magnetic field exists now not only at the vertex of the magnetic field lines. Because of the not purely perpendicular E-field lines to the target, the E-field component which is perpendicular to the vertexes of the B-field curves is now weaker. This is assumed to affect the efficiency of the intentionally implemented $\vec{E} \times \vec{B}$ - drift and therefore the performance of the magnetron.

8 mm PMMA-Tube: Fig. 6.13 shows the simulated (using *FEMM*) E-field lines distribution for the configuration with the 8 mm PMMA tube including the carry-along anode. The contour lines indicate the equipotential lines. Because the same anode is used as for the PMMA tube with 12 mm in diameter, the distribution looks almost the same. The difference is, that the E-field strength shows a slower decrease over the length of the tube.

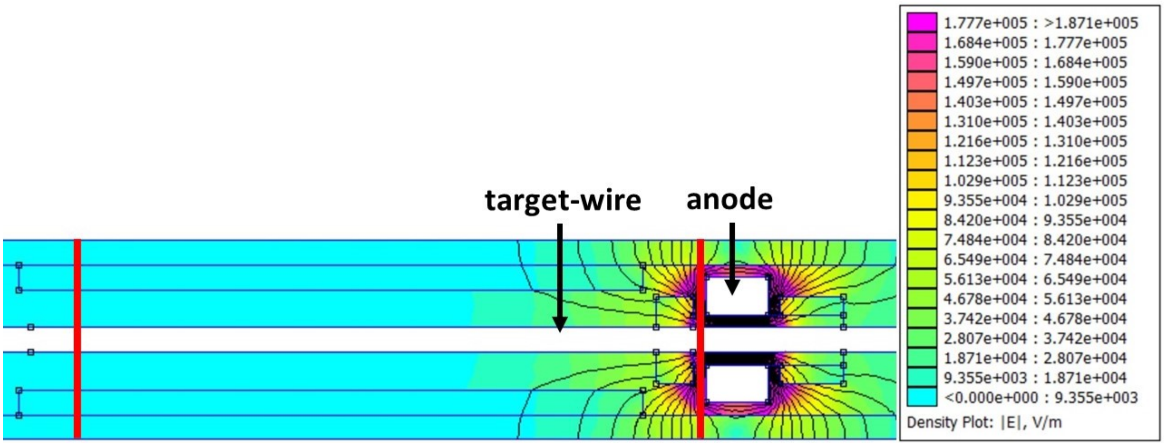

Figure 6.13.: Simulated electric field lines (with *FEMM*) of a configuration with the 8 mm PMMA tube. Red lines mark the area covered by the magnetron.

6.5. Ignition Pressure

Ignition pressures were determined for all target-substrate-configurations by applying a power and slowly increasing the pressure until the discharge ignites, see Tables 6.1, 6.2 and 6.3.

Table 6.1.: Ignition pressures for the Cu target and different substrate tubes for different power values. Statistic for PMMA from 4 measurements, for 8 mm PMMA and stainless steel from 2 measurements.

	ignition pressure (Pa)		
power (W)	PMMA	8mm PMMA	stainless steel
5	26,5 ± 2,38	34 ± 2,82	15 ± 1,41
10	27 ± 2,16	37 ± 2,82	17
15	28 ± 2,44	39,5 ± 3,53	19 ± 1,41
20	29 ± 2,44	41 ± 2,82	21 ± 1,41
25	30 ± 2,44		23
30	30,5 ± 2,88		24

Table 6.2.: Ignition pressures for the Fe target and different substrate tubes for different power values. Statistic for 8 mm PMMA and stainless steel from 3 measurements.

	ignition pressure (Pa)		
power (W)	PMMA	8mm PMMA	stainless steel
3	19	31,66 ± 1,52	
5	20	32 ± 2,64	15,6 ± 0,57
8	21	33,3 ± 1,52	18
10	23	34,3 ± 1,52	18,3 ± 0,57
13	25	36,6 ± 1,15	21 ± 2,64
15	28	38,6 ± 1,15	23,6 ± 0,57

Table 6.3.: Ignition pressures for the Al target and different substrate tubes for different power values. Statistic for 8 mmm PMMA from 3 measurements. Measurements performed by Sandro Dal Cin.

	ignition pressure (Pa)		
power (W)	PMMA	8mm PMMA	stainless steel
5	21	26,33 $\pm$ 1,52	16
10	19	26 $\pm$ 1	17
15	26	32 $\pm$ 2,64	19
20	22	31 $\pm$ 2,64	20
25	27	35 $\pm$ 1	20

Based on these measurements, the Ar-pressure for the deposition experiments for PMMA 12 mm in diameter and stainless steel tubes was set to 30 Pa, for PMMA-tubes 8 mm in diameter was set to 35 Pa.

6.6. I-V Characteristics

I-V characteristics were recorded for all target-substrate configurations by reading off the current and voltage values, applied by the DC-source, for certain power values. The set Ar-pressures were 25 Pa, 30 Pa and 35 Pa for the 12 mm diameter tubes and 32 Pa, 35 Pa and 40 Pa for the 8 mm PMMA tube.

The characteristics showed a time dependent voltage-increase depending on the applied power. To achieve reproducibility, all voltage and current values were recorded after a run-in period of 10 s. It was assumed that the time dependent behavior originated in increasing target-temperature during the sputter process, therefore the system was left to cool down after every recorded power value for approximately 3 min.

The time dependence of the voltage for the target/substrate configuration Cu/stainless steel for different applied powers shown in Fig. 6.14.

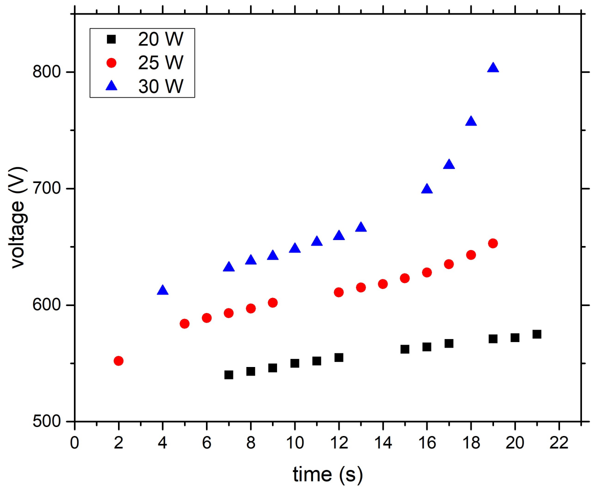

Figure 6.14.: Time dependent voltage for the target/substrate configuration Cu/stainless steel for different applied powers.

As can be seen from Fig. 6.14, after approximately 15 s the voltage drastically increases for powers above 20 W. At the 10 s mark, however, a voltage increase by approximately 10 V - 50 V took place, i.e. about 3-10% of the initial value.

The obtained I-V characteristics were fitted using Eq. 3.1 as described in section 3.1. To obtain V_0, a minimum current of 0,001 A was assumed. However, many characteristics showed no sufficient linearity for reasonable results of V_0. All values for n and V_0 are given in Appendix A.2.

I-V Characteristics of Copper: Fig. 6.15 shows the I-V characteristics for the Cu-target, recorded for the three different substrate-tubes at 35 Pa up to a maximal power of 30 W. Especially the characteristics for the 12 mm diameter PMMA tube show a transition of the slope n at higher powers. Therefore, linear fits were performed two times and two n values (n_1 and n_2) were obtained for each I-V characteristic.

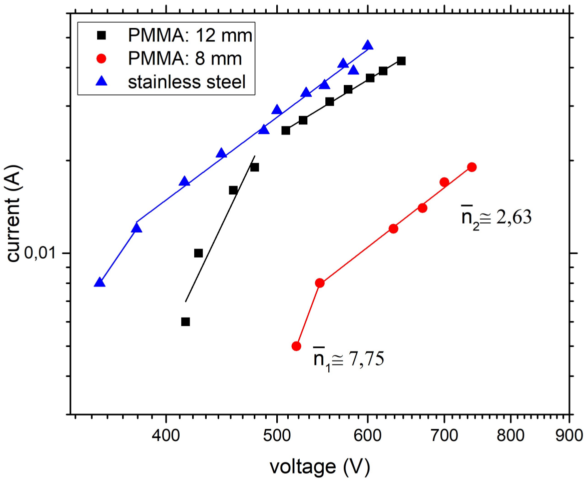

Figure 6.15.: I-V characteristics of Cu for the three different investigated substrate tubes, taken at a pressure of 35 Pa. $\bar{n_1}$ and $\bar{n_2}$ correspond to the mean values of n_1 and n_2 of the characteristics in this graph.

Using this fitting approach, on average the highest values for n were obtained for the 12 mm PMMA tube and the lowest for the 8 mm PMMA tube. I-V characteristics recorded for stainless steel start at lower voltages compared to PMMA and consistently show higher current values. With increasing power, the characteristics for both tubes 12 mm PMMA and 12 mm stainless steel converge.

As can be seen in Fig. 6.16 the characteristics shift to lower voltage with increasing pressure while still exhibiting the same trend (similar n). This is the case for PMMA and for stainless steel.

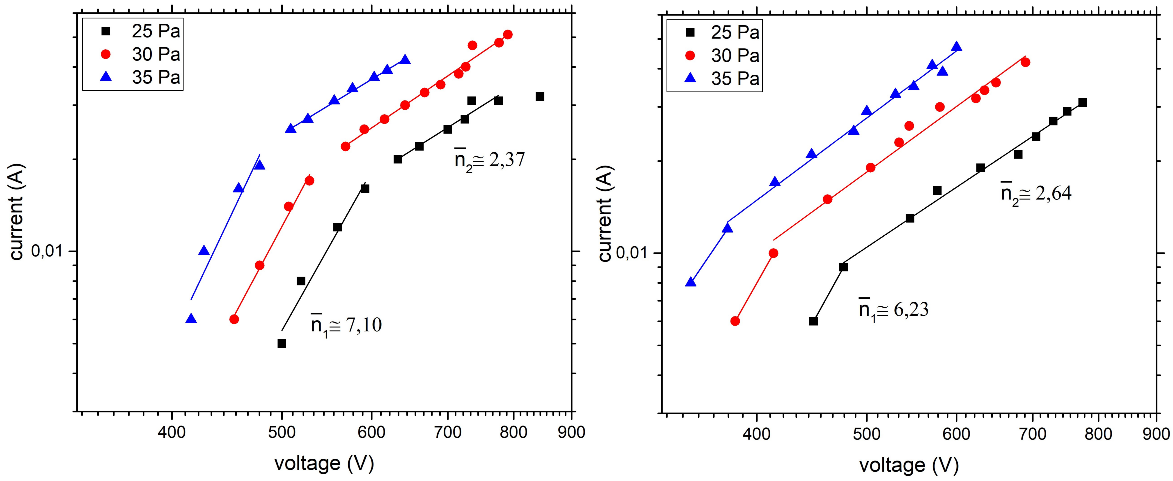

(a) (b)

Figure 6.16.: I-V characteristics of a Cu-target for (a) 12 mm PMMA and (b) stainless steel, recorded at different pressures. $\bar{n_1}$ and $\bar{n_2}$ correspond to the mean values of n_1 and n_2 of the characteristics in these graphs.

I-V Characteristics of Iron: Fig. 6.17 shows the I-V characteristics for the Fe-target, recorded for the three different substrate-tubes at 35 Pa and up to a maximal power of 15 W (the lower maximal power-values come from taking the reduced wire-diameter of 1 mm into account, which supposedly leads to faster target heating).

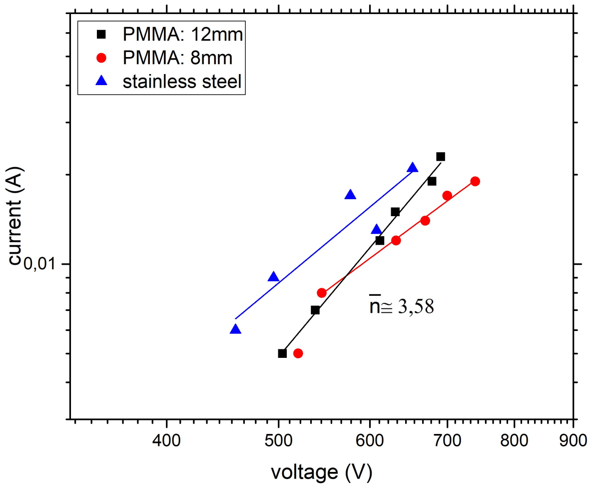

Figure 6.17.: I-V characteristics of Fe using the three different investigated substrate tubes, taken at a pressure of 35 Pa. $\bar{n}$ corresponds to the mean values of n of the characteristics in this graph.

The characteristics are roughly linear, although the measurement-values show variances. n is highest for the 12 mm PMMA-substrate, followed by stainless steel and finally 8 mm PMMA. It is increasing with pressure, also the characteristics shift to higher currents. Again, characteristics recorded for stainless steel start at the lowest voltages.

I-V Characteristics of Aluminum: Fig. 6.18 shows the I-V characteristics for Al recorded for the three different substrate-tubes at a pressure of 35 Pa. All measurements were performed by Sandro Dal Cin in the course of a project work.

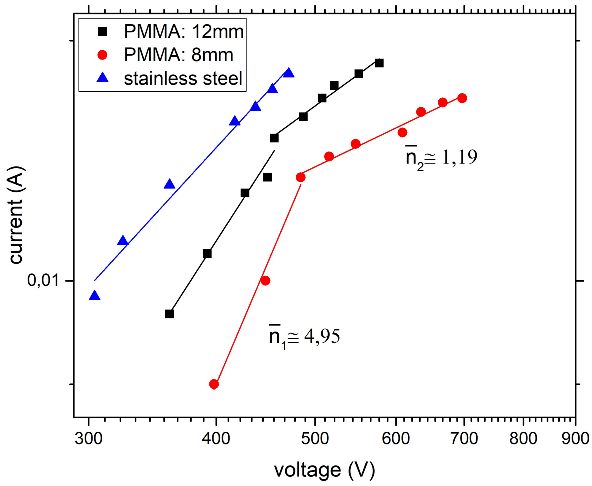

Figure 6.18.: I-V characteristics of Al for the three different investigated substrate tubes, taken at a pressure of 35 Pa. $\bar{n_1}$ and $\bar{n_2}$ correspond to the mean values of n_1 and n_2 of the characteristics in this graph.

These characteristics were recorded up to a maximum power of 25 W. Especially the characteristics for the PMMA tubes exhibit a transition of slope at higher powers. Therefore, again, a linear fit was performed two times for each linear section of the characteristic and two n - values were obtained (n_1 and n_2). Again, n has the highest values for PMMA. Also, the characteristics for stainless steel and the PMMA tube with 12 mm diameter move closer to each other for increasing power as it was also observed for Cu.

Discussion and Conclusion: The strong time-dependent voltage-increase is believed to be caused by increasing target-temperature during the sputter process and can possibly be attributed to temperature induced oxidation effects on the target surface. This is supported by the higher initial pressure of the device in the 10^{-2} Pa range for PMMA tubes and the low 10^{-3} Pa regime for stainless steel tubes.

The log-log-plotted I-V characteristics for Cu and Al showed a transition of the slope n starting at around 15 W. The characteristics for Fe were only recorded up to 15 W because of the higher temperature load on the thinner wire.

This transition may have several reasons: First, temperature effects, even though attempted to minimize, are contributing to cause these transitions, because they get more prominent with increasing power. Second a limited electron trapping efficiency [14] may be given by the electric and magnetic field configuration. From a certain power - value on, the power can only be increased by a disproportionately high voltage increase, because not enough additional electrons can be confined.

Another effect can possibly be attributed to the electron trapping efficiency too: Fig. 6.15 shows that the I-V characteristics for stainless steel and PMMA (12 mm in diameter) are converging with increasing power. For an Ar-pressure of 25 Pa this is already the case at lower power values, see Fig. 6.19, and occurs for all investigated target-materials.

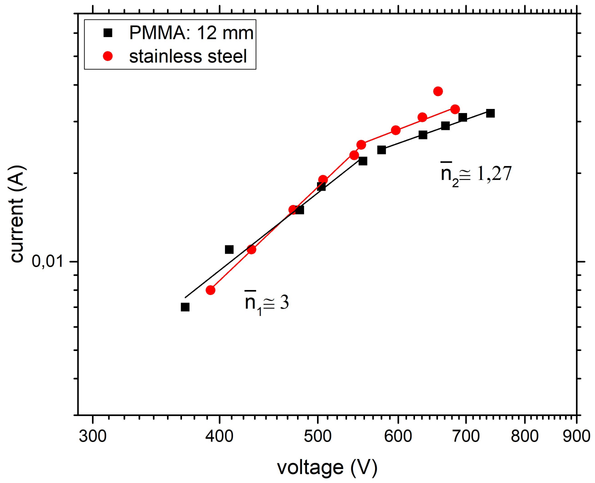

Figure 6.19.: I-V characteristics of Al for the stainless steel and 12 mm PMMA tubes, taken at a pressure of 25 Pa. $\bar{n_1}$ and $\bar{n_2}$ correspond to the mean values of n_1 and n_2 of the characteristics in this graph.

This indicates that the magnetron electron-trapping-efficiency sooner or later outweighs pressure dependencies or influences originating from the tube material. For example, electrons may be lost too quickly to the large stainless steel anode, because of the plasma flux towards the substrate, mentioned in section 5.4. For PMMA substrates, the electron generation is assumed to be less efficient due to the weaker $\vec{E}$ - field and the less favorable distribution of its field lines, see section 6.4.1.

For the Fe- and Al- targets using stainless steel as substrate-tube, the n - values are approximately the same for all pressures (25 Pa, 30 Pa and 35 Pa), and the characteristics display the same trend. For PMMA (12 mm diameter) however, the n - values of the Fe- and Al- targets are similar for 30 Pa and 35 Pa, but not for 25 Pa, see Fig. 6.20. This is in contrast to the Cu-target, see Fig. 6.16a, where the characteristics showed the same trend independent of the used substrate-tube. It indicates, that for a pressure of 25 Pa, the limitation of the magnetron electron trapping efficiency was not yet reached for the configuration of these two target-materials with the PMMA substrate tube.

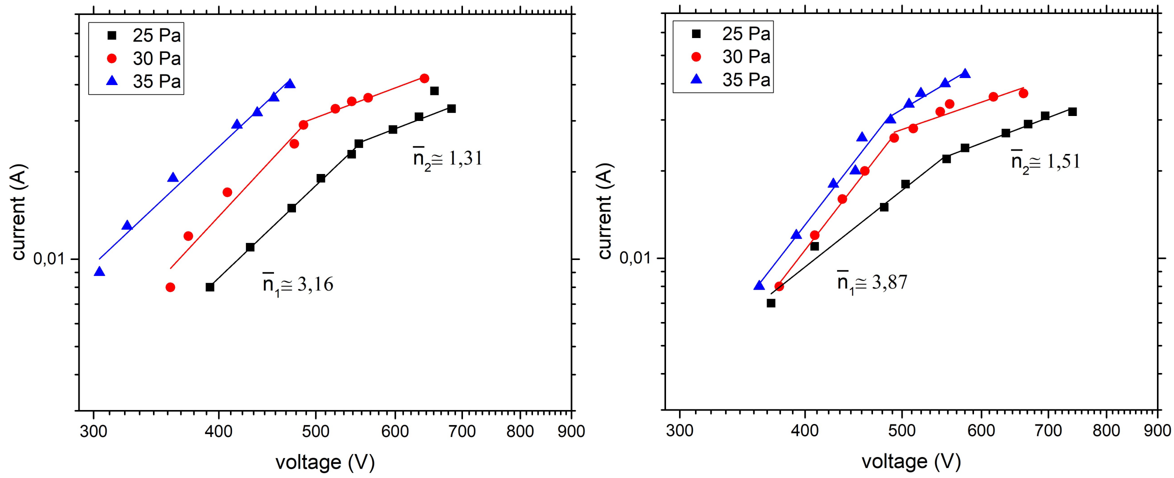

(a) (b)

Figure 6.20.: I-V characteristics of Al for (*a*) stainless steel and (*b*) 12 mm PMMA, recorded at different pressures. $\bar{n_1}$ and $\bar{n_2}$ correspond to the mean values of n_1 and n_2 of the characteristics in these graphs.

In Fig. 6.21 I-V characteristics of all target-materials recorded with the same substrate (PMMA, 12 mm diameter) and pressure (30 Pa) are compared. This plot shows exemplarily that in general Cu exhibits the highest slope in log-log-plots (n). Al in general exhibits the highest current values. Fe ist found to have the highest voltage-values.

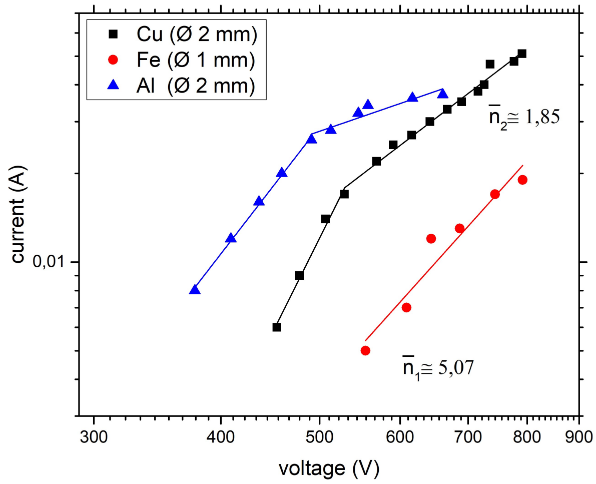

Figure 6.21.: I-V characteristics of the three investigated targets for the 12 mm PMMA substrate-tube, recorded at a pressure of 30 Pa. $\bar{n_1}$ and $\bar{n_2}$ correspond to the mean values of n_1 and n_2 of the characteristics in these graphs.

6.7. Film Characterization and Evaluation

As mentioned before, thin films were deposited on transparency films which were attached to the inner surface of the substrate tubes underneath the magnetron. These were analyzed applying the optical transmission method, described in section 3.4, regarding their film-thickness distribution and deposition rate.

For the 12 mm diameter PMMA tube, films were deposited underneath the area of the unmoved magnetron on the left (closest to the Ar-inlet), middle and right side of the tube. For stainless steel on the left and right side and for PMMA, 8 mm in diameter only in the middle, see below.

Unless stated otherwise, only films deposited on the left side of the tubes are considered (except for PMMA 8 mm in diameter). A list of all deposition experiments is given in the Appendix A.3.

6.7.1. Film Thickness Distribution

A film thickness distribution is shown exemplarily for a Cu-film deposited in a stainless steel tube, see Fig. 6.22. The top corresponds to the left end of the tube, which is closer to the Ar-inlet.

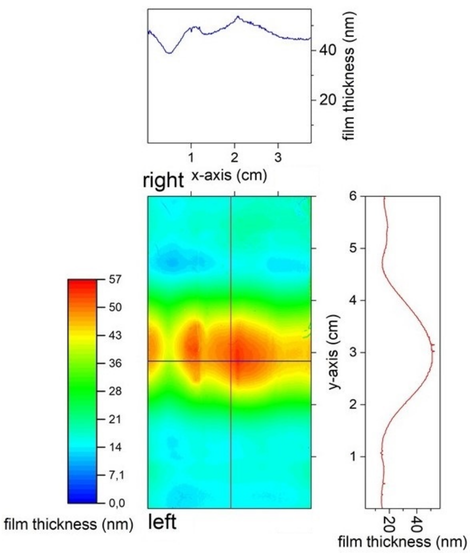

Figure 6.22.: Film thickness distribution of a Cu-film deposited inside a stainless steel tube at a pressure of 30 Pa with 20 W for 18 s.

Likewise, as in section 5.7, the area with maximum deposition is located in the center of the magnetron and extends over a length of around 25 mm. Periodic patterns also start to appear for powers starting from 25 W, for both stainless steel and PMMA 12 mm in diameter, see Fig. 6.23. Again, the top corresponds to the left end of the tube.

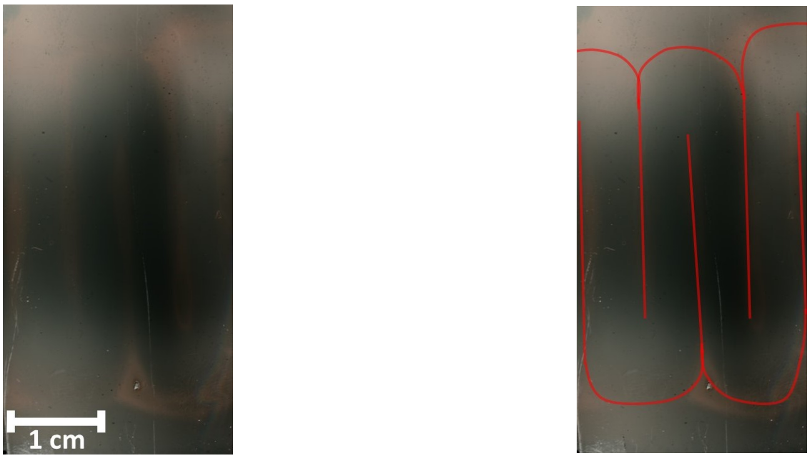

(a) (b)

Figure 6.23.: Cu-film deposited inside a stainless steel tube at 30 Pa with 25 W for 14 s, (*a*) exposing a periodic pattern; (*b*) Pattern is emphasized with red lines.

6.7.2. Deposition Rate

In Fig. 6.24 the deposition-rates for all three substrate tubes are plotted as a function of the applied power. To calculate the deposition rate, only the areas with maximum film-thickness (about 25 mm in length) were taken into account, except for 8 mm PMMA. Because of instabilities the area of maximal deposition varied for this tube.

Also, no deposition rates for the configuration Al/stainless steel could be determined, see section 6.7.3.

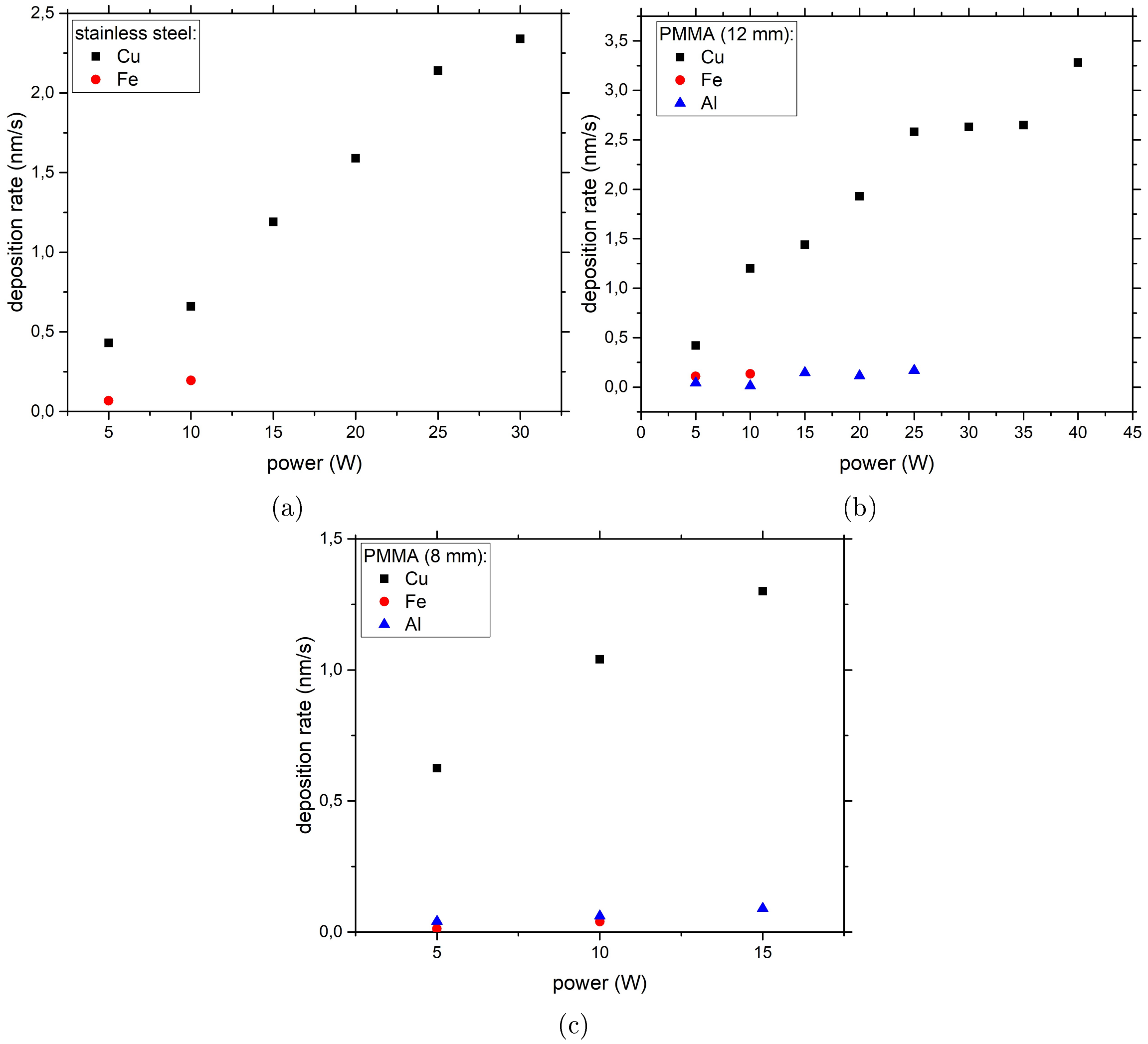

Figure 6.24.: Deposition rates for all investigated target-materials for (*a*) stainless steel, (*b*) 12 mm PMMA and (c) 8 mm PMMA.

The difference in the deposition rates does not fit to the difference in the sputter yields of the materials. For the Fe-target this is believed to be linked to its smaller surface-area which was only half of the surface-areas for the Cu- and Al-targets, because of the difference in wire diameter (2 mm for Cu and Al and 1 mm for Fe). For Al, it is assumed that this difference can be attributed to oxidation effects on the target surface. Oxidation may lead to decreased yield because of the higher surface binding energy of aluminum oxide. It is also possible that an oxide forms on the substrate, which makes the thickness measurement based on optical transmission, in which metallic Al was assumed, unreliable, see also section 6.7.3.

Fig. 6.25 illustrates how, in general, the deposition rate decreases from left (closer to Ar-inlet) to right (closer to pump) over the length of the tubes. It is also visible, that the difference in deposition rate from left to right increases with the applied power. For 35 W and 40 W no film could be deposited anymore on the right side of the PMMA-tube.

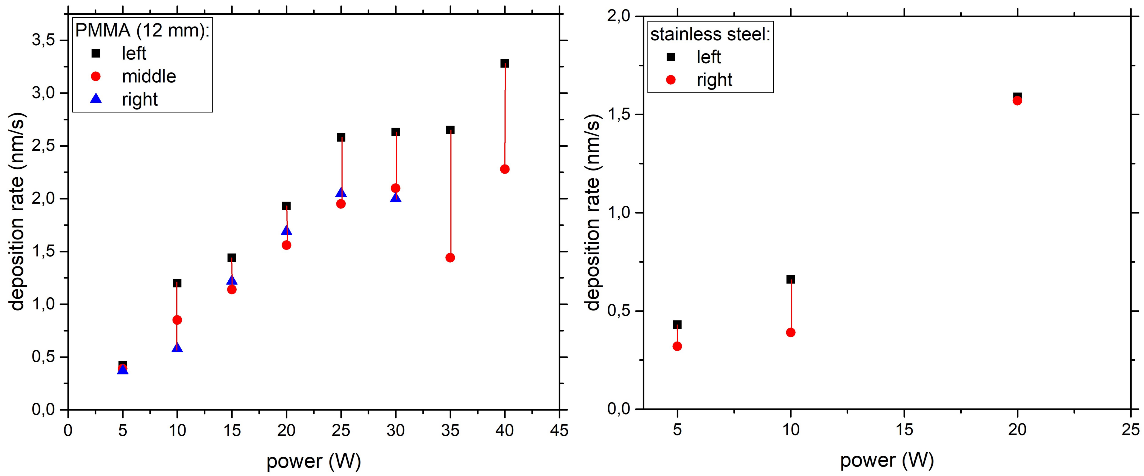

(a) (b)

Figure 6.25.: Deposition rate decrease from left to right over the length of the tube for (*a*) 12 mm PMMA and (*b*) stainless steel.

6.7.3. Substrate-Specific Differences

Stainless steel: As the whole length of the stainless steel tube serves as anode, it is possible that a plasma discharge does not only form under the magnetron. To test this, the stainless steel tube was lined from the inside with aluminum foil, which was chosen because it is conductive. Subsequently a discharge was ignited at 30 Pa and 5 W in the middle of the tube. After a coating time of 1 minute a clearly identifiable film had been deposited only under the area of the magnetron, see Fig. 6.26.

Figure 6.26.: Aluminum foil coated with Cu only in the area of the magnetron in the stainless steel tube, at 30 Pa, 5 W and 60 s.

This was just one exemplary measurement and results could vary for different sets of parameters (e.g. pressure, power).

PMMA, 12 mm in diameter: The area of maximum deposition is not centered under the magnetron anymore as in case of the stainless steel tube, but shifted to the right side towards the anode, see Fig. 6.27.

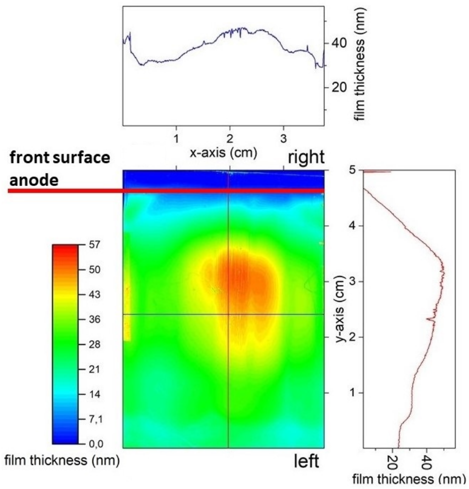

Figure 6.27.: Film thickness distribution of a Cu-film deposited inside a 12 mm PMMA tube at a pressure of 30 Pa with 25 W for 14 s.

This can be understood by considering the electric field distribution, see section 6.4.1, which shows the strongest field close to the anode. Also, a coating free area of about 5 mm is seen. This is due to screening effects of the macor-shield of the anode.

As a result of the high reactivity of Al under atmospheric conditions, the target-wire had to be conditioned. Usually this is done by sputtering against a shutter. Due to constructional constrains, this was not possible here. To determine the deposition rates, the time measurement was started as soon as metallic film growth (as judged visually by the metallic appearance of the deposited film) could be observed in the transparent PMMA tube. Before this, depending on the applied power from a few seconds to a few minutes, no film deposition could be seen despite of stable sputtering conditions. During this time period, it is assumed that a deposition of transparent aluminum oxide took place. Rates were determined as soon as a non-transparent film deposition could be observed, but it could not be determined whether this film also contained aluminum oxide or not.

PMMA, 8 mm in diameter: The anode, see section 6.4, was not constructed for tubes with this diameter, it has a 10 mm front-surface and was situated in the 12 mm PMMA tube on the right side of the narrower 60 mm long PMMA tube. Attention had to be paid for the tube not to be clogged by the anode and therefore inhibiting the Ar-flow. Discharges using this tube were the most unstable, especially for Fe and Al.

6.7.4. Discussion

The highest rates were achieved using the 12 mm PMMA tube. Discharges for this configuration and the stainless steel tube were much more stable and yielded more evenly distributed films than for the 8 mm PMMA tube. Differences in the film thickness distribution for a configuration with the same target but different substrates result from differences in the electric fields, shadowing effects from the anode for the PMMA tubes or the different tube diameter. As mentioned in section 5.7, the area of maximum deposition rate is approximately limited by the distance between the two deflecting magnets on both ends of the magnetron. Also, angle-dependent variations in the deposition thickness are a result of transparency films not perfectly fitting to the inner surface of the tube and therefore different distances to the target-wire.

The dependence of the deposition rate on the location in the tube can be explained by considering the arrangement of the setup: The Ar-inlet is located on the left side of the tube and the pumping system on the right side. Considering the small tube-conductance, see section 6.2, a pressure gradient develops over the length of the tube, which leads to varying plasma conditions along the tube.

Due to the already mentioned heating of the target wire, the wire expanded during the sputter process and had to be retightened several times. The substrate-tubes showed increased temperature too. The effects of long-term deposition were therefore investigated. For this, in both, stainless steel and 12 mm PMMA tubes, Cu and Fe films were deposited over a time period of maximum 20 minutes while continuously moving the magnetron back and forth over the length of the tube. Particular attention was paid to the stability of the system over a long time period. Fig. 6.28 shows the time dependent voltage, which was recorded during a long-term deposition experiment with the configuration Cu/stainless steel for 15 min.

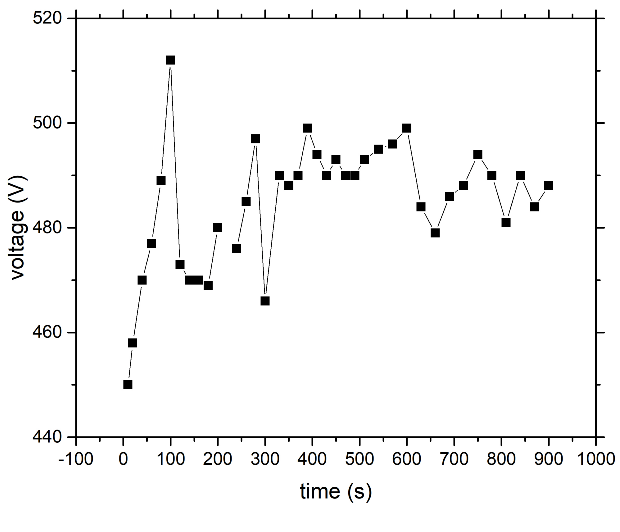

Figure 6.28.: Time dependent voltage for a deposition experiment with a Cu target-wire and a stainless steel substrate-tube, recorded with 10 W, 30 Pa for 15 min.

Because of the pressure-gradient dependent voltage fluctuations from left to right over the length of the substrate-tube, the voltage was only recorded when the magnetron was located at the very left of the substrate-tube. After an initial rise, the voltage fluctuates within a constant voltage range. Bigger voltage drops can be explained by the necessity to retighten the target-wire and thus centering it again inside the substrate tube. From Fig. 6.28 it is assumed that an equilibrium in target temperature was reached after approximately 5 minutes.

A Cu coated 12 mm PMMA tube and a Fe coated 8 mm tube inside a 12 mm tube are shown in Fig. 6.29a.

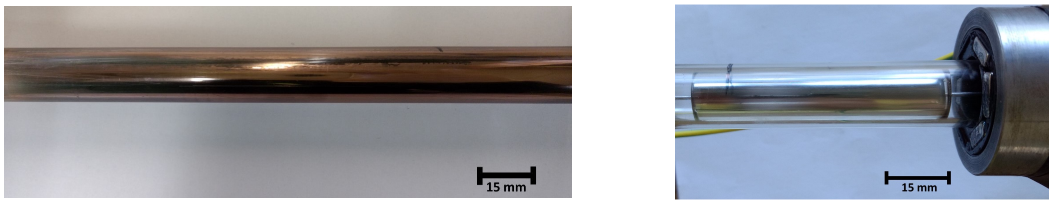

(a) (b)

Figure 6.29.: (*a*) 12 mm PMMA internally coated with Cu and (*b*) 8 mm PMMA inside a 12 mm PMMA internally coated with Fe.

6.8. Temperature Measurements

A temperature measurement was performed on the surface of the stainless steel substrate during a sputter process of the Fe-target with 10 W and 30 Pa. A thermoelement type K was mounted at the margin of the area over which the magnetron continuously moved. The result can be seen in Fig. 6.30.

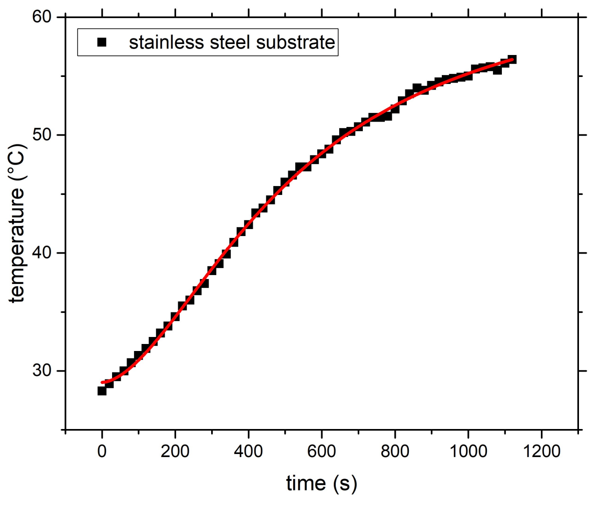

fit parameters	
A_1	29
A_2	63
x_0	520
p	1,73
red. chi-sqr	0,072

Figure 6.30.: Temperature measurement using a thermocouple mounted on the stainless steel substrate during a sputter process.

This curve was fitted with a logistic fit function of the form [29]:

$$y = \frac{A_1 - A_2}{1 + (x/x_0)^p} + A_2 \tag{6.6}$$

whereas the following meanings can be assigned:

- A_1 ... initial temperature
- A_2 ... final temperature
- x_0 ... center
- p ... order of the curve

A logistic function describes a curve with limited growth, as it is the case for processes where an equilibrium can be reached. As suggested by the fit the final temperatures are reached after roughly 4 min.

Temperature measurements were also performed on the Cu target-wire, with a static magnetron in two different ways: by using temperature indicating labels or with a Pt100 element. Both were mounted on the Cu target-wire at the margin of the sputtered area. The Pt100 element was about 10 mm away from the sputtered area and the temperature indicating labels about 2,5 mm, see section 3.6.

Fig. 6.31 compares these two measuring methods.

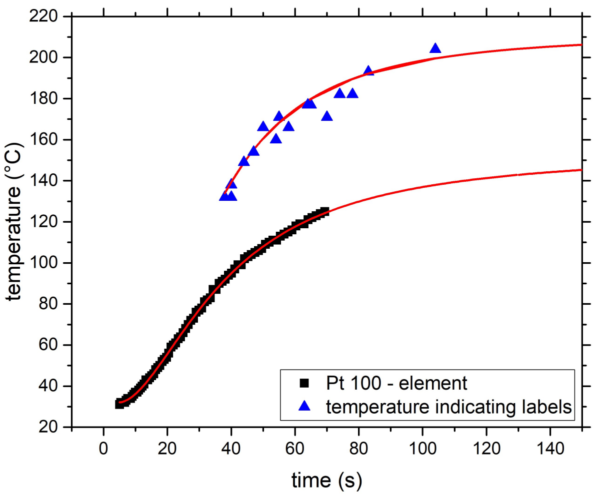

fit parameters		
	labels	Pt 100
A_1	26	32
A_2	212	154
x_0	33	33
p	2,44	1,75
red. chi-sqr.	10,849	0,378

Figure 6.31.: Comparison of the temperature measurements on the Cu target-wire using temperature indicating labels and a Pt100 element.

Again the graphs were fitted with Eq. 6.6. The two techniques yielded different results. This could be due to the following factors:

Thermal Contact of the Pt100-Element: The main thermal contact of the Pt100-element is assumed to be through the Cu-wire with which it is mounted on the target-wire and not with the target itself (see Fig. 3.4 in section 3.6). This is due to the geometric incompatibility between the Pt100-element, which is flat, and the round target wire.

Influence of the Plasma: It is assumed, that the temperature indicating labels were influenced by heat transfer from the plasma. This temperature transfer from the plasma is not necessarily equivalent to the total heat transfer to the target-wire within the magnetron. Plasma leaking from the magnetron to the temperature sensitive labels may also cause an additional heat flux to the label. Because the Pt100 was mounted further away and insulated with Teflon, which also contributes in some degree to thermal insulation, this effect is believed to not be so prominent for the Pt100 element.

One can conclude the following: Fig. 6.31 shows that both curves reach saturation after approximately the same time interval. This indicates that no time delay in the heating of the Pt100 element is present. It is assumed that the strong difference in temperature using the two measurement techniques is a result of the following factors: the influence of the plasma on the temperature indicating labels, the thermal insulation resulting from the mounting of the Pt100-element and also strong temperature gradients from the area under the static magnetron, which was sputtered, to the measured areas. In one experiment it had been observed that the Fe target-wire started to glow under the static magnetron, whereas outside the magnetron no visible thermal glowing was observed.

6.9. Discussion and Outlook

The biggest advantage of the present setup is the easy accessibility of the magnetron assembly from the ambient. Also, the plasma first starts to develop underneath the magnetron, depending on the set Ar-pressure and power. Therefore, it is possible to introduce controlled film-thickness gradients by coating the tube only at desired areas. This area-specific deposition also counteracts possible overheating of the target by continuously moving the zone of maximum thermal load.

Due to the fact that the substrate is part of the vacuum chamber, the substrate length is flexible, because it is not limited by an external vacuum chamber. This is also a cost-effective solution. However, a pressure gradient forms, which increases with increasing tube length, see section 6.2.

The produced thin films on the inner surface of insulating and conducting substrate-tubes show different film-thickness distributions depending on the different electric field line distributions. Also, due to the pressure gradient over the length of the device, the deposition rate decreases from left (closer to Ar-inlet) to right (closer to pumping system). It is believed, that even films can be produced with an automated control of the magnetron motion pattern in a way that balances these factors. Also, a second Ar-inlet on the right side of the substrate-tube and/or a symmetric positioning of pumping outlets would counteract the pressure gradient during the deposition process.

Heat effects were observed in the I-V characteristics due to the warming of the target starting at higher powers for a stationary magnetron. Fig. 6.28 showing voltage data for the long-time deposition experiment with a moving magnetron indicates that a temperature equilibrium was reached.

The base pressure for PMMA of 10^{-2} Pa was in the upper high-vacuum range, for stainless steel it was in the 10^{-3} Pa region. Therefore, it is assumed, that the base pressure for PMMA is already close to the vapor pressure of PMMA. The deposition process took place at pressures three or four orders of magnitude higher, in the 10 Pa range. Nevertheless, oxidation effects on the target with the residual oxygen are assumed to take place due to strong target warming during the deposition process. By increasing the conductance of the tubes, the base pressure at least for stainless steel can be decreased. In addition, the effective pumping speed can be improved by 51% simply by directly connecting the device to the pumping system and therefore avoiding the 750 mm long flexible corrugated hose. The length of the device can also be shortened using vacuum parts with the same diameter and therefore avoiding reducers, this would shorten the length for about 135 mm and improve the effective pumping speed by about 7%.

7. Cumulative Summary and Conclusion

Starting from an existing magnetic configuration, two magnetrons, a modular cylindrical magnetron and a toroidal magnetron for the internal coating of narrow tubes were designed and constructed in this thesis. Their magnetic field configuration was measured using a Hall probe as well as simulated using the program *FEMM* [19]. Due to the same magnetic configuration, both magnetrons show curved $\vec{B}$ - field lines between two neighboring magnets. While the magnetic field strength is 30% of its initial value at the surface of a magnet at the target surface for the modular magnetron, it is only 3,9% for the toroidal magnetron. I-V characteristics were recorded to test the performance of the two systems.

- For the cylindrical modular magnetron the following can be stated: A distinct behavior difference was found between the configuration with 2 segments and the configurations with 3 to 5 segments. While the system with 2 segments showed only a slight dependence of its global characteristics on the working gas pressure and even an increase of its electron trapping efficiency with the degree of twist between the segments, the opposite behavior was observed for the other configurations. In general, the modular magnet arrangement can be easily implemented into cylindrical targets of arbitrary length and twisting the segments relative to each other even allows to realize different plasma conditions and configurations in different selected portions of the target.

- The toroidal magnetron was part of the construction of a device for the internal coating of narrow tubes. For this device, conducting (stainless steel) and insulating (PMMA) substrate-tubes with an inner diameter of 12 mm, and 8 mm (in some cases) were tested. These tubes simultaneously served as a substrate and as a part of the vacuum-chamber. For the insulating tubes a special anode was constructed, while conducting tubes themselves served as anode. This yielded differences in the formed electric field line distribution. The deposited thin films were only slightly affected by this difference and showed, in general, an area of enhanced deposition of around 25 mm in width. This can be attributed to the geometry of the magnetic configuration of the magnetron.

  The deposition rates were the highest at the side close to the Ar-inlet and decreased over the length of the tube. This can be explained by a pressure gradient, which developed due to the low conductance of the vacuum components and the substrate-tube itself. Typical deposition rates for the different target materials were in the range 0,3 nm/s - 3,3 mn/s for Cu, 0,01 nm/s - 0,19 nm/s for Fe and 0,04 nm/s - 0,17 nm/s for Al, depending on the applied power which ranged from 5 W to 40 W maximum for Cu.

A time dependent voltage increase was apparent, especially for higher applied powers. This was attributed to heating effects of the target. The I-V characteristics show a transition of slope starting from 15 W. Also, the characteristics for the 12 mm diameter tubes are converging with increasing power, which indicates a higher dependence of I-V characteristics on the electron-trapping efficiency of the magnetron than on other system parameters at these powers.

Nonetheless it was possible to achieve stable deposition conditions for several tens of minutes by moving the magnetron, which is fully accessible from the ambient. This distributes the mean temperature load on the target and allows the deposition of continuous films all along tubes of a tested length up to 30 cm. The controlled target movement has counteracting effects on pressure gradients or uneven heat loads and is considered to be a key parameter to optimize coating-uniformity.

8. Acknowledgments

I wish to thank most of all my supervisor, Prof. Christoph Eisenmenger-Sittner, for giving me the opportunity to work in this group. He was always available with continuous guidance, professional advice and good ideas.

I would also like to thank the other group-members for the delightful working atmosphere and for the help when I needed assistance.

Gratitude is owned to the workshop of the institute of Solid State Physics under the responsibility of Andreas Lahner, which played a big part in the realization of the constructed device.

Finally, very special gratitude is owned to my family, who were always there to support me and lifted a lot of weight from my shoulders in difficult situations. By doing this, they significantly contributed to me successfully concluding my studies.

Bibliography

[1] Demtröder, Wolfgang: *Experimentalphysik 1 Mechanik und Wärme.* Springer, 2008

[2] Jousten, K.: *Wutz Handbuch Vakuumtechnik.* Springer Verlag, 2012

[3] MKS: *How an MKS Baratron Capacitance Manometer Works.* https://www.mksinst.com/docs/ur/barainfo2b.aspx, [03.06.2018]

[4] Haefer, R.: *Oberflaechen- und Duennschicht-Technologie ; Teil I: Beschichtungen von Oberflaechen".* Springer Verlag, 1987

[5] Martin, Peter M.: *Handbook of deposition technologies for films and coatings : science, applications and technology.* Amsterdam [u.a.] : Elsevier, 2009

[6] Frey, H.: *Handbook of thin film technology.* Berlin [u.a.] : Springer-Verlag, 2015

[7] Group, IAP/TU Wien Surface P.: *A Simple Sputter Yield Calculator.* URL: https://www.iap.tuwien.ac.at/www/surface/sputteryield, [12.03.2018]

[8] Yamamura, Y. and Tawara, H.: Energy Dependence of Ion-Induced Sputtering Yields from Monoatomics Solids at Normal Incidence. In: *Atomic Data and Nuclear Data Tables* Vol. 62 (1996), März, Nr. No. 2, S. 149 – 253

[9] Laimer, J.: *Plasmatechnologie und -Chemie.* Vienna : Technische Universitaet Wien, 2015

[10] Keidar, Michael and Beilis, Isak: *Plasma Engineering Applications from Aerospace to Bio- and Nanotechnology.* Elsevier Science, 2013

[11] Demtröder, Wolfgang: *Experimentalphysik 2 Elektrizität und Optik.* Springer Spektrum, 2008

[12] Lieberman, Michael A. and Lichtenberg, Allan J.: *Principles of Plasma Discharges and Materials Processing.* Wiley-Interscience, 2005

[13] Bittencourt, J. A.: *Fundamentals of Plasma Physics.* Springer, 2004

[14] Thornton, John A.: Magnetron sputtering: basic physics and application to cylindrical magnetrons. In: *Journal of Vacuum Science and Technology* 15 (1978)

[15] KELLY, P. and ARNELL, R.: Magnetron sputtering: a review of recent developments and applications. In: *Vacuum* 56 (2000), S. 159–172

[16] WESTWOOD, W. D.; MANIV, S. and SCANLON, P. J.: The current-voltage characteristic of magnetron sputtering systems. In: *Journal of Applied Physics* 54 (1983), Nr. 12

[17] AREPOC: *Arepoc Hall probes.* http://www.arepoc.sk/?p=25, [21.06.2018]

[18] KG, ChenYang Technologies GmbH & C.: *NdFeB Magnets.* http://www.chenyang.de/hauptseite.htm, [05.09.2018]

[19] MEEKER, David: *Finite Element Method Magnetics.* http://www.femm.info/wiki/HomePage, [09.06.2018]

[20] STEINKE, Peter: *Finite-Elemente-Methode Rechnergestützte Einführung.* Springer, 2007

[21] MAHR, Harald: *Numerische Berechnungen zur Beschichtung granularer Materialien in einer Magnetron-Sputteranlage.* Bd. Masters Thesis. Vienna University of Technology, 2009

[22] HORST BIERMANN, Lutz K.: *Moderne Methoden der Werkstoffprüfung.* Wiley, 2015

[23] GIBSON, I. P.: Erosion-resistant coating of tubes by physical vapour deposition. In: *Thin Solid Films* 83 (1981)

[24] HAGEDORN, D.; LÖFFLER, F. and MEESS, R.: Magnetron sputter process for inner cylinder coatings. In: *Surface & Coatings Technology* 203 (2008)

[25] FUJIYAMA, Hiroshi: Inner coating of long-narrow tube by plasma sputtering. In: *Surface and Coatings Technology* 131 (2000)

[26] KAWASAKI, Hiroharu; SHIBAHARA, Katsuki; OHSHIMA, Tamiko; YAGYU, Yoshihito and SUDA, Yoshiaki: Effects of Surface Coating on Cylinder Rods Prepared Using Sputtering Deposition Method with Modulated Magnetic Field. In: *Japanese Journal of Applied Physics* (2010)

[27] TRANSPARENT-DESIGN: *Acrylic Glass.* https://www.transparentdesign.at/, [10.08.2018]

[28] CORNING: *Macor - Machinable Glass Ceramic For Industrial Applications.* https://docs-emea.rs-online.com/webdocs/0397/0900766b80397c65.pdf, [21.11.2018]

[29] ORIGINLAB: *Logistic Fit Function.* https://www.originlab.com/doc/Origin-Help/Logistic-FitFunc, [07.10.2018]

List of Figures

List of Tables

A. Appendix

A.1. Modular Cylindrical Magnetron: I-V characteristics-results

Table A.1.: The obtained values for n and V_0 (when assuming a minimal current of 0,1 A) are given. n is the slope of log-log current-voltage plots. For I-V characteristics which showed a transition in slope, linear fits were performed two times and two values for n (n_1 and n_2) are given.

		5 Segments		4 Segments		3 Segments		2 Segments	
press.	twist	n_1/n_2	V_0 (V)	n_1/n_2	V_0 (V)	n_1/n_2	V_0 (V)	n_1/n_2	V_0 (V)
0,4 Pa	0°	3,81 ± 0,16	201,00	4,25 ± 0,21	217,19	4,36 ± 0,16	242,97	4,78 ± 0,04	288,56
	10°	3,23 ± 0,08	173,11	3,51 ± 0,17	201,85	3,59 ± 0,24	227,27	4,11 ± 0,06	278,17
	20°	5,95 ± 0,25 / 0,83 ± 0,23	281,02	1,7 ± 0,05 / 0,05 ± 0,26	122,82	0,91 ± 0,28	58,78	3,74 ± 0,07	288,33
	30°	0,88 ± 0,19	282	1,42	286,91	0,64	83,53	4,32 ± 0,07	323,04
0,7 Pa	0°	3,90 ± 0,09	193,72	4,46 ± 0,07	220,31	4,66 ± 0,03	243,36	4,98 ± 0,08	278,68
	10°	3,70 ± 0,13	188	3,85 ± 0,09	202,53	3,62 ± 0,09	214,32	4,86 ± 0,07	278,25
	20°	3,39 ± 0,28 / 1,07 ± 0,07	195,90	2,53 ± 0,14 / 0,56 ± 0,05	163,47	2,81 ± 0,24 / 0,47 ± 0,05	200,67	4,97 ± 0,13	301,21
	30°	1,32 ± 0,12 / 0,73 ± 0,29	225,79	0,77 ± 0,03	47,35	1,02 ± 0,21	85,38	5,75 ± 0,10	320,69
1 Pa	0°	4,57 ± 0,10	313,47	4,87 ± 0,09	228,90	5,12 ± 0,08	251,41	5,88 ± 0,03	294,32
	10°	4,42 ± 0,1	212,84	4,34 ± 0,16	214,68	4,48 ± 0,09	234,71	5,23 ± 0,09	278,93
	20°	4,04 ± 0,19 / 1,04 ± 0,06	215,85	3,65 ± 0,11 / 0,62 ± 0,21	207,87	4,32 ± 0,14 / 1,15 ± 0,18	250,11	6,05 ± 0,13	309,67
	30°	2,26 ± 0,10 / 0,53 ± 0,07	245,12	1,50 ± 0,1 / -0,04 ± 0,23	120,22	2,31 ± 0,32 / 0,65 ± 0,07	185,52	6,56 ± 0,14	316,22
1,5 Pa	0°	5,21 ± 0,07	226,50	5,68 ± 0,07	243,96	5,94 ± 0,04	257,16	6,32 ± 0,06	279,84
	10°	5,18 ± 0,07	227,58	5,25 ± 0,09	235,19	5,3 ± 0,06	249,01	6,19 ± 0,04	289,75
	20°	4,04 ± 0,19 / 1,16 ± 0,15	215,85	4,05 ± 0,15 / 1,07 ± 0,19	210,59	4,79 ± 0,17	255,72	6,76 ± 0,15	301,50
	30°	3,83 ± 0,27 / 0,92 ± 0,06	258,54	2,42 ± 0,29 / 0,84 ± 0,05	170,37	3,88 ± 0,22 / 0,89 ± 0,07	240,68	7,29 ± 0,16	306,87
2 Pa	0°	5,74 ± 0,07	235,78	6,00 ± 0,1	246,41	6,42 ± 0,04	265,26	6,59 ± 0,05	289,27
	10°	5,34 ± 0,04	225,9	5,82 ± 0,08	242,59	5,97 ± 0,09	256,27	6,69 ± 0,03	276,75
	20°	4,64 ± 0,34 / 1,16 ± 0,15	219,03	5,15 ± 0,07 / 2,55 ± 0,24	233,80	5,83 ± 0,14	259,04	7,14 ± 0,09	296,47
	30°	3,94 ± 0,20 / 0,56 ± 0,04	238,87	2,63 ± 0,23 / 0,82 ± 0,04	166,16	4,62 ± 0,43 / 0,85 ± 0,14	250,18	8,25 ± 0,14	310,21

A.2. Magnetron for Internal Coatings and designed device: I-V characteristics-results for n and V0

Table A.2.: The obtained values for n and V_0 (when assuming a minimal current of 0,011 A) for the Cu target are given. I-V characteristics showed a transition in slope, in this case two values for n are given for a characteristics.

	Cu target-wire					
	PMMA: 12 mm		PMMA: 8 mm		stainless steel	
press.	n_1/n_2	V_0 (V)	n_1/n_2	V_0 (V)	n_1/n_2	V_0 (V)
25 Pa	6,58 ± 0,86 / 2,34 ± 0,29	385,94			6,7 / 2,47 ± 0,08	244,37
30 Pa	6,92 ± 0,48 / 2,53 ± 0,11	349,22			6,56 / 2,70 ± 0,14	291,70
32 Pa			1,68	182,76		
35 Pa	7,81 ± 1,57 / 2,25 ± 0,25	324,39	10 / 2,88 ± 0,09	173,37	5,45 / 2,76 ± 0,09	239,78
40 Pa			5,83 / 2,24 ± 0,15	161,33		

Table A.3.: The obtained values for n and V_0 (when assuming a minimal current of 0,011 A) for the Fe target are given.

	Fe target-wire					
	PMMA: 12 mm		PMMA: 8 mm		stainless steel	
press.	n	V_0 (V)	n	V_0 (V)	n	V_0 (V)
25 Pa	2,15 ± 0,24	261,43			2,17 ± 0,66	265,48
30 Pa	3,84 ± 0,49	357,83			2,61 ± 0,79	271,87
32 Pa			1,18	142,08		
35 Pa	4,64 ± 0,17	355,87	2,88 ± 0,12	265,89	3,23 ± 0,65	256,90
40 Pa			2,91 ± 0,24	237,41		

Table A.4.: The obtained values for n and V_0 (when assuming a minimal current of 0,011 A) for the Al target are given. I-V characteristics showed a transition in slope, in this case two values for n are given for a characteristics.

	Al target-wire					
	PMMA: 12 mm		PMMA: 8 mm		stainless steel	
press.	n_1/n_2	V_0 (V)	n_1/n_2	V_0 (V)	n_1/n_2	V_0 (V)
25 Pa	2,72 ± 0,24 / 1,32 ± 0,08	177,82			3,28 ± 0,05 / 1,29 ± 0,10	175,93
30 Pa	4,46 ± 0,12 / 1,18 ± 0,21	236,83	3,54 ± 0,05 / 0,89 ± 0,33	237,52	2,98 ± 0,19 / 1,33 ± 0,12	161,45
35 Pa	4,44 ± 0,30 / 2,03 ± 0,22	225,73	7 ± 0,75 / 1,42 ± 0,10	318,31	3,24 ± 0,17	149,94
40 Pa			9,23 ± 2,41 / 1,18 ± 0,08	337,83		

A.3. List of all Deposition Experiments

Table A.5.: All performed deposition experiments for every target/substrate configuration are given. The deposition rate was determined by taking into account only the area with maximal deposition (25 mm).

target/substrate	position	pressure (Pa)	power (W)	time (s)	dep. film thickness (nm)	dep. rates (nm/s)
Cu/PMMA: 12 mm	left	30	5	81	34,69	0,42
Cu/PMMA: 12 mm	left	30	10	51	61,44	1,2
Cu/PMMA: 12 mm	left	30	15	31	44,84	1,44
Cu/PMMA: 12 mm	left	30	20	18	34,75	1,93
Cu/PMMA: 12 mm	left	30	25	14	36,25	2,58
Cu/PMMA: 12 mm	left	30	30	19	50,09	2,63
Cu/PMMA: 12 mm	left	30	35	17	45,19	2,65
Cu/PMMA: 12 mm	left	30	40	10	32,82	3,28
Cu/PMMA: 12 mm	middle	30	5	81	32,1	0,39
Cu/PMMA: 12 mm	middle	30	10	51	41,1	0,85
Cu/PMMA: 12 mm	middle	30	15	31	35,6	1,14
Cu/PMMA: 12 mm	middle	30	20	18	28,1	1,56
Cu/PMMA: 12 mm	middle	30	25	14	27,4	1,95
Cu/PMMA: 12 mm	middle	30	30	19	40	2,1
Cu/PMMA: 12 mm	middle	30	35	17	24,6	1,44
Cu/PMMA: 12 mm	middle	30	40	10	22,8	2,28
Cu/PMMA: 12 mm	right	30	5	81	30	0,37
Cu/PMMA: 12 mm	right	30	10	51	29,99	0,58
Cu/PMMA: 12 mm	right	30	15	31	38	1,22
Cu/PMMA: 12 mm	right	30	20	18	30,58	1,69
Cu/PMMA: 12 mm	right	30	25	14	28,8	2,05
Cu/PMMA: 12 mm	right	30	30	19	38	2
Cu/PMMA: 8 mm	middle	35	5	40	25	0,62
Cu/PMMA: 8 mm	middle	35	10	30	31,2	1,04
Cu/PMMA: 8 mm	middle	35	15	15	19,5	1,3
Cu/stainless steel	left	30	5	81	34,69	0,42
Cu/stainless steel	left	30	10	51	33,63	0,66
Cu/stainless steel	left	30	15	31	36,89	1,19
Cu/stainless steel	left	30	20	18	28,68	1,59
Cu/stainless steel	left	30	25	14	29,97	2,14
Cu/stainless steel	left	30	30	19	44,44	2,34
Cu/stainless steel	right	30	5	81	26	0,32
Cu/stainless steel	right	30	10	51	20,3	0,39
Cu/stainless steel	right	30	20	18	28,3	1,57
Fe/PMMA: 12 mm	left	30	5	300	32,63	0,11
Fe/PMMA: 12 mm	left	30	10	120	16,23	0,13
Fe/PMMA: 12 mm	middle	30	5	600	7,6	0,0,0126
Fe/PMMA: 12 mm	middle	30	10	180	8,8	0,04
Fe/PMMA: 12 mm	right	30	5	180	2,1	0,01
Fe/PMMA: 12 mm	right	30	10	70	10,4	0,14

Table A.6.: All performed deposition experiments for every target/substrate configuration are given. The deposition rate was determined by taking into account only the area with maximal deposition (25 mm). Experiments containing the Al-target were performed by Sandro Dal Cin in the course of a project work.

target/substrate	position	pressure (Pa)	power (W)	time (s)	dep. film thickness (nm)	dep. rates (nm/s)
Fe/PMMA: 8 mm	middle	35	10	180	8,7	0,05
Fe/stainless steel	left	30	5	180	12,17	0,07
Fe/stainless steel	left	30	10	70	13,67	0,19
Fe/stainless steel	right	30	5	300	6,8	0,02
Fe/stainless steel	right	30	10	70	9,8	0,14
Al/PMMA: 12 mm	left	30	5	210	2,65	0,013
Al/PMMA: 12 mm	left	30	10	90	3,91	0,043
Al/PMMA: 12 mm	left	30	15	60	8,83	0,147
Al/PMMA: 12 mm	left	30	20	30	3,43	0,114
Al/PMMA: 12 mm	left	30	25	20	3,48	0,17
Al/PMMA: 12 mm	right	30	5	210	2,3	0,01
Al/PMMA: 12 mm	right	30	10	90	3,9	0,04
Al/PMMA: 12 mm	right	30	15	60	4	0,07
Al/PMMA: 12 mm	right	30	20	30	2,8	0,09
Al/PMMA: 12 mm	right	30	25	20	3,8	0,19
Al/PMMA: 8 mm	middle	35	5	210	8,7	0,04
Al/PMMA: 8 mm	middle	35	10	90	3,7	0,06
Al/PMMA: 8 mm	middle	35	15	60	5,5	0,09

A.4. Device for Internal Coatings of Narrow Tubes: Parts list

A.4.1. Pfeiffer Vacuum Standard Components

- 4 × Clamping Ring for Elastomer Seal DN 32 / 40 ISO-KF: ord. no.: 120BSR040
- 4 × Centering ring Aluminum DN 40 ISO-KF: ord. no.: 112ZRG040
- 9 × Clamping Ring for Elastomer Seal DN 20 / 25 ISO-KF: ord. no.: 120BSR025
- 4 × Centering ring Aluminum DN 25 ISO-KF: ord. no.: 112ZRG025
- 3 × Clamping Ring for Elastomer Seal DN 10 / 16 ISO-KF: ord. no.: 110BSR016
- 4 × Centering ring Aluminum DN 16 ISO-KF: ord. no.: 112ZRG016
- Reducer Cross, Stainless Steel DN 25-16 ISO-KF: ord. no.: 120RKR025-016
- 2 × Tee, Stainless Steel DN 25 ISO-KF: ord. no.: 120RTS025
- 4 × Straight Reducer, Stainless Steel DN 40-25 ISO-KF: ord. no.: 120RRG040-025-40
- 2 × Tube Compression Fitting, Stainless Steel DN 25 ISO-KF for 16 mm Tube Diameter: ord. no.: 120XQV025-16
- Corrugated Hose, Flexible, Stainless Steel DN 25 ISO-KF 750 mm length: ord. no.: 120SWN025-0750

A.4.2. Valves

- HV angle valve Series 264 DN 25: VAT, ord. no.: 26428-KE01-0001

A.4.3. Instruments

- DC Generator MDX 500 Magnetron Drive: Advanced Energy Industries, ord. no.: 5700502-D
- Penning/Pirani gauge: Adixen ACC 2009
- Penning/Pirani Controller: Adixen ACS 2000
- Penning gauge: Alcatel CF2P
- Penning Controller: Alcatel FA 101
- Turbomolecular Pump: Alcatel 5080
- Turbomolecular Pump Controller: Alcatel cff 100

A.4.4. Other Components

- air inlet
- needle valve: Alcatel Type 6819
- Ar bottle
- bellow DN 40
- rail 1 m
- slide
- 2 × mount: designed during thesis
- construction to contract or expand the below: designed during thesis
- clamping system: designed during thesis
- toroidal magnetron: designed during thesis
- substrate tubes: Niro 1.4301 tube DN EN 1127 AD: 12 mm, ID: 8 mm: Fixmetall, art. nr.: DEKO01162.0; 128XT Acrylglas-Rohr XT, AD: 16 mm, ID: 12 mm, and AD: 12 mm, ID: 8 mm: Transparent Design
- Anode: designed during thesis